FERMILAB-THESIS-1999-55

POLARIZATION OF Λ^0 INCLUSIVELY PRODUCED BY A 610 GeV/c Σ^- BEAM

by

Kenneth Day Nelson

An Abstract

Of a thesis submitted in partial fulfillment
of the requirements for the Doctor of
Philosophy degree in Physics
in the Graduate College of
The University of Iowa

May 1999

Thesis supervisors: Professor Ed McCliment
Professor Yasar Onel

I have measured the polarization of Λ^0 inclusively produced by a 610 GeV/c Σ^- beam incident on copper and carbon targets in experiment E781 (SELEX) at Fermilab. The method used was a bias canceling technique. The polarization was measured in the range x_f (0.3 - 1.0), and Λ^0 transverse momentum (0.1 - 2.5 GeV/c). The Λ^0's produced have a similar magnitude but opposite sign of polarization to those produced using a proton beam. This is the first measurement of Λ^0 polarization from a Σ^- beam at this energy and the second measurement at any energy. This greatly extends the range in x_f of Σ^- produced Λ^0 polarization.

Abstract approved: ____
Thesis supervisor

____
Title and department

____
Date

____
Thesis supervisor

____
Title and department

____
Date

POLARIZATION OF Λ^0 INCLUSIVELY PRODUCED BY A 610 GeV/c Σ^- BEAM

by

Kenneth Day Nelson

A thesis submitted in partial fulfullment
of the requirements for the Doctor of
Philosophy degree in Physics
in the Graduate College of
The University of Iowa

May 1999

Thesis supervisors: Professor Ed McCliment
Professor Yasar Onel

Graduate College
The University of Iowa
Iowa City, Iowa

CERTIFICATE OF APPROVAL

____

PH.D. THESIS

____

This is to certify the the Ph.D. thesis of

Kenneth Day Nelson

has been approved by the Examining Committee for the thesis requirement for the Doctor of Philosophy degree in Physics at the May 1999 graduation

Thesis committee: ____
Thesis supervisor

____
Thesis supervisor

____
Member

____
Member

____
Member

[redacted]

If a man eats a pound of pasta and a pound of antipasto... would they cancel each other out, leaving the man still hungry?

-Scott Adams, *“Dilbert”*

ACKNOWLEDGMENTS

I owe thanks to many people who have contributed to the work described in this thesis. I thank my advisors Ed McCliment and Yasar Onel for their guidance and support during the analysis. Peter Cooper for his support and guidance throughout my graduate career. Joe Lach for his help and advise throughout this analysis. My officemate, Suat Özkorucuklu, with whom I had many talks, and who was a constant source on encouragement. Charles Newsom for his help in the beginning of my graduate journey. The E781 collaborators who helped to make this experiment the success that it is. My friends and colleagues at the University of Iowa who made my graduate experience a pleasant one. Finally, my family, for supporting me in every way possible.

TABLE OF CONTENTS

Page

APPENDIX

LIST OF FIGURES

LIST OF TABLES

CHAPTER 1.

INTRODUCTION

In 1976 the publication of the first observation of a significant polarization of inclusively produced Λ^0 appeared [1]. Since that time, the lambda has been the most reported hyperon showing a significant polarization [1, 2, 3, 4, 5, 6, 7, 8, 9, 10, 11, 12, 13, 14, 15, 16, 17, 18]. Polarization is not a property of just lambda's, other hyperons have been seen to have large polarizations: $\Sigma^-, \Sigma^+, \Sigma^0, \Xi^0, \Xi^-$, and Ω^-[7, 19, 20, 21, 22, 23, 24, 25, 26, 27, 28, 29, 30]. Many models have been developed in an attempt to explain this process, but none have been completely successful.

A theoretical model of polarization based on first principles has never been developed. Part of the problem is that polarization is a long range phenomena and as such can not be described by perturbative QCD. Many phenomelogical models have been developed which are able to model polarization in specific interactions or for a sub-set of interactions. However, there is still no generally accepted mechanism [31, 32] that can explain all the various observed polarizations.

The discovery [30, 33] that some anti-hyperons $\bar{\Xi}^-$ and $\bar{\Sigma}^-$ are produced polarized prevents polarization from being modeled as a purely valence quark phenomena [34, 35]. With current theoretical understanding being unable to account for polarization and with current models also finding limited success, more experimental information will hopefully give new insights into the mechanism of polarization.

To date, most experimental results on polarization used interactions of protons and nucleons. Other experiments have used pions [6, 7, 8] and Kaons [10, 11, 12] as the primary beam. Only one other experiment used a Σ^- beam to measure polarization, WA89[19]. The K and Σ^- results are very interesting since in these experiments the s quark is a valence quark. In the kaon data, the s quark is the only valence quark, but with a Σ^- beam, the s quark may bring a second quark with it. This possibility allows for a deeper probe of how polarization might develop.

Experiment E781 (SELEX) is the second measurement of the inclusive polarization of Λ^0 produced by a Σ^- beam. This analysis is measured at nearly double the beam energy and at higher values in x_f.

CHAPTER 2.

EXPERIMENTAL AND THEORETICAL REVIEW

Polarization is the tendency for a particle to decay non-isotropically in it's center of mass frame. In the simple case of a two-body decay, (such as $\Lambda^0 \to p + \pi^-$), if there exists a net parent polarization P_Λ, then in the rest frame of the Λ^0:

$$\frac{dN}{d\Omega} = \frac{1}{4\pi}(1 + \alpha P_\Lambda \cdot \hat{k}_{proton}) \tag{2.1}$$

where the polarization is measured along the $\hat{k}_{beam} \times \hat{k}_\Lambda$ direction, $\hat{k}_{beam}$ is the unit momentum vector of the beam particle and α is the asymmetry parameter. The α parameter arises from the interference of s wave (parity violating) and p wave (parity conserving) amplitudes. In the general process $\frac{1}{2}^+ \to \frac{1}{2}^+ + 0^-$, both s and p wave amplitudes are contained. If the normalization is specified by the transition rate , $= |S|^2 + |P|^2$, then the decay parameters are defined by , $\alpha = 2\mathrm{Re}SP^*$, , $\beta = 2\mathrm{Im}SP^*$, and , $\gamma = |S|^2 - |P|^2$. Since $\alpha^2 + \beta^2 + \gamma^2 = 1$, the two parameters α and $\Phi = \arctan\left(\frac{\beta}{\gamma}\right)$ are generally used. Table 2.1 gives various data regarding hyperons and Table 2.2 gives decay parameters for hyperons.

Although many models have been created in an attempt to model the ob-

Table 2.1: Properties of the Hyperons [36]

Particle	Mass (Mev/c^2)	Lifetime (s)	Decay Length ($c\tau$)
Λ	1115.684 ± 0.006	$(2.632 \pm 0.020) \times 10^{-10}$	$7.89cm$
Σ^+	1189.37 ± 0.07	$(0.799 \pm 0.004) \times 10^{-10}$	$2.396cm$
Σ^0	1192.55 ± 0.08	$(7.4 \pm 0.7) \times 10^{-20}$	$2.22 \times 10^{-9}cm$
Σ^-	1197 ± 0.033	$(1.479 \pm 0.011) \times 10^{-10}$	$4.434cm$
Ξ^0	1314.9 ± 0.6	$(2.90 \pm 0.09) \times 10^{-10}$	$8.71cm$
Ξ^-	1321.32 ± 0.13	$(21.639 \pm 0.015) \times 10^{-10}$	$4.91cm$
Ω^-	1672 ± 0.29	$(0.822 \pm 0.012) \times 10^{-10}$	$2.46cm$

served polarization results, only two models have met with moderate success: The Lund Model and the DGM Model. A recent model based on perturbative QCD [37, 38] has only been applied to proton data.

Most models start with a valence quark picture and expand upon it. This picture is shown for proton beams in Fig. 2.1 with the observed polarizations for the hyperons shown. Fig. 2.2 shows this picture for Σ^- beams with the results of WA89 [19] shown for the observed polarizations of the hyperons. The main features of this picture are that the resulting hyperon is formed first from the available valence quarks (V) and secondly from the quarks which reside in the sea (S). In addition, two quarks of the same type (valence or sea)

Table 2.2: Decay Properties of the Hyperons [36]

Particle	Decay Mode	α	Φ
Λ	$p\pi^-(63.9 \pm 0.5)\%$	$+0.642 \pm 0.013$	$(-6.5 \pm 3.5)^\circ$
	$n\pi^0(35.8 \pm 0.5)\%$	$+0.648 \pm 0.044$	
Σ^+	$p\pi^0(51.57 \pm 0.30)\%$	-0.980 ± 0.017	$(36 \pm 34)^\circ$
	$n\pi^+(48.31 \pm 0.30)\%$	$+0.068 \pm 0.013$	$(167 \pm 20)^\circ$
Σ^0	$\Lambda\gamma(100)\%$		
Σ^-	$n\pi^-(99.848 \pm 0.005)\%$	-0.068 ± 0.008	$(10 \pm 15)^\circ$
Ξ^0	$\Lambda\pi^0(99.54 \pm 0.05)\%$	-0.411 ± 0.022	$(21 \pm 12)^\circ$
Ξ^0	$\Lambda\pi^-(99.887 \pm 0.035)\%$	-0.293 ± 0.007	$(4 \pm 4)^\circ$
Ω^-	$\Lambda K^-(67.8 \pm 0.7)\%$	-0.026 ± 0.026	
	$\Xi^0\pi^-(23.6 \pm 0.7)\%$	$+0.09 \pm 0.14$	

form a diquark. Under this model, valence quarks have positive polarization and sea quarks have negative polarization. The resulting net polarization is a result of the combined quarks. In the case of $\Sigma^- + N \to \Lambda^0 + X$, since two valence quarks are in common, this is a VVS process and the 'naive' assumption is the net polarization would be postive. If only one quark were in common, it would be a VSS process and if no quarks are in common (such as with anti-particles) it is a SSS process. This 'naive' model works well in some cases but breaks down with the experimental results of polarization in anti-particles. Never-the-less, it is still the basis of the two most successful models.

2.1 Lund Model

In the Lund Model [39, 40], the mechanism that produces the Λ^0 polarization from an incident proton, is basically a soft process, where sea $s\bar{s}$ pairs are produced by a tunneling process through a classically forbidden region in the color field before entering the outgoing hyperon's wave function, and where perturbative QCD is not applicable. The main assumptions of the model are:

- A color dipole field is stretched between the diquark (S=0, I=0) of the incoming proton and the central collision region , and an $s\bar{s}$ pair is produced in this field.

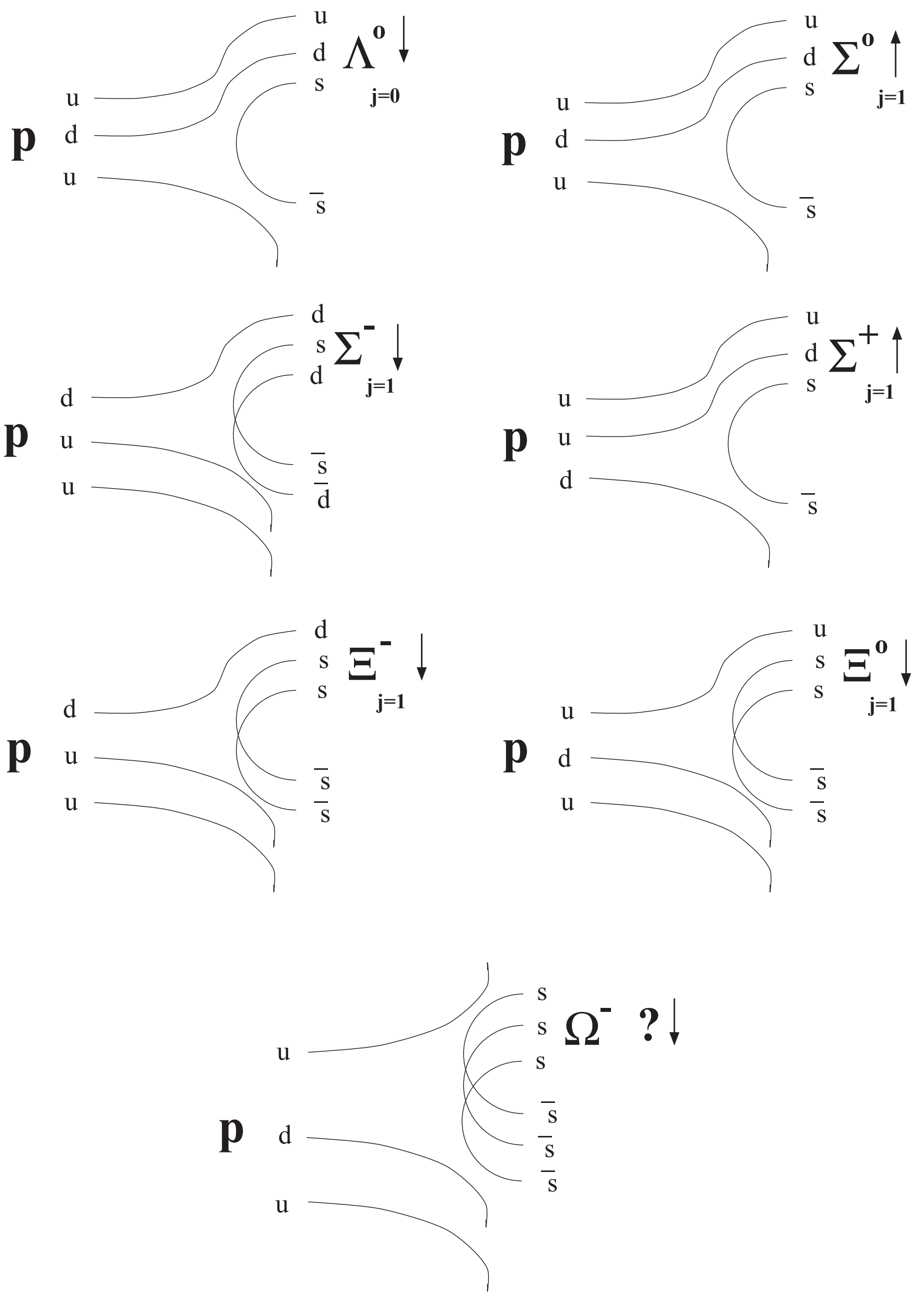

Figure 2.1: Valence quark model of polarization for proton induced hyperons

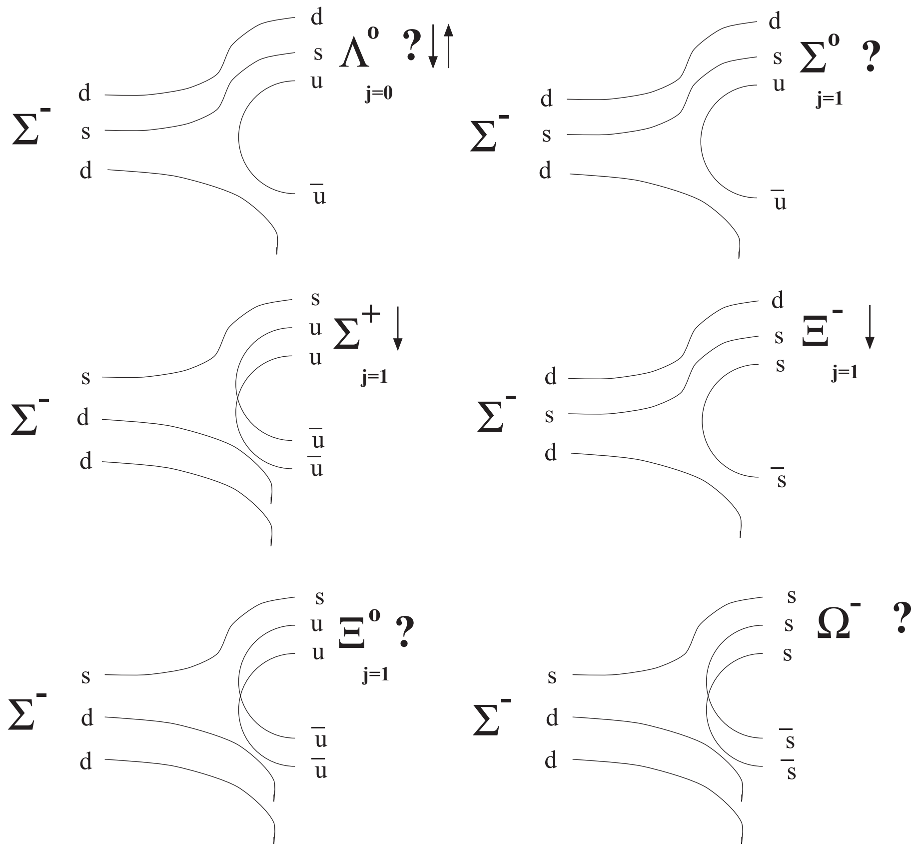

Figure 2.2: Valence quark model of polarization for Σ^- induced hyperons

- The transverse momentum is locally conserved in the string force-field. This field has no transverse degrees of freedom and hence the $s\bar{s}$ pair is produced in a state with equal and opposite transverse momenta.

The total transverse momentum of the Λ^0 is made up of the transverse momentum of the pair ud (perpendicular to the beam), which determines the direction of the force-field string and the transverse momentum of the s-quark which is measured with respect to the string direction. Since the s-quarks have mass, the s and $\bar{s}$ must be produced at a certain distance from each other in order to conserve momentum and energy. Thus the energy in the force field in between them can be transformed into transverse mass of the pair. This causes the appearance of an orbital angular momentum perpendicular to the string. The assumption of the model is that this orbital angular momentum ($L \leq 1$) is compensated by the spin of the $s\bar{s}$ pair.

Putting this altogether, the model predicts, the Λ^0 polarization is perpendicular to the plane defined by the incoming beam and outgoing Λ, and it increases with with the transverse momentum of the hyperon up to around 4GeV/c. The main limitation of this model is it's failure to include the contribution of a (polarized) leading parton to the polarization asymmetry of the hyperon.

2.2 DGM Model

In the DGM Model [34, 35], the hyperon polarization is due to a Thomas precession effect during the quark-recombination process. In this model, the valence quarks carry almost all of the beam particles momentum, while the sea partons account for only a small fraction. This proposed recombination process is based on the following:

- Produced hyperons use all available valence quarks.
- The baryons are described in terms of SU(6) wave functions and are treated as bound states of a quark and a di-quark.
- Quarks which must slow down (valence quarks) combine with their spin up and quarks which must speed up (sea quarks) combine with their spin down.

The last point can best be illustrated by looking at the case $p \to \Lambda$[34]. In this case, the s quark involved in the recombination resides in the sea of the proton and carries a very small fraction x_s (≈ 0.1) of its momentum. However, it is a valence quark in the Λ and must carry a large fraction of the $\Lambda' s$ momentum. Since the Λ also carries a large fraction (x_f) of the proton's momentum, recombination induces a large increase in the longitudinal momentum of the s quark, from $x_s P$ to $\frac{1}{3} x_f P$. At the same time, the s quark carries transverse momentum. Therefore, the velocity vector of the s quark is not parallel to the change in momentum induced by recombination and hence will feel the effects of Thomas precession [35].

An additional term will appear in the effective Hamiltonian which describes the recombination process:

$$U = \vec{S} \cdot \vec{\omega}_T \tag{2.2}$$

with the Thomas frequency

$$\vec{\omega}_T = \frac{\gamma}{\gamma + 1} \frac{\vec{F}}{m_s} \times \vec{V} \tag{2.3}$$

where $\vec{V}$ is the strange quark's velocity, $\vec{F}$ the force and m_s is the strange quarks mass.

Table 2.3 shows the predictions of the DGM model assuming an unpolarized beam and the two free parameters in the model are equal ($\epsilon = \delta$). Table 2.3 shows the polarization for the beam fragmentation region. No predictions in the target fragmentation region are made using the DGM model. The results of this analysis are included along with the results from WA89.

2.3 Experimental Results

The majority of experiments which have measured the inclusive polarization of Λ^0, have by the nature of their experiment, done so at fixed targeting angles. With a fixed targeting angle there is a direct correspondence between p_t and x_f of the Λ^0. Therefore the dependence of the polarization on both

Table 2.3: DGM Model Predictions for Polarization [34, 35]

Transition	Predicted polarization	Observed polarization	Energy (GeV/c)
$p \to \Lambda$	$-\epsilon$	-0.1 to -0.2	$24 - 2000$
$p \to \bar{\Lambda}$	0	0	$24 - 2000$
$p \to \Sigma^+$	ϵ	0.1 to 0.2	400
$p \to \Sigma^0$	ϵ		
$p \to \Sigma^-$	$\epsilon/2$	0.15 to 0.3	400
$p \to \Xi^0$	$-\epsilon$	-0.1 to -0.2	400
$p \to \Xi^-$	$-\epsilon$	-0.1 to -0.2	400
$K^+ \to \Lambda$	ϵ	$> 0.4, x_f > 0.3$	$32, 70$
$K^- \to \bar{\Lambda}$	ϵ	0.4	14
$\pi^- \to \Lambda$	$-\epsilon/2$	-0.05	18
$\Sigma^- \to \Lambda$	$-\epsilon/2$	-0.05 to 0.2	$376 - 610$

of these variables has been folded together. This co-dependence has been unfolded in fixed target experiments by measuring the polarization of proton induced $\Lambda's$, for a large number of incident angles [15], and for Σ^- induced $\Lambda's$ by using a 0^o targeting angle [19]. For collider experiments, this was done by measuring the polarization over a large apparatus acceptance [14]. In these results, the co-dependence was unfolded by using a 0^o targeting angle. Table 2.4, and Fig. 2.3 presents the results for E704 for a polarized proton beam of momentum 200 GeV/c [41] . Table 2.5, and Fig. 2.4 presents the results for R608, a collider experiment at the CERN ISR for proton-proton interactions [14]. Table 2.6, and Fig 2.5 presents the results for WA89 for Λ^0, Σ^+, and Ξ^- polarization produced by a Σ^- beam [19].

One common feature of the experiment results shown, is the increasing polarization until around $p_t \approx 1.0 GeV/c$. From that point, the polarization appears to be independent of p_t or decreasing as p_t increases above $1.0 GeV/c$. The current models all suggest that the polarization should vanish for large p_t. Large p_t in general is considered to be greater than $5.0 GeV/c$. No experimental data exits at the larger p_t values.

Other features of the experimental results includes the linear dependence on x_f. This has been seen in virtually all of the experimental results to date. In addition, the polarization appears to depend weakly on the target type. Energy dependence has been observed for some hyperon polarizations but

Table 2.4: Polarization of Λ^0 at 200 GeV/c [41]

x_f interval	p_t interval	$< p_t >$ (GeV/c)	polarization (%)
0.2-1.0	$0.1 - 0.3$	0.23	-7.7 ± 3.2
	$0.3 - 0.45$	0.38	-11.8 ± 2.3
	$0.45 - 0.6$	0.52	-12.0 ± 2.1
	$0.6 - 0.8$	0.69	-21.6 ± 2.0
	$0.8 - 1.0$	0.89	-30.7 ± 2.8
	$1.0 - 1.3$	1.11	-32.8 ± 4.3
	$1.3 - 2.0$	1.43	-28.5 ± 11.4

not for the Λ^0 [16].

Table 2.5: % Polarization of Λ^0 at $\sqrt{s} = 62\ GeV/c$ [14]

	$< p_t > (GeV/c)$					
$< x_f >$	0.41	0.60	0.76	0.89	1.02	1.26
0.25	-2.7 ± 1.0	-5.6 ± 0.9	-5.8 ± 1.4	-5.1 ± 1.9		
0.38	-2.7 ± 1.0	-7.5 ± 0.8	-11.8 ± 1.1	-13.6 ± 1.3	-15.9 ± 1.5	-14.8 ± 1.5
0.58	-4.6 ± 2.9	-7.3 ± 1.4	-14.9 ± 1.7	-20.0 ± 1.9	-24.8 ± 2.3	-25.4 ± 2.2
0.77		-15.1 ± 4.2	-21.9 ± 4.0	-29.7 ± 4.3	-37.1 ± 5.0	-37.5 ± 4.6

Table 2.6: % Polarization for Σ^- produced hyperons at 330 GeV/c [19]

	Polarization (%)		
$< p_t >$	Λ^0	Σ^+	Ξ^-
(GeV/c)	$< x_f >= 0.30$	$< x_f >= 0.27$	$< x_f >= 0.31$
0.2	0.002 ± 0.005	0.010 ± 0.034	-0.019 ± 0.040
0.46	-0.004 ± 0.004	-0.025 ± 0.020	0.001 ± 0.027
0.73	-0.005 ± 0.004	-0.045 ± 0.022	-0.055 ± 0.030
1.03	-0.022 ± 0.008	-0.031 ± 0.023	-0.090 ± 0.041
1.32	-0.055 ± 0.015	-0.051 ± 0.035	-0.092 ± 0.064
1.8	-0.033 ± 0.020		-0.121 ± 0.091

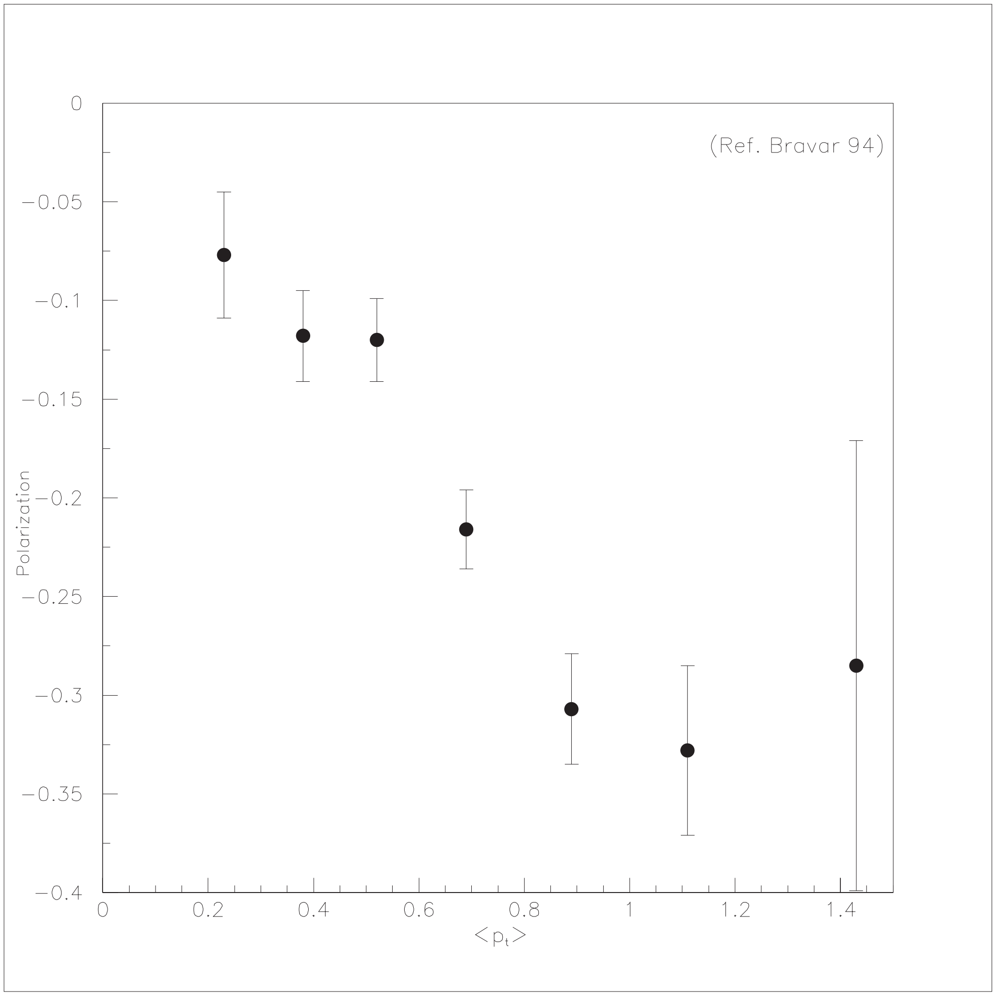

Figure 2.3: Λ^0 Polarization from Experiment E704 [41]

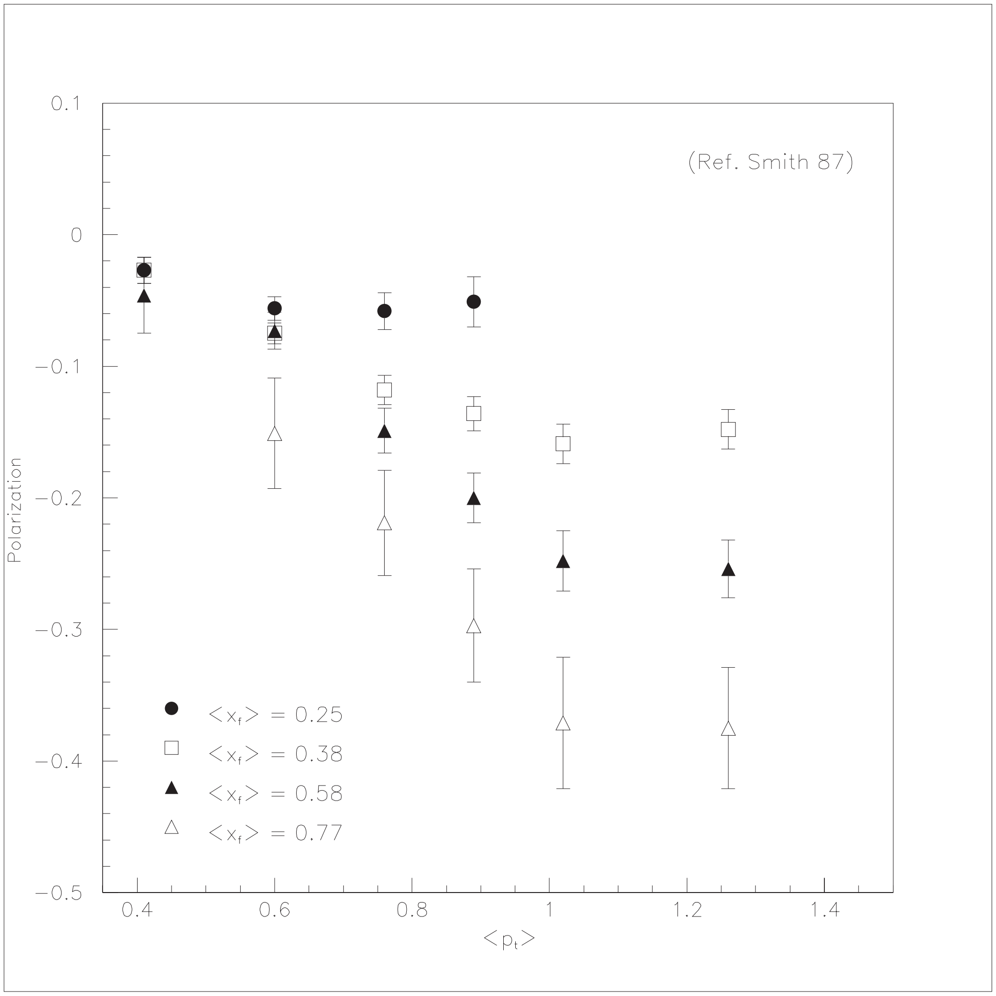

Figure 2.4: Λ^0 Polarization from Experiment R608 [14]

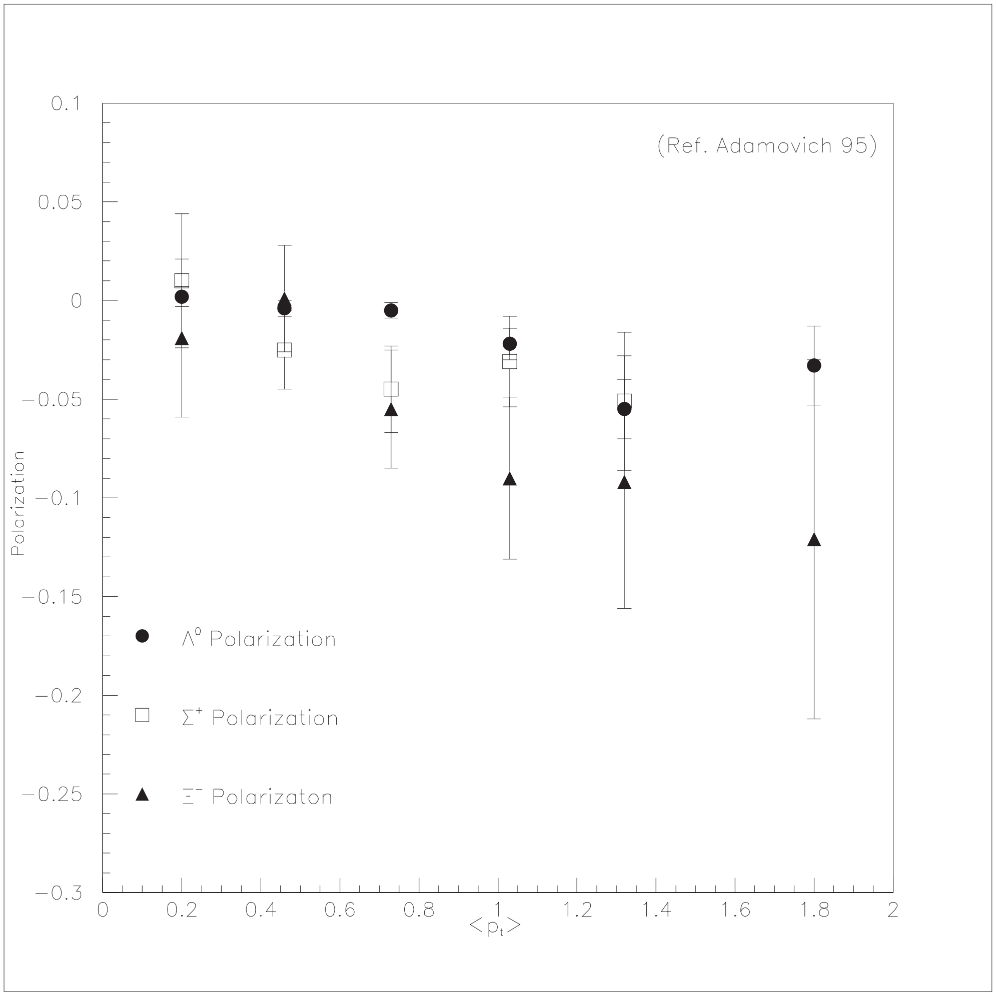

Figure 2.5: Hyperon Polarizations from Experiment WA89 [19]

CHAPTER 3.

THE DETECTOR

SELEX (SEgmented LargE X baryon spectrometer) was mainly designed for the high-statistics study of charm-baryons at large x_f. Charm-baryons are hadrons containing at least one charm quark. In addition to charm-baryons, other topics were of interest: Primakoff physics, Hyperon radiative decays, exotic mesons, hyperon electron scattering, etc. To accomplish these goals, the SELEX detector was a five-stage spectrometer, the layout of which is shown in Fig 3.1 and Fig 3.2. The five spectrometers were the Beam, Vertex, M1, M2 and M3. Each spectrometer, except for the Vertex, contained a bending magnet and the associated particle detectors. The Vertex spectrometer did not contain a magnet as it was designed for high resolution tracking of particles near the interaction target and the subsequent vertex determination. Each of the spectrometers will be discussed with key components used for the polarization measurement expanded upon.

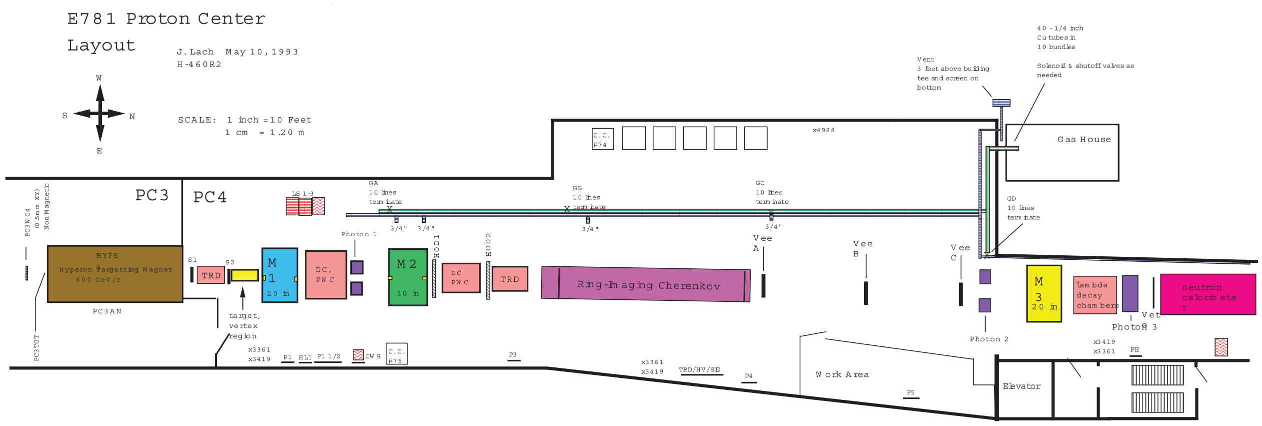

Figure 3.1: E781 SELEX Experimental Hall Layout

3.1 The Beam Spectrometer

The layout of the beam spectrometer is shown in Fig 3.3. The Beam spectrometer consisted of the hyperon production target, the Hyperon magnet, beam particle identification detectors, beam track detectors and scintillators used for the trigger.

3.1.1 Hyperon Production

The Tevatron at Fermilab produced an 800 GeV/c proton beam which was focused on the $1 \times 2 \times 400\ mm^3$ beryllium production target. The production target was 0.98% of an interaction length and was located at the entrance of the hyperon channel. Under normal conditions, the tevatron delivered $5 \times 10^{10}\ protons/second$ during a 20 second burst every minute. The proton beam spot size was on the order of $1mm$ full width at half-maximum. The hyperon channel was made of tungsten and was used to select particle of the desired momentum. In addition, it served as a beam dump for the non-interacting protons. The Hyperon magnet was $7.3m$ long and had a field strength of 3.5 Tesla. The magnet selected negative particles with a mean momentum of 610 GeV/c with an 8% spread. The radius of curvature of the tungsten channel was 619 m. The beam produced by the production target consisted of approximately 70% Σ^- and 30% π^- with a small fraction of Ξ^- and Ω^- in a total flux of 1×10^6 particles/second. Due to decays of the Σ^-, the produced beam changes to approximately 50% Σ^- and 50% π^- by the

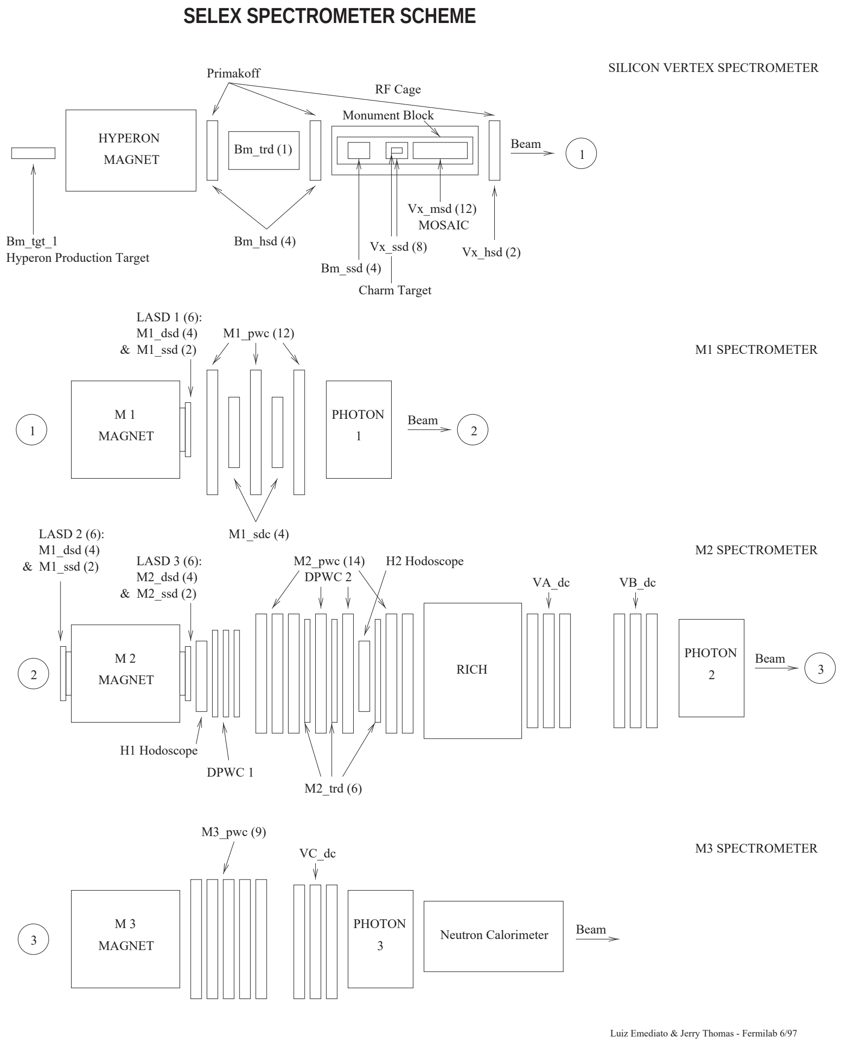

Figure 3.2: E781 SELEX Detector Layout

charm target. Once the beam left the hyperon magnet, it passed through the Beam Transition Radiation Detector (BTRD).

3.1.2 Beam Transition Radiation Detector (BTRD)

The BTRD consisted of 10 identical modules, each containing 200 polypropylene foils, 17 microns thick, separated by a 0.5mm gap and 3 multi-wire proportional chambers (MWPCs). The MWPCs consisted of aluminized mylar cathodes, 2 mm drift spaces and anode planes of 15 micron thick gold-plated tungsten wires spaced 1mm apart. The BTRD detected electromagnetic radiation emitted by charged particles as they traversed the boundary between media with different dielectric properties. A charge particle moving towards a boundary forms together with its mirror charge, an electric dipole, whose field strength varies in time, i.e. with the movement of the particle. The field strength vanishes when the particle enters the medium. The time dependent dipole electric field causes the emission of electromagnetic radiation. The use of 200 layers of polypropylene per module increased the amount of radiation emitted. The beauty of transition radiation was that the radiated energy, by transition radiation photons, increased with the Lorentz factor γ (i.e. the energy) of the particle, and not just its' velocity as C̃erenkov radiation detectors do. This enables it to be extremely valuable for the identification of relativistic particles ($\beta \rightarrow 1$) at high energies. Fig 3.4 displays a typical distribution of the number of planes activated when a

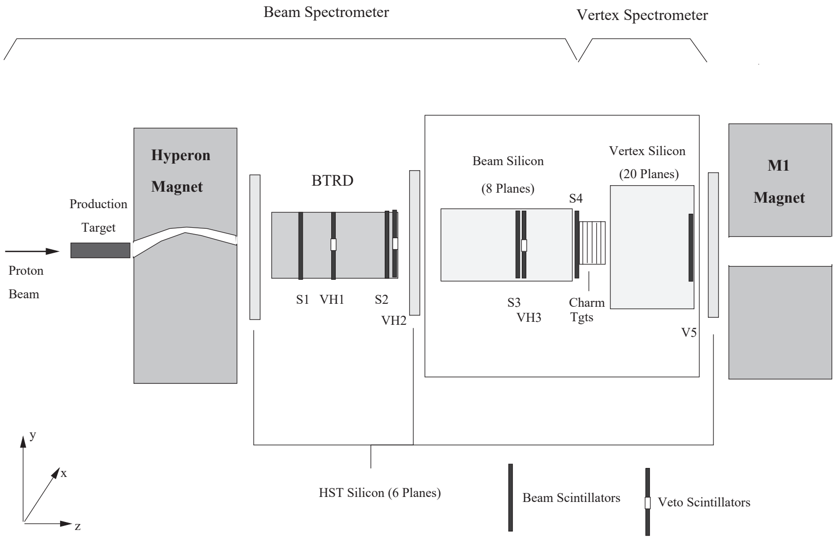

Figure 3.3: Beam Spectrometer

beam particle traversed the detector. The number of planes activated was directly proportional to γ, so for particles of equal momenta (Σ^- and π^-) the π^- activated more planes since its' mass is much less than that of the Σ^-. The cut on the number of planes used for this polarization measurement was $n \leq 4$. The efficiency for this cut in identifying Σ^- particles was greater then 95% for the selected events.

3.1.3 HST Silicon

After the Hyperon magnet, in front of the RF cage and before the M1 magnet were mounted 6 planes of silicon detectors as part of the the Hardware Scatter Trigger for Primakoff physics. These detectors were installed for Primakoff physics and were used as a supplement to other detectors for

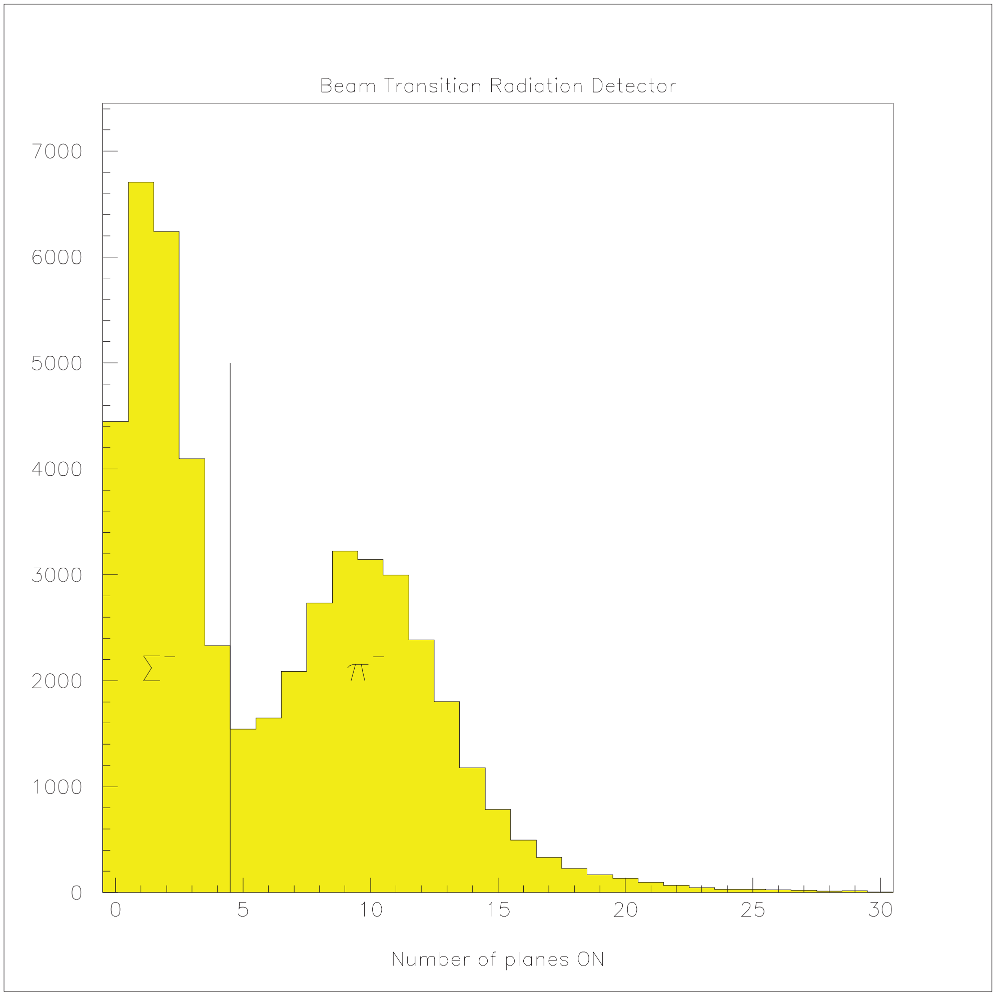

Figure 3.4: BTRD Planes active for beam particles

tracking purposes.

3.1.4 Beam Silicon

The Beam Silicon tracking detector consisted of 8 planes of 300 μm thick single sided silicon detectors. Each detector had an active region 2 × 2 cm^2. On the silicon, 1024 strips were implanted at 20 micron pitch. Each detector was read out via 8 SVX chips. Fig 3.5 shows the three stations of Beam silicon. The detectors were mounted on three stations with stations 1 and 3 containing 3 detectors and station 2 containing 2 detectors. The alignment procedure used to mount the detectors is discussed in Appendix B. Stations 1 and 3 contained x-view, y-view and u-view detectors. The hit efficiency for a single detector was $> 98\%$ with an overall tracking efficiency of $> 95\%$. The resolution of a single detector was $< 7\mu$m. Fig. 3.6 shows the output of the BSSD's near the end of the run. From this, hot channels, which are strips which are noisy, can be clearly seen. Also, the profile of the beam can be seen. The SVX chip used on the detector collected and stored the 'hit' information of the silicon strips. It used a variable integration gate. This gate could be set for up to 10 μs. Depending on the beam intensity and the gate setting, several beam tracks were stored in the SVX between readouts.

3.2 The Vertex Spectrometer

The Vertex Spectrometer consisted of the charm targets and the vertex silicon. It was designed to give high resolution of interactions within the

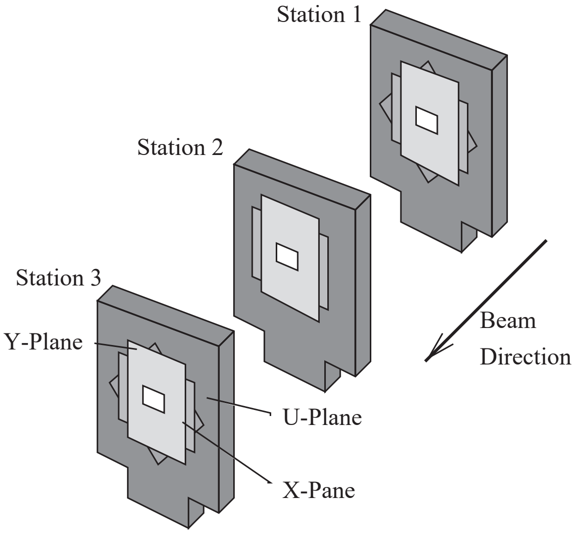

Figure 3.5: Beam Silicon Strip Detector Stations

charm targets as well as secondary vertices formed from the decay of charmed particles. The vertex spectrometer distinguished between the large number of particle tracks which resulted when a charmed particle was formed during the target interaction.

3.2.1 Charm Target

The charm target consisted of 2 copper blocks 1.6 mm, and 1.0 mm thick and 3 diamond blocks each 2.2 mm thick. The targets were separated along the beam line to allow determination of the target in which the interaction occurred. The targets were removed from the beam line remotely to allow alignment data to be taken using the non-interacted beam tracks.

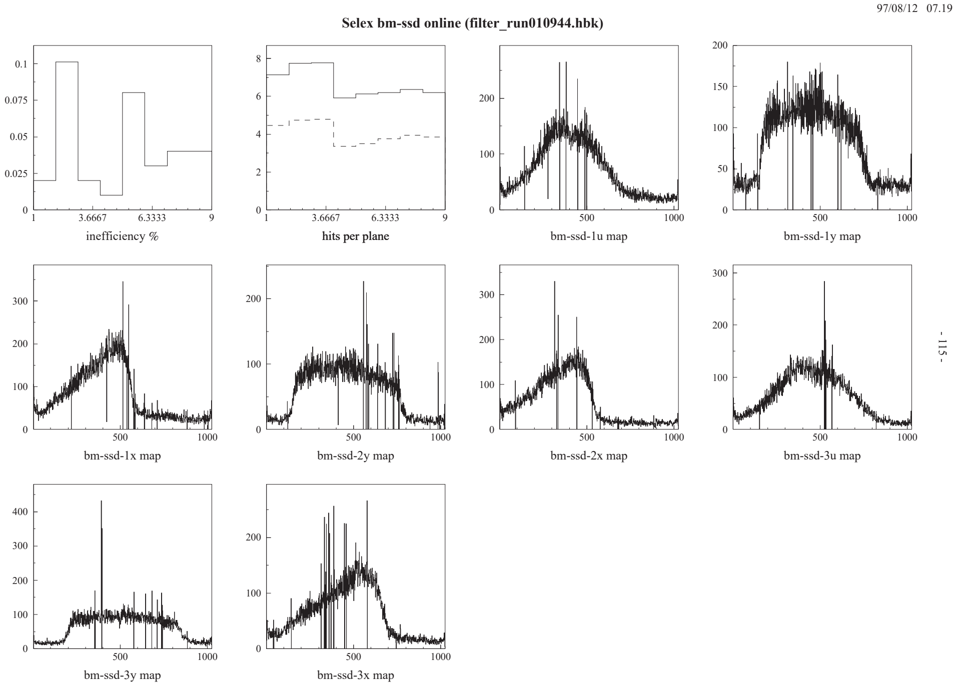

Figure 3.6: BSSD output

3.2.2 Vertex Silicon

The Vertex Silicon detector consisted of 20 planes of 300 μm thick single sided silicon detectors. The detectors were mounted on five stations with four detectors on each station. The 20 detectors were comprised of 6 x-view, 5 y-view, 4 u-view and 5 v-view detectors. The first two stations had an active region of 5.12×5.00 cm^2 with 2560 strips at a pitch of 20 μm. On these detectors, only in the central region of 1536 strips was every strip read out. In the outer regions, every other strip was read. The other three stations contain mosaic detectors. The mosaic detectors were a combination of three 8.3×3.2 cm^2 silicon detectors, each with a 25 μm pitch. The central detector had every strip read out while the outer detectors had every other strip readout. The single hit efficiency was 98% and the overall tracking efficiency was $> 95\%$ for these detectors.

The Beam silicon, Vertex silicon, charm targets and trigger scintillators were enclosed in a light-tight aluminum box for RF shielding. The layout inside the box is shown in Fig 3.7. The RF cage was also cooled with air chilled to 19 degF.

3.3 The M1 Spectrometer

The M1 spectrometer consisted of the M1 magnet and the detectors between the magnets M1 and M2. The layout of the M1 spectrometer is shown in Fig 3.8. The M1 spectrometer was designed to analyze particles in the 2.5

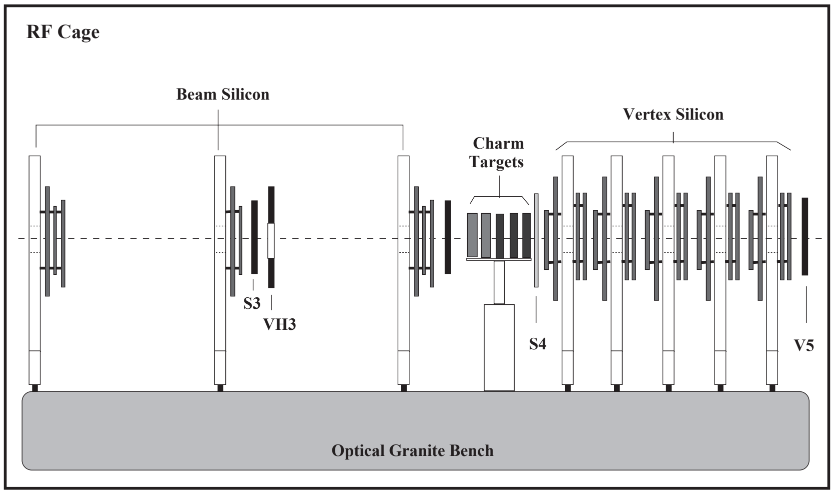

Figure 3.7: E781 RF Cage Layout

- 15 GeV/c momentum range. As such, the M1 magnet was operated with a field strength of $1.35T$ giving a p_t kick of 0.74 GeV/c. The M1 spectrometer used Proportional wire chambers and drift chambers to track these 'soft' particles. The high momentum or 'stiff' particles were also tracked though the spectrometer by means of high precision large area silicon detectors (LASD).

3.3.1 Large Area Silicon

Each Large Area Silicon detector consisted of two single-sided silicon detectors and two double-sided silicon detectors. Both types of silicon were 300μm thick with the single sided having an active area of 6.35×6.35 cm and the double-sided 5.26×6.64 cm. The double-sided detectors were employed to reduce the overall radiation length ($> 10\%$) already accounted for by the

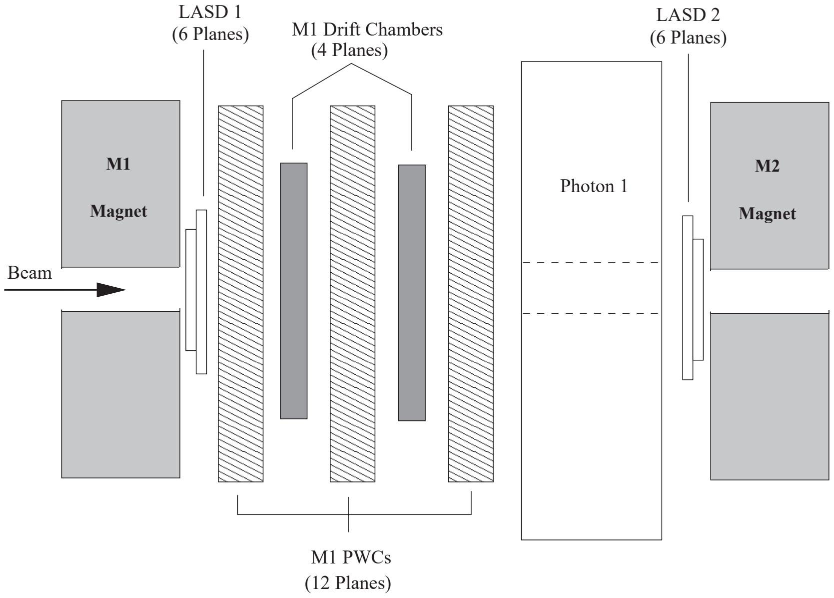

Figure 3.8: E781 M1 Spectrometer

other silicon detectors. The LASDs were mount on the end plates of the magnets and therefore were designed to function correctly in the fringe magnetic field. This created unique problems which required a separate cooling system, and special mounting structures to prevent flexing in the magnetic field and to reduce the amount of material in the beam line which could produce downstream interactions. Including the LASDs the total silicon system accounted for approximately $80,000$ channels of readout in the experiment.

3.3.2 M1 Proportional Wire Chambers

The M1 Multi-wire Proportional Wire Chambers (PWCs), were designed to track the 'softer' particles from the interaction. The PWCs consisted of equally spaced anode wires centered between two cathode planes. The chamber was filled 'magic gas' (75% argon, 24.5% isobutane, and 0.5% freon). The magic gas would ionize when a charged particle passed through it. The ionized gas consists of electrons and positively charged ions. The positive ions would drift in the electric field to the cathode and the electrons would drift to the anode. When the electrons are close to an anode wire, a process of avalanche formation occurs greatly increasing the signal collected by the wire. This signal was then readout and the wire position of the passing charged particle was determined. Each PWC consists of four planes of anode wires configure in x,y, u and v projections allowing for the position of the particle to be determined. The three chambers were positioned 70 cm apart and had an active region of $100 \times 100\ cm^2$. The anode wires were 2 mm apart giving a resolution of $0.6mm$.

3.3.3 M1 Drift Chambers

The two M1 drift chambers were placed between the M1 PWC's. Drift chambers use the fact that if the drift velocities of the ionized particles is held constant and known, and the time of passing of the particle is known, than a finer position resolution of the particle can be determined. The M1 drift chambers were used to obtain a finer resolution on track positions.

3.3.4 Photon 1

Photon 1 was a lead glass calorimeter. High energy electrons lose their energy almost exclusively by bremsstrahlung and photons their energy by electron-position pair production. This electro-magnetic shower was produced in the lead glass of the calorimeter. These particles in turn emitted C̃erenkov light which was collected by the photo-multiplier tubes. The integrated energy collect by the tubes could then be used to estimate the energy of the incident particle. One advantage of the use of lead glass calorimetry is their radiation hardness.

3.4 M2 Spectrometer

The M2 spectrometer was designed to track, and identify the 'stiff' ($>$ 15GeV/c) particles from the interaction. The M2 spectrometer is the M2 magnet and all detectors between the M2 and M3 magnets. The M2 magnet was operated at a field strength of 1.54 T which corresponds to a p_t kick of 0.845 GeV/c. The M2 spectrometer is shown in Fig 3.9. The first detector in the M2 spectrometer was the third LASD station. It was located at the exit to the M2 magnet and consisted of 2 single-sided and 2 double-sided silicon detectors.

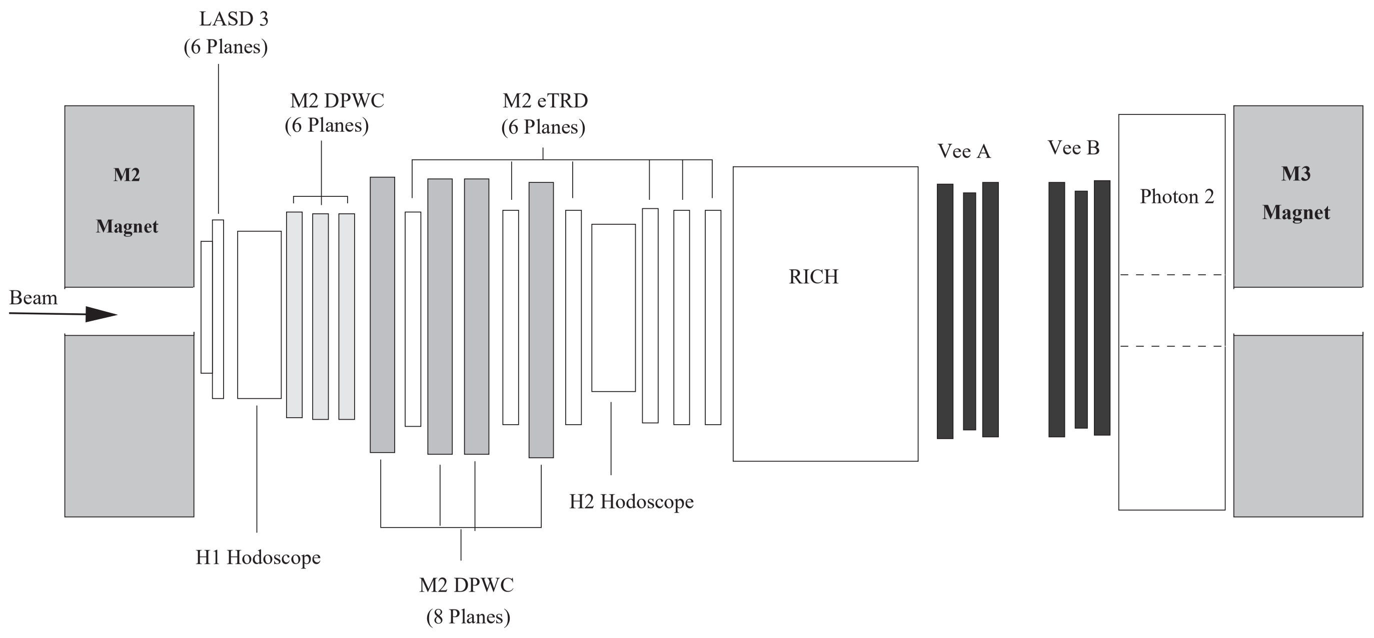

Figure 3.9: E781 M2 Spectrometer

3.4.1 Hodoscopes

The two hodoscopes employed in the M2 spectrometer used scintillation counters to give a fast response on the sign, number and momentum of particles passing through the spectrometer. This information was used by the trigger in deciding whether to trigger on an event. The hodoscopes consist of three regions covering the negative-charge, central and positive-charge regions of the M2 spectrometer. The sign of the charge was assumed based the region in the detector. The spectrometer magnets bent negatively charged particles to the right as they traveled down the beam line.

3.4.2 M2 Wire Chambers

Most of the tracking in the M2 spectrometer was done using the M2 PWCs and the M2 drift chambers. The first three stations of the M2 DPWCs were used in experiment E761. The first two stations are configured for (x,y) readout and the last station was configured for (u,v). These chambers had an active region of $60 \times 60\ cm^2$ and used magic gas. The M2 PWCs had and active region of $100 \times 60\ cm^2$ and consisted of 8 planes configured in pairs (x,y), (u,v), (x,y) and (x,y). These chambers also used a form of magic gas.

3.4.3 M2 eTRD

Interleaved within other detectors in M2 were the electron Transition Radiation Detectors (eTRD). The eTRD were specifically designed to give good electron identification. They used 200 sheets of 17 μm polypropylene foils and 2mm spaced collection wires to collect position information from the resultant transition radiation. The eTRD were 100×60 cm^2 and were all configured to give x-position information. The eTRDs were most efficient at distinguishing between electrons and pions at lower momenta (20 GeV/c). The eTRDs were found to be 95% efficient in this region and 91% efficient for typical electron momenta during the run.

3.4.4 E781 RICH

The E781 Ring-imaging C̃erenkov detector (RICH) provided most of the particle identification for the experiment. The RICH provided separation of pions, kaons and protons up to 200 GeV/c [42]. The RICH was a 10m long cylindrical vessel with a diameter of 2.34m. The vessel was filled with neon, a noble gas, to provide a clear signal. The downstream end of the vessel consisted of 16 hexagonally shaped spherical mirrors of total area $2.4m \times 1.2m$ with focal length of 10m. The mirrors were used to reflect the C̃erenkov photons back to an array of 2848 photo-multiplier tubes position at the upstream entrance of the vessel. The triggered photo-multipliers were then fit to circles and if the momentum of the track was known, the particle could be identified with varying levels of certainty.

C̃erenkov radiation is emitted when a charged particle traverses a medium with refractive index n with a velocity v exceeding the velocity of light c/n

in that medium. C̃erenkov radiation is emitted because the charge particle polarized the atoms along its track so that they become electric dipoles. The time variation of the dipole field leads to the emission of electromagnetic radiation. As long as $v < c/n$, the dipoles are symmetrically arranged around the particle's path, so that the dipole field integrated over all dipoles vanishes. If the particle moves with $v > c/n$, then the symmetry is broken and a non-vanishing dipole moment results. The opening angle of the resulting cone is related to the particle's velocity by

$$\cos\Theta_c = \frac{1}{n(\omega)\sqrt{1-\frac{1}{\gamma^2}}} \tag{3.1}$$

where ω is the frequency of the emitted radiation and γ is the relativistic Lorentz factor. This angle corresponds to the radius of the light-cone as seen by the photo-tubes in the detector.

3.4.5 Vector Drift Chambers

After the RICH were two of the three vector drift chambers (VDC). Most of the detectors in the SELEX spectrometer provided position information. The VDCs, on the other hand, were drift chambers designed to provide short track segments of charged particles in addition to the usual position information. These detectors consisted of a fine cell region centered around the beam line and a coarse cell region away from the beam. The VDCs were designed to track downstream decay products by providing high resolution,

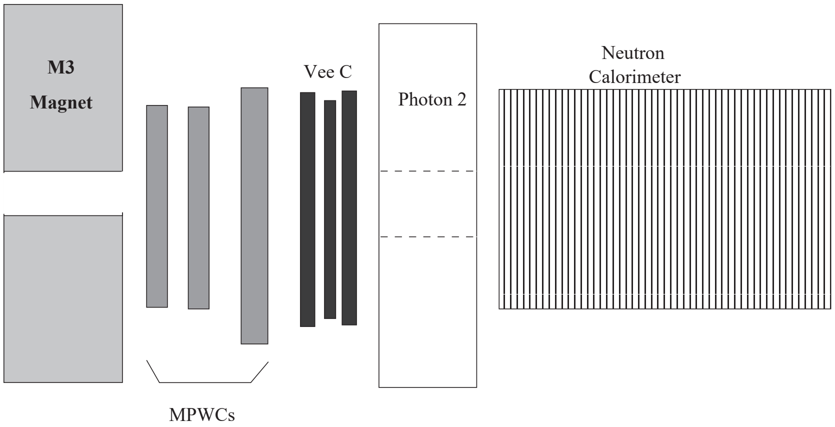

Figure 3.10: E781 M3 Spectrometer

short track segments within each station. Each station consisted of three axes (x,y,u/v). The chambers had an active region of $1.16 \times 1.16\ m^2$ with the fine cells providing 8 sense wires for each view and the coarse cells providing 6 sense wires. After the second VDC station was the second photon detector.

3.5 M3 Spectrometer

To measure the momentum of decay products for long-ranged hyperons, a third spectrometer was employed. The M3 magnet had a field strength of 1.3T providing a p_t kick of 0.72 GeV/c. The M3 Spectrometer is shown in Fig 3.10. The M3 spectrometer consisted of two MWPCs of $64 \times 64\ cm^2$, a third MWPC of $115 \times 89\ cm^2$, followed by the third VDC, the third photon detector and the neutron calorimeter.

3.5.1 Neutron Calorimeter

The final detector in the SELEX scheme was the neutron calorimeter (NCAL). The NCAL was designed to distinguish between beam particles and decay product neutrons. The NCAL consisted of 50 scintillator planes sandwiched between 50 iron sheets and 17 PWCs.

CHAPTER 4.

THE SELEX TRIGGER

The primary trigger configuration used for SELEX was called the charm trigger [43]. It was designed to study the production and decay of charmed baryons. The charm trigger had three levels of the hardware trigger, referred to as T0, T1 and T2. The purpose of the hardware trigger was to select interactions with a topology favorable to charm events while rejecting all other events. Charm events show a high number of charged particles produced by the interaction, whereas many non-charm events, such as a non-interacting beam track, contain low numbers of charged particles.

The purpose of T0 was the initial identification of trigger primitives and synchronization of higher levels. A beam scintillator was used to identify beam particles and the beam particles were used in the synchronization of the trigger levels. Cuts were made on dead-time, multiplicity, and number of beam particles. A positive decision at this level sent a tag to T1.

T1 accepted a BTRD (Beam Transition Radiation Detector) tag to determine the beam type along with a T0 tag to start the trigger level processes. The TDC gate and the ADC's were generated at this stage. Cuts were made on the beam definition and number of hits in the positive regions of the H1 hodoscope. T2 received a tag if a positive decision was reached at T1.

At T2 the hodoscope matrix was be applied. This took the hits in H1 and H2 and cuts on the possible hits in H2 for which there was a hit in H1 with a positive track extrapolating back to the target vertex. A tag from T1 was required to begin the level tasks, it started reading the data from the detectors into the Data Acquisition (DAQ) when a positive T2 decision was made.

The trigger was synchronized with the beam. Each level took a tag from a positive decision at the previous level and asserted the busy. This occurred from T0 to T2 until either a negative decision was reached or T2 gave a positive decision reading the detector data into DAQ. When either occurred, the level completed and terminated its processes and reset it's gate generator passing the clear back to the previous level until the T0 gate reset, ready for the next spill.

4.1 Trigger Synchronization

Each level of the trigger received a tag from the previous level in order to start its processing. In the case of T0, this tag came from the beam gate signaling when the beam was on or off spill. The level became busy and held the busy until its processes had finished and a level decision had been reached. If a negative decision was reached then the gate reset after the level had finished its tasks and the clear was passed back to the previous level, or in the case of T0 the busy was released ready for the next event. For a positive level decision the busy was passed on to the next level and the process was repeated until either a negative decision was reached at one of the levels or until a positive decision was formed at the T2 level and the detector data was read into DAQ. In this case a busy was also held by the detector systems being read to DAQ. Upon completion T2 reset and passed the clear to T1 and eventually to T0 as in the case of a reset from a negative decision. Synchronization between trigger levels was achieved by a synchronization signal confirming the logic was ready. Programmable Logic Units (PLU's) were the decision makers so the synchro-option could be used for this purpose.

4.2 T0 Logic

At the T0 level what was required was a defined incoming beam and multiple particles emerging after the charm targets. Hence, the beam scintillators should have been at the level of 1 particle, the veto scintillators should have be zero and the interaction counter and V5 should have shown multiple charged particles.

The programming of the T0 trigger was accomplished though the control of primitives. There could be up to eight T0 primitives each corresponded to an output bit of an Octal Logic Module (8LM). Each primitive bit was matched with the appropriate multiplicity bit and an OR was made to give the T0 decision. When a positive decision was reached a tag was sent to the T1 gate generator and the busy was passed on. If a negative decision was reached the busy remained at this level as it completed its processing and reset it's gate generator. The cut on multiplicity was made from the S4 interaction counter and the V5 beam scintillator. This cut selected a multiplicity greater than one.

The beam particles were identified using a beam scintillator referred to as V5 and the S3 interaction counter was used to synchronize the trigger. A cut on V5 pulse height was made to allow 20% of beam particles to pass. This prevents the interaction of more than two particles. T0 is prescaled to let the nth T0 decision to pass regardless of whether it would give a positive decision or not because this serves as a control for the experiment by giving a set quota of straight through beam particles. This could be used to check the trigger, comparing to previous trigger versions and also provided some events for alignment. Cuts on beam definition were made by the S1, S2 and S3 beam scintillators and the VH1, VH2 and VH3 veto counters. This was made at the S_logic 8LM (Octal Logic Module).

A cut was made on dead-time, this occurred at the B_logic module of T0 after a delay of 10μs with a zero fast-clear reading at the T0_srs PLU. This was to reset the system if there was a sufficiently long time without beam. This occurred when the 4th pulse reached the T0 Beam strobe.

A PLU-8 (eight bit PLU) used the T0 pattern to synchronize the Silicon Vertex (SVX) fast-clear and to strobe the T1 gate. A PLU is a memory unit that can store a set of bits. The bits were read in until the module was strobed, locking it, storing the data held when it was strobed. PLU's were the decision makers and locked until reset by either a negative decision on the present level or until the clear was returned from the next level.

The trigger was synchronized to the beam by using the S3 counter to identify the timing of the beam particles. The S counters covered a 15ns window with the veto counters covering a 5ns margin on either side of this window. Interactions completely within the window were accepted, those registered in the vetoes were rejected. The S3 counter was shifted 5ns later and combined with the rest of the S counters to give the timing of the beam. This phase locking was the ARF (Accelerator Radio Frequency) which was typically at 53MHz, synchronous with the beam so the readout was clocked in phase with the beam.

4.2.1 SVX Fastclear

T0 interacted with the Silicon Readout Sequencer (SRS) to provide the synchronization for the clear and readout operations of the Silicon Strip Detectors (SSD). The SRS took a positive T1 result and froze the SSD for readout at a positive decision from T2 to DAQ. The SVX integrated charge from all tracks until readout or clear occurred. A clear was required when there were more than three beam particles, if a readout occurred or if 10μs passed without an event.

The used a Field Effect Transistor (FET) short to discharge the capacitor across which the charge integration of the SVX occurred. This cleared any charge from a previous event, readied for the next collection and kept the capacitor clear when there was no beam.

4.3 T1 Logic

This stage was enabled by a positive decision at T0. It identified target interaction from the interaction counters and accepted a BTRD tag to select beam type. The hits in H1 were counted. For the charm trigger, the BTRD required a Σ beam, there must have been two positive hits in H1 and the interaction counters must have shown hits that can be extrapolated back from H1 to the target vertex.

The T1 decision reached from the above cuts was sent through an AND with the T0 decision to give the final T1 decision. For a positive decision, a tag was sent to T2. If the decision was negative then the level finished all processes and passed the clear back to T0.

4.4 T2 Logic

The T2 level contained the hodoscope matrix and the photon 3 energy sum, and was used to initiate reading of data from the detectors into DAQ when a positive T2 decision occurred. When a positive decision was reached by the matrix the detector data was read into DAQ in the following streams: FSDA, TDC, CROS, SCC, CAMAC, ADC, RMH12 and RMH3. For a negative decision the level finished its processing and then returned the clear to T1.

4.4.1 The Hodoscope Matrix

The matrix read a hit in the positive region of H2 and asked for that hit "was there a hit in H1 with a track of the required momentum extrapolating back to the target vertex?".

The hodoscope matrix is found in the T2 section of the trigger and worked as follows:

- 'enableA' and 'enableB' are MLU's. Their role was to provide a set of enable bits for the H2 counters.
- 'matrixA' and 'matrixB' ANDed each H2 counter result with its enable bit.
- The 4508 PLU's were 8x8 bit PLU's programmed as 8bit line encoders. They counted the number of valid H2 hits in four momentum regions and convert each into a 3-bit binary.
- The 2373 MLU converted the binary inputs into a count of the total number of hits, then passed the binary to the matrix level decision PLU.
- The matrix level PLU was the matrix decision PLU. A multiplicity cut

> was imposed upon the 3a output, if this read a 1 or greater then the cut was imposed giving a negative T2. The binary from T1 was stored and the T2 inputs were strobed for a positive T1. A strobe from T0 to this PLU froze it and the clear came here for negative T1 decisions. The matrix interacted with T2 via the T2_ MLU.

When a particular hit occurred in H1, a corresponding set of possible hits in H2 was looked up in enableA/B and sent to matrixA/B respectively. This was ANDed with the actual hits in H2 and the results separated and sent out to PLU's to represent four momentum regions of the matrix. The four momentum regions, represent only the positive side, increasing in momentum as the center was approached. The results from these four regions were then coupled with the result of the T1 decision to give the T2 decision.

4.5 Other Triggers

Apart from the charm trigger there were several other triggers, namely; the HST (Hardware Scattering Trigger), the He (Hadron electron) trigger, and the HYP (Hyperon) trigger.

4.5.1 HST

This trigger was actually designed as part of T1. Its primary aim was to reject noninteracting beam. This was accomplished by a prediction of the beam coincidence at bm_hsd3 (beam HST silicon detector 3) being made from the tracks through bm_hsd1 and bm_hsd2. The logic of the HST then read a hit in station 3 and asks “is the hit on the predicted beam-line?”. If the result was positive the event was rejected, if it’s off the beamline then an interaction was implied. The logic then asked “are there corresponding tracks in the silicon stations that extrapolate back to a beam interaction.?”, a positive result here passed the event on to the rest of the trigger. Stations 1 and 2 were before the vertex while station 3 was after it.

A secondary role of the HST was to provide good time resolution for the beam silicon region. The beam silicon had good space resolution but accumulated data over a 10μs time period. The HST would do this in less than 100ns but at the loss of spatial resolution. The good time resolution of the HST was coupled with the good spatial resolution of the bm_ssd’s to improve the tracking of the beam silicon.

4.5.2 He Trigger

The aim of this trigger was to trigger on the scattering of beam particles with the electron cloud of the target atoms. The Interaction Counters (IC’s) were used to identify the two negative particles. The cut at this point was that there are two counts in both counters. H1 was used to find these particles. The cut was the same, that there were two hits in the negative region of the hodoscopes. The veto counters on H2, denoted as H2-61 to H2-64, were used to cut on the low momentum, large angle secondaries to reduce the trigger rate.

4.5.3 Hyperon Trigger

The hyperon trigger was designed to find the $\Sigma^{-*}(1385)\rightarrow$ $\Lambda^0\pi^-$. An effect of this was there should be one negative charge in the IC's. The BTRD cut on the beam definition to ensure a Σ was present. The Λ^0 further decayed $\Lambda^0 \rightarrow \mathrm{p}\,\pi^-$. So the $\mathrm{p}\,\pi^-\,\pi^-$ gave three tracks to be detected in the M2 hodoscopes. Therefore a cut of 3 particles was made in H1 with one of them (the proton) being in either the neutral of positive region and the other two (the pions) being in the neutral or negative region. A cut on trajectory angle was made in the H2-Veto counters (H2-61 to H2-64). This was because the $\Sigma^-*(1385)$ had a lot of energy which would propagate through the decay into the $\mathrm{p}\,\pi^-\,\pi^-$. So if the particles could be swept into the vetoes they were not likely to have enough momentum to have come from the Σ^{-*}.

4.6 Software Triggers

There were five basic types of trigger, namely; Interaction, Beam, G-pulser, Lpulser and Random.

4.6.1 Interaction

This was the standard trigger setup used to trigger on interactions in the charm target. It was used during beam with the spectrometer magnets on and the charm target in the beam.

4.6.2 Beam

Used to find beam particles in the S1, S2, S3 and NOT in V1, V2, V3 detectors. This type of trigger was used in alignment runs with the target out of the beam. It could be used only if beam was present.

4.6.3 Gpulser

Could be used regardless of whether beam was present or not. A pulse was generated through the system at a fixed frequency (ARF / prescaler).

This provided triggers asynchronous to the beam particles to search for noise within the SELEX detector.

4.6.4 Lpulser

This trigger used LED's to strobe the scintillators to emulate one particle passing through the experiment. This could only be done when there was no beam and was used in timing the trigger.

4.6.5 Random

This trigger was used when there was no beam to randomly trigger the chambers at a mean rate of 20μs. This tested chamber performance. 20μs was used because it was the same as the average interaction triggering rate. The scintillators were also randomly strobed with an LED, this could be used to check the trigger logic.

CHAPTER 5.

SOFTWARE

The software used in SELEX can be broken down into four major categories: Data Acquisition, Off-line Processing, Simulation and Data Analysis. Since the experimental hall was not accessible during the running of the experiment, all detectors had to be controlled remotely from the control area. This included the configuration of the detectors for all types of data collection, including calibration and testing. Most of the experiment was controlled using two Silicon Graphics computers. From these computers and the appropriate hardware connections, most systems could be accessed.

5.1 Data Acquisition

The data acquisition (DAQ) software was a diverse set of software. It included the embedded software used to control individual detector systems, the trigger subsystem, the control software and the online filter. A schematic of the DAQ is shown in Fig 5.1.

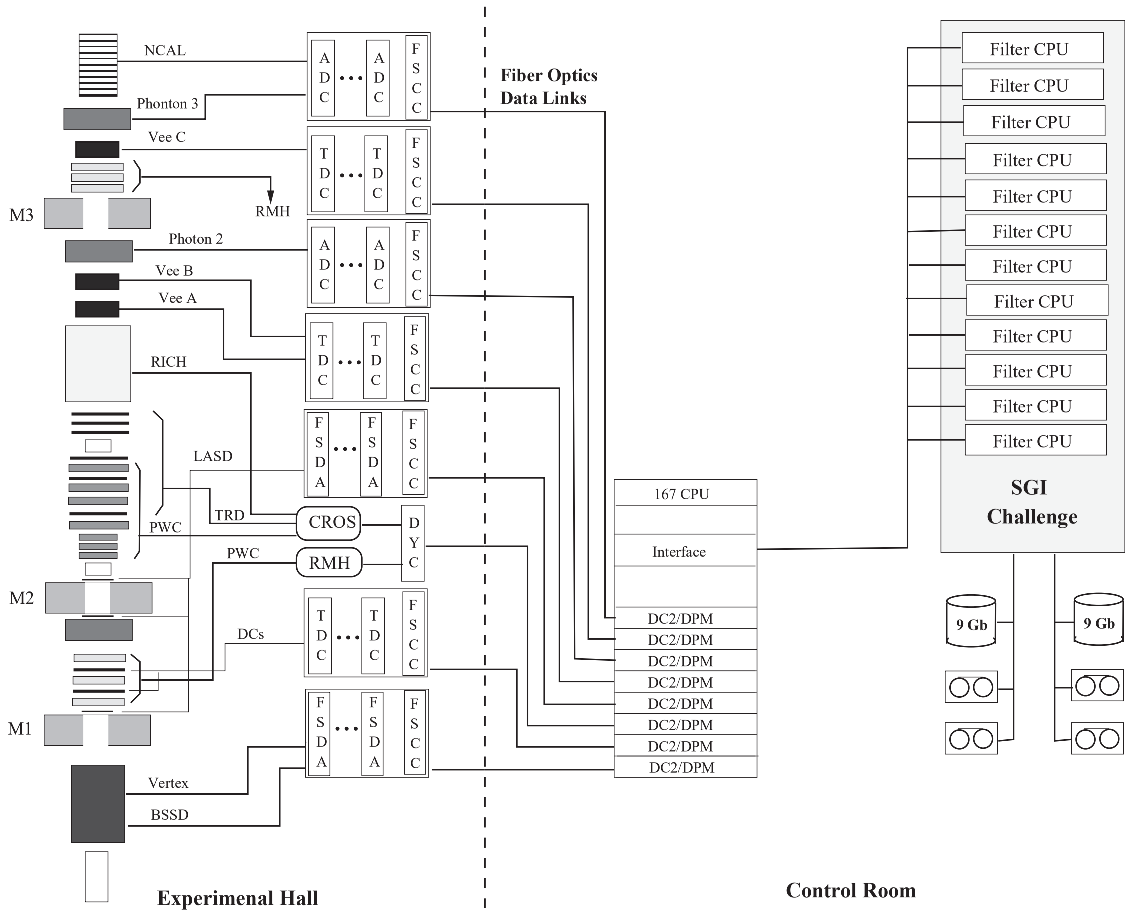

Figure 5.1: E781 DAQ schematic

The center of the DAQ was a Silicon Graphics Indigo (Indy) computer. The running of the experiment was controlled from this computer. Through command scripts and routines the individual detector sections were configured and controlled. The Indy interfaced with two types of controllers in the experimental hall: FASTbus Smart Crate Controllers (FSCC) and Damn-Yankee Controllers (DYC). At the start of each run, configuration files and controls were downloaded to the FSCCs and the DYCs preparing the detector system for data collection. These interfaces also allowed the DAQ to monitor the status of the individual systems. In addition, the trigger was configured according to run conditions (Chapter 4).

Once the run conditions were configured, control of the data collection became automatic based on the trigger. Data from all silicon systems was read via FASTBus SVX Data Accumulators (FSDA). Data for drift chambers was read via FASTbus TDCs, and FASTbus ADCs for the photon detectors and the NCAL. All FASTbus crates were controlled via the FSCCs which were programmable. The M1 and M3 PWCs were read via the RMH system and the M2 PWCs, TRDs and the RICH were read via the Chamber Read-Out System (CROS). The data was then collected via fiber optic links into an SGI Indy computer which fed the SGI challenge for software filtering of the data.

The online filter was design to perform monitoring of the detector components and to act as a first level filter for the data, to enrich the stored data with desired events. At the start of each run, the filter histogrammed detector data which allowed the human controllers to monitor the status of the data collection in near real-time. This feature was very valuable in detecting correctable problems early, before too much data became tainted. Once the data was passed by the filter, it was spooled onto disks for temporary storage as it was written to 8mm Exabyte tapes. The entire collection of SELEX data was stored on these tapes and then transferred in the Fermilab Mass Storage System (FMSS) were it could be retrieved over the network for further processing.

5.2 Off-line Processing

The main software used in the further processing of the data is the SELEX Off-line Analysis Program (SOAP). SOAP consists of five major subsections: unpacker (UNPACK), track finder (TRACK), vertex finder (VERTEX), particle ID (PID) and reconstruction (RECON). Raw data from the FMSS is first passed through UNPACK with formats the data in a consistent fashion for use by the other packages. Once the data is unpacked, each spectrometer is searched for track segments. The track segments are then combined to form tracks. All of the processing is controlled via input files which specify the order, techniques used, required elements and cuts used in the formation of tracks. Once the track segments and tracks have been found, VERTEX is activated to find not only the interaction vertex, but any secondary vertices in the vertex spectrometer. There are two flavors of vertexing which are used. Both flavors have about the same efficiency but they overlap $< 80\%$. So the use of both packages increases the overall reconstruction of vertices. Once the track finding is done and momentums are calculated, the particle ID (PID) package is activated. The results of PID is stored along with the tracks, vertices and other information in tables for use by RECON. RECON is a table driven routine which reconstructs particles, based on the input data, from TRACK, VERTEX and PID. The output of RECON are ftupls which can be converted in ntuples using a program called ftupl_select.

The control on the SOAP process was done through a command file. Within this file, different packages could be turned off and on and different sub-modes of the packages could be specified. In addition, the default set of cuts used for processing could be overridden. A sample control file is shown in Table 5.1.

Control of the track finding methodology was down via a TSEG file. In this file, the starting planes of detectors used for track segment finding and the planes to be involved in the search were specified. In addition, other requirements for the track could be specified. After the segments were found, the tseg file specified the algorithms used and the order of processing in forming tracks from the track segments. The use of control files allowed for the largest versatility with the ease of use in finding the best algorithm needed for finding different types of tracks. A sample tseg file can be seen in Table 5.2.

The reconstruction of events from tracks was also controlled via files. The RECON table (file) specified the form of the reconstruction, requirements on particle ID for the reconstruction and constraints on the reconstruction. A Sample RECON table is shown in Table 5.3.

5.3 Simulation

Several types of simulations are available in SELEX. For this analysis, two types of simulators were used, EXP and embedding. EXP is a geometric simulator which is database driven. During the analysis, I modified the program to use real data for the beam profile, to simulate polarization and to generate both ftuples and embed files for futher analysis. EXP uses a database of detector elements combined with a control file to simulate events. The type of event required (i.e. $\Sigma^- \rightarrow \Lambda^0 \rightarrow p + \pi^-$) is input along with constraints via a control file. This file allows the specification of where decays can occur, which detectors must 'see' the particles and control parameters which define the production characteristics of the particles. In this fashion, the phase-space distribution of the daughter particles can be controlled along with the fiducial volume. A sample control file is shown in Table 5.4 and a sample apparatus file is shown in Table 5.5.

Embedding allows files with simulated events to be embedded over the raw data for processing by SOAP. The data can be embedded as perfect events or smeared and it can either be embedded over real data or instead of

Table 5.1: SOAP sample control file

```
! PASS11
 noexec   filter
 set  on  driver    wrt_savebk save_all prod
 execute  unpack
 set  on  unpack    adc cros rmh svx ! hist
 execute  tracking
 set  on  tracking  segment link fit0 silmatch silm3d guided fit hist
 set  on  tracking  vx_radial m1_guide vx_lasd tr_seg2 ! tr_subset tr_user
 set  on  tracking  m1_share            ! m1pwc s-y hit share
 set  cut tracking  lasd_wid       2.   ! inflate LASD res by factor 2
 set  cut tracking  max_bmsi     250.
 set  cut tracking  max_vxsi    1000.
 set  cut tracking  max_pwc      260.
 set  cut tracking  max_svx     1000.
 set  cut tracking  segment         0   ! all spectrometers on in track_segment
 set  cut tracking  ptm1       0.7371   ! use fixed spectrometer pt_kicks
 set  cut tracking  ptm2       0.8285   ! use fixed spectrometer pt_kicks
 set  cut tracking  trajectory parabolic ! parabolic trajectory as a default
 prog     tracking  pass11.tseg

 ocs  class main anal
 ocs  sets out ncal_                     ! vdc_
 exec     photon
 set  on  photon    full m1_pht m2_pht m3_pht
 set  cut photon    min_count  5.
 set  cut photon    min_energy 2.
 exec     partid
 set  on  partid rich btr etr etr_track  ! etr_hist
 execute  user
 set  on  user   hist          ! pass11_11_v1
 set  cut user   report        1000
 exec     vertex
 set  on  vertex vtx2   err2 secint   prim  sec
 set  cut vertex prong            5
 set  cut vertex vtxd           4.0
 exec     recon
 set  on  recon  hist   ftuple strip ! ntuple
 set  cut recon  tgt_rec       0.05
 set  cut recon  pscale        1.0000 ! pass11_11_v1
 set  cut recon  cand_csec     5.0
 set  cut recon  cand_cpri     5.0

 disk in  reset
 in   disk_files

 ana    0
 exit
```

Table 5.2: SOAP sample TSEG file

```
spec: bm vx m1 m2 m3                 ! all.tseg - general purpose tracking
comb: bm_comb1
      planelist:  bm_ssd_ 1x1y1u2x2y3x3y3u
      planeinit:  bm_ssd_1y bm_ssd_3y bm_ssd_1x bm_ssd_3u
!     cut names   xl   xh   txl   txh   yl  yh   tyl   tyh  xs  ytgt  chi2  npl
      cuts:       0.,  0.,-.0012,.0012, 0., 0.,-.0012,.0012,0.0, 0.2,   4.0,  7
*end

comb: bm_comb2
      planeinit:  bm_ssd_1y bm_ssd_2y bm_ssd_1u bm_ssd_3x
!     cut names   xl   xh   txl   txh   yl  yh   tyl   tyh  xs  ytgt  chi2  npl
      cuts:       0.,  0.,-.0015,.0015, 0., 0.,-.0015,.0015, 0.0, 0.2,  9.0,  7
*end

comb: vx_comb1
      planelist:  vx_ssd_ 1x1y1u1v2x2y2u2v
      planelist:  vx_msd_ 1x1y1u1v2x2y2u2v3x3u3v4x
      planeinit:  vx_ssd_1u vx_ssd_1v vx_msd_2x vx_msd_2y
!     cut names   xl   xh   txl   txh   yl  yh   tyl   tyh   xs  ytgt chi2  npl
      cuts:       0.,  0.,-.025, .025,  0., 0.,-.025, .025,    ,    ,  5.0, 12
*end

comb: vx_comb2
      planeinit:  vx_ssd_2x vx_ssd_2y vx_msd_3u vx_msd_3v
!     cut names   xl   xh   txl   txh   yl  yh   tyl   tyh   xs  ytgt  chi2 npl
      cuts:       0.,  0.,-.100, .100,  0., 0.,-.100, .100,    ,     , 20.0, 10
*end

link   prog bmdown
link   copy bm                       ! convert beam tseg into track
link   prog m2down
link   copy m2                       ! copy M2 segments

tracking  findcl     all             ! clusterize all planes
!tracking  fbk_guide                  ! find tracks in filter block
tracking  tr_seg2    m2              ! alternate M2 segment finder
tracking  segment    bmm2            ! find segments in all spects but vx
tracking  link       bmdown          ! prepare bm Tsegs for silmatch
tracking  guided     bm>vx_comb1     ! find old beam tracks in vx
tracking  fit0       bm              ! momenta for beam tracks
tracking  fit                        ! momentum fit all fittable tracks
```

Table 5.3: SOAP sample RECON table

```
#recdf      0     0 fill anal v01.20 04-Mar-1998 16:32 psc ! pass12 recon list
! pass11 production - add new charmed baryon modes + excited states + x1 recons
  id  name       from pr q  pid   ls_min ls_max mass_min mass_max   out !   frac
!                                                                         n  [%]
! Strange states
   1  kshort      v2  2  0  i-i+       5.  800.   0.470  0.530  $100008 !01 1.41
   2  lambda      v2  2  0  p+i-       5.  800.   1.090  1.140  $200008 !02 0.33
   3  alambda     v2  2  0  p-i+       5.  800.   1.090  1.140  $200008 !03 0.07
   4  phi         c   2  0  k+k1-      0.    0.   0.995  1.045  $400000 !04 8.21
   4  phi         c   2  0  k2+k-      0.    0.   0.995  1.045  $400000 !05 4.36
   5  psi_ee      c   2  0  e+e-       0.    0.   0.200  5.000  $000008 !06 0.26
  10  k0          v2  2  0  i+i-      20.  800.   0.470  0.530  $000000 !07 0.78
  12  l0          v2  2  0  p+i-      20.  800.   1.090  1.140  $000000 !08 0.19
  14  phi_det     v2  2  0  k+k1-      5.  800.   0.995  1.045  $000008 !09 0.09
  14  phi_det     v2  2  0  k2+k-      5.  800.   0.995  1.045  $000008 !10 0.04
  31  kshort_1    x1  2  0  i-i+       5.  800.   0.470  0.530  $100008 !11 1.69
  32  lambda_1    x1  2  0  p+i-       5.  800.   1.090  1.140  $200008 !12 0.46
  33  alambda_1   x1  2  0  p-i+       5.  800.   1.090  1.140  $200008 !13 0.12
  44  phi_det_1   x1  2  0  k+k1-      5.  800.   0.995  1.045  $000008 !14 0.27
  44  phi_det_1   x1  2  0  k2+k-      5.  800.   0.995  1.045  $000008 !15 0.12
!
! Partial states
  52  i2i         v2  3 +1  i-i+i+     0.  800.   0.400  1.300  $002000 !16 17.6
  61  ki          v2  2  0  k-i+       5.  800.   0.600  1.700  $002002 !17 0.91
  62  k-2i        v2  3 +1  k-i+i+     5.  800.   0.750  1.500  $002002 !18 0.20
  63  k3i         v2  4  0  k-i-i+i+   0.  800.   0.900  1.700  $002000 !19 1.82
  64  k+2i        v2  3 -1  k+i-i-     5.  800.   0.750  1.500  $002002 !20 0.35
  71  kki         v2  3 -1  k-k-i+     5.  800.   1.100  1.600  $002002 !21 0.01
  72  kk2i        v2  4  0  k-k-i+i+   0.  800.   1.200  1.700  $002000 !22 0.02
  86  pii         v2  3 +1  p+i+i-     0.  800.   1.200  1.700  $002000 !23 3.26
!
! D0
 100  d0_kpi      v2  2  0  k-i+       0.  800.   1.664  2.064  $000041 !24 0.19
 101  d0b_kpi     v2  2  0  k+i-       0.  800.   1.664  2.064  $000041 !25 0.28
 102  d0_k3pi     v2  4  0  k-i-i+i+   3.  800.   1.764  1.964  $000041 !26 0.44
 103  d0b_k3pi    v2  4  0  k+i+i-i-   3.  800.   1.764  1.964  $000041 !27 0.58
 104  d0_kk       v2  2  0  k-k+       0.  800.   1.664  2.064  $000041 !28 0.08
 130  d0_kpi_1    x1  2  0  k-i+       5.  800.   1.664  2.064  $000041 !29 0.12
 131  d0b_kpi_1   x1  2  0  k+i-       5.  800.   1.664  2.064  $000041 !30 0.15
 132  d0_k3pi_1   x1  4  0  k-i-i+i+   3.  800.   1.764  1.964  $000041 !31 0.21
 133  d0b_k3pi_1  x1  4  0  k+i+i-i-   3.  800.   1.764  1.964  $000041 !32 0.25
 190  d0_ke       v2  2  0  k-e+       0.  800.   0.500  1.900  $000810 !33 0.11
 192  d0_k-e-     v2  2 -2  k-e-       0.  800.   0.500  1.900  $000810 !34 0.08
```

Table 5.4: EXP sample control file input

```
COND      CHAMB     WA    WB

COND      RICH      VX2  SD2  RCH

COND      TARG      VX2

COND      MMMO      VX2  SD2

PARTICLE  L0        1.11560    0.       0.789
PARTICLE  KS0       0.49767    0.       0.0100
PARTICLE  D0        1.8645     0.       0.01244
PARTICLE  D+        1.8693    +1.       0.0317
PARTICLE  RHO0      0.770      0.       0.00000001
CUT       DV        S   L0    LAB        -5.0      -1.0
CUT       DV2       S   L0    LAB       -13.0       0.0
EVENT     200000
DECAYVOL  0.0       0.1
SCAT      SIG- -->  L0

          2.200     2.300     0.00      1.00
MODE      L0    --> P     +   PI-
                    TARG      TARG

DEBUG     1
END
```

Table 5.5: EXP sample apparatus file input

```
TITLE     E781 TRACK FINDING SIMULATION
C
C         Mostly empty file for initial testing
C
EVENT     100
HYPE      800.0     600.0     0.0       0.0
          0.0       0.0       .000000   .000000
          0.0       0.1000    0.1000    0.0
PWC       TAR
          0.0       5.0       0.0
          0.0       5.0       0.0
          0.0       0.0
DECAYVOL  0.0       1000.
PWC       VX2
          0.0       5.0       0.0
          0.0       5.0       0.0
          15.4      0.0       0.0000    0.
PWC       VX5
          0.0       12.8      0.0
          0.0       9.0       0.0
          46.97     0.0       0.000     0.
MAGNET    M1
          0.0       60.96     0.0
          0.0       50.80     0.0
          99.5      182.88    -0.7332
PWC       SD2
          0.0       5.12      0.0
          0.0       5.12      0.0
          285.      0.0       0.0000    0.
MAGNET    M2
          0.0       60.96     0.0
          0.0       25.40     0.0
          653.6     182.88    -0.8421
PWC       HOD1
          15.0      30.0      0.0
          0.0       30.0      0.0
          885.4     0.0       0.0000    0.
```

real data for processing. This tool is very useful in verification of the analysis techniques used and cut specification. Control of the embedding is done via the SOAP control file. A sample embed file for the decay $\Lambda^0 \rightarrow p + \pi^-$ is shown in Table 5.6. In this file, the first three parameters are the position of the particle, the second three are the direction cosines, followed the by particle momentum and then the mass. the first line in the file describes the file contents in terms understood by the embedding software.

5.4 Data Analysis

The majority of the data analysis is performed using tools developed at CERN. The main tool used is the Physics Analysis Workstation (PAW). PAW is part of the CERN library and is quite robust. In general, PAW works with ntuples and histograms. It's processing is extensible by calling user written FORTRAN routines which perform user specific actions. Most other actions can be accomplished through the use of KUMAC (script) files which control the processing of the ntuples/histograms. A sample KUMAC file is shown in Table 5.7. The use of PAW macros and PAW extensions allowed the ntupls and histograms to be completely analyzed. Other features of the CERN library were used in both EXP and SOAP.

Table 5.6: Example embed file for $\Lambda \rightarrow p + \pi^-$

```
3 0 +1 -1 $6 $10000 $10000 ;exp lambda decay
  0.00    0.00    0.08   0.00203   0.00093   1.00000  144.31  1.116
  0.01    0.01    7.12   0.00274   0.00041   1.00000  111.93  0.938
  0.01    0.01    7.12  -0.00152   0.00353   0.99999   22.58  0.140
  0.00    0.00    0.04   0.02073  -0.02381   0.99950   42.60  1.116
  0.03   -0.03    1.30   0.02255  -0.02621   0.99940   33.16  0.938
  0.03   -0.03    1.30   0.01149  -0.01167   0.99987    6.54  0.140
  0.00    0.00    0.05  -0.02809   0.00444   0.99960    8.64  1.116
 -0.05    0.01    1.89  -0.04276   0.00526   0.99907    6.83  0.938
 -0.05    0.01    1.89   0.05390  -0.00021   0.99855    1.22  0.140
  0.00    0.00    0.01  -0.00390  -0.00373   0.99999  121.50  1.116
 -0.01   -0.01    1.65  -0.00422  -0.00437   0.99998   87.84  0.938
 -0.01   -0.01    1.65  -0.00276  -0.00153   0.99999   25.41  0.140
  0.00    0.00    0.06  -0.00288  -0.00703   0.99997  145.94  1.116
  0.00    0.00    0.64  -0.00333  -0.00702   0.99997  104.13  0.938
  0.00    0.00    0.64  -0.00142  -0.00707   0.99997   31.80  0.140
  0.00    0.00    0.04  -0.00711  -0.00074   0.99997   49.84  1.116
 -0.01    0.00    2.05  -0.00655  -0.00315   0.99997   40.02  0.938
 -0.01    0.00    2.05  -0.01055   0.01426   0.99984    6.43  0.140
  0.00    0.00    0.06  -0.07567   0.12826   0.98885    5.79  1.116
 -0.04    0.07    0.56  -0.08512   0.13575   0.98708    4.13  0.938
 -0.04    0.07    0.56  -0.04461   0.10359   0.99362    1.26  0.140
  0.00    0.00    0.02   0.00068   0.00276   1.00000  119.62  1.116
  0.01    0.04   13.37   0.00095   0.00358   0.99999   99.49  0.938
  0.01    0.04   13.37  -0.00156  -0.00406   0.99999   11.93  0.140
  0.00    0.00    0.03   0.00143   0.00104   1.00000   84.84  1.116
  0.02    0.01   14.16   0.00032   0.00101   1.00000   61.68  0.938
  0.02    0.01   14.16   0.00541   0.00113   0.99998   17.35  0.140
  0.00    0.00    0.09  -0.08727   0.03557   0.99555    5.79  1.116
 -0.56    0.23    6.45  -0.08117   0.05604   0.99512    4.39  0.938
 -0.56    0.23    6.45  -0.11314  -0.05307   0.99216    1.02  0.140
  0.00    0.00    0.03  -0.01673  -0.00110   0.99986   12.46  1.116
```

Table 5.7: Sample KUMAC file used in the polarization analysis

```
nt/chain pass pd001.ntu pe001.ntu
nt/chain pass pf002.ntu pg001.ntu ph001.ntu
nt/chain pass px001.ntu py001.ntu pz002.ntu

cd //pass

opt stat
opt ndat
title 'Polarization of [L]^0!inclusively produced by [S]^-!'

nt/cut $1 btk_pid.lt.10.and.abs(tk3_py).gt.0.025
nt/cut $2 $1.and.abs(mass-1.116).lt.0.005
nt/cut $3 tk1_pid.lt.1000
nt/cut $4 $2.and.$3.and.mod(-tk2_type,1000.)>8

for/file 66 final_polar3.ps
meta 66 -111

opt stat
set stat 110
opt fit
set fit 111

exec final_cuts.kumac
exec final_polar2.kumac
exec final_polar3.kumac
exec final_polar4.kumac
exec final_polar5.kumac
close 66
exit
```

CHAPTER 6.

DATA ANALYSIS

The traditional method used for analyzing polarization required measuring the acceptance of the apparatus by way of a full scale monte carlo. Once the acceptance of the apparatus is known, the acceptance can be removed from the data distribution and the polarization measured. In order to reduce the final error in the measurement, the monte carlo must be contain far more events than the real data. This method is only as good as the simulation of the apparatus. A more modern technique, and the one used in this analysis, uses algorithms which cancels the acceptance function from the polarization distribution.

$$\frac{dN}{d\Omega} = \frac{1}{4\pi}(1 + \alpha P_\Lambda \cdot \hat{k}_{proton}) \tag{6.1}$$

The convention used in this analysis is the polarization axis is defined as:

$$\hat{P} = \hat{k}_{\Sigma^-} \times \hat{k}_\Lambda \tag{6.2}$$

For this analysis, it is consider to be the $y-axis(\hat{y}_{cm})$ in the CM frame of the Λ. In addition, the $z-axis(\hat{z}_{cm})$ is the Λ line-of-flight and the $x-axis(\hat{x}_{cm})$ completes the orthogonal triad (see Fig. 6.1). This figure also shows the definition of the angle between the polarization vector and the proton line-of-flight in the cm frame.

The laboratory coordinates are as follows. The $z-axis(\hat{z}_{lab})$ is the along the average beam line-of-flight. The $y-axis(\hat{y}_{lab})$ is vertical and the

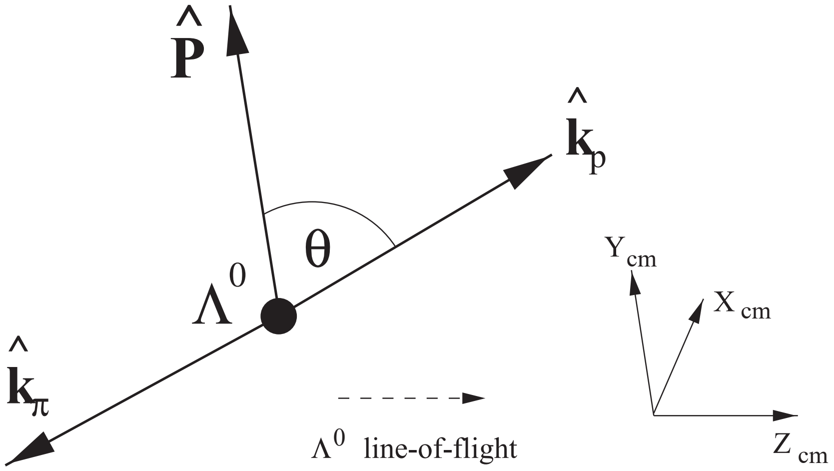

Figure 6.1: Λ^0 CM frame definition.

$x - axis(\hat{x}_{lab})$ completes the orthogonal triad. The laboratory frame coordinates were defined based on the position of two planes of Beam silicon strip detectors. All other detectors were aligned to the position of these detectors at the time of each alignment run. Fig. 6.2 shows a sample event in the lab frame. Note that the decay plane can be at any angle to the production plane but the momentum sum of the daughter particles must combine to form the parent Λ's.

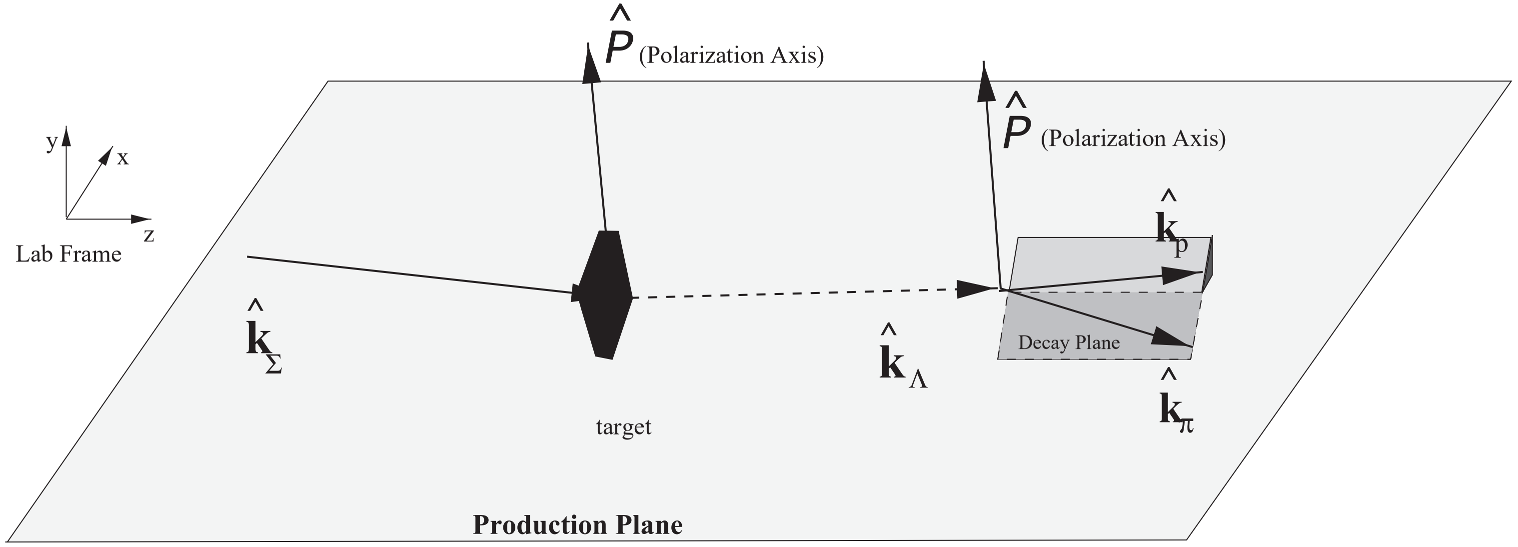

Figure 6.2: Sample event in the Laboratory frame

Given the acceptance of the apparatus and the angular spread in the Σ^- beam, the polarization axis will lie closely to the (x_{lab}, y_{lab}) plane. However, it may have any azimuthal angle with respect to the x-axis. Also, the angle between the daughter proton and the polarization vector may have any value (see Fig. 6.1). Therefore, the data must be grouped by azimuthal sectors and bins in $\cos\theta$ in order for the apparatus acceptance function within a sector - $\cos\theta$ bin combination to be smooth and relatively flat. This analysis of the polarization relied on the ability of the bias canceling algorithms used to successfully eliminate biases due to the non-uniformity of the apparatus. Fig. 6.3 shows the azimuthal bins in the lab coordinates. The data was binned on the projection of the polarization vector in the laboratory $(x_{lab} y_{lab})$ plane.

6.1 Bias Cancellation Methods

Two bias cancellation methods were used throughout this analysis. Multiple means were used as cross checks to ensure that the algorithms implemented were correctly written and successful in their ability to cancel biases. A complete description of the bias canceling algorithms and the derivation of the errors inherent in each, is given in Appendix A. The general idea of the algorithms is to compare regions of the detector where the acceptance is the same for both 'up' and 'down' events. In this manner, any bias inherent in the apparatus is eliminated to good precision if the apparatus function is smooth and the data is binned such that changes within a given set of data for the acceptance is small. Fig. 6.4 is a comparison of two such regions. In this figure it is evident, that if the apparatus is up-down symmetric, then the daughter particles from decays whose polarization axis is 'up' and decays whose polarization is 'down' will have the same apparatus acceptance

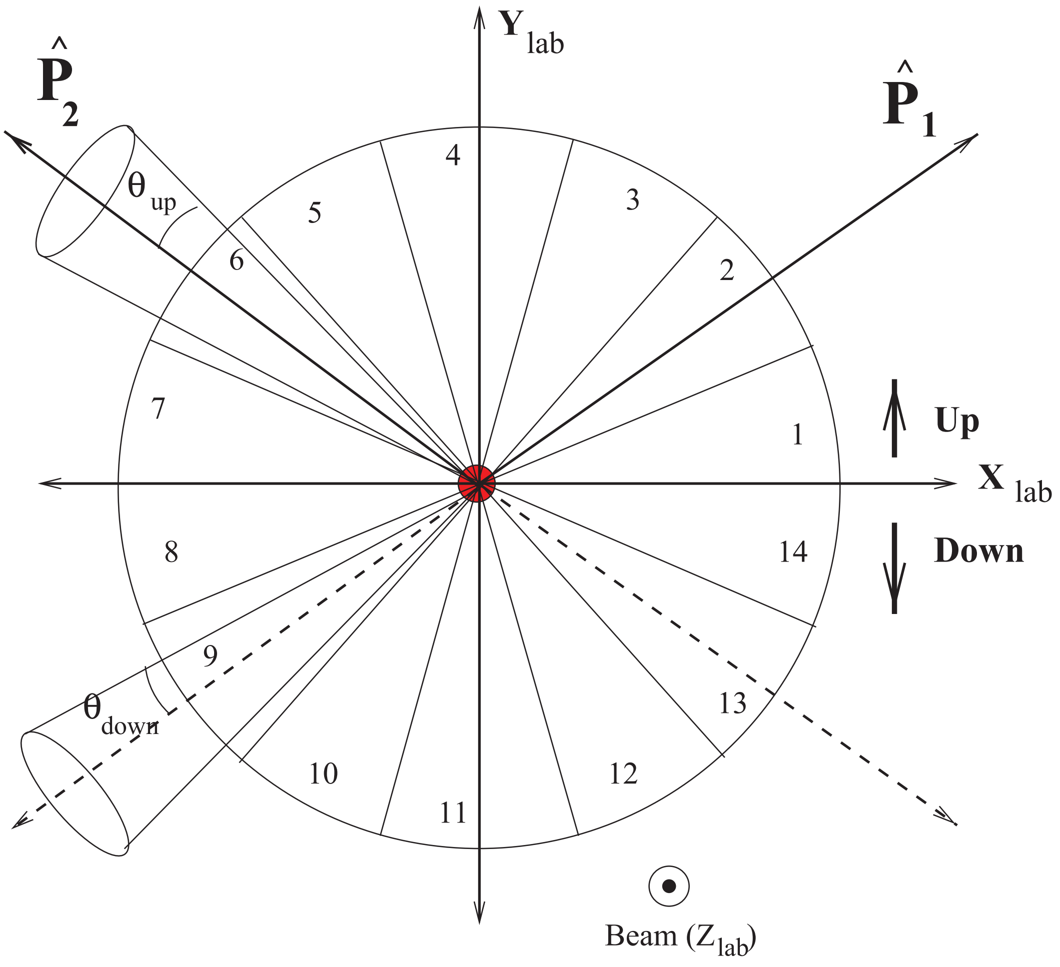

Figure 6.3: Division of data into azimuthal bins

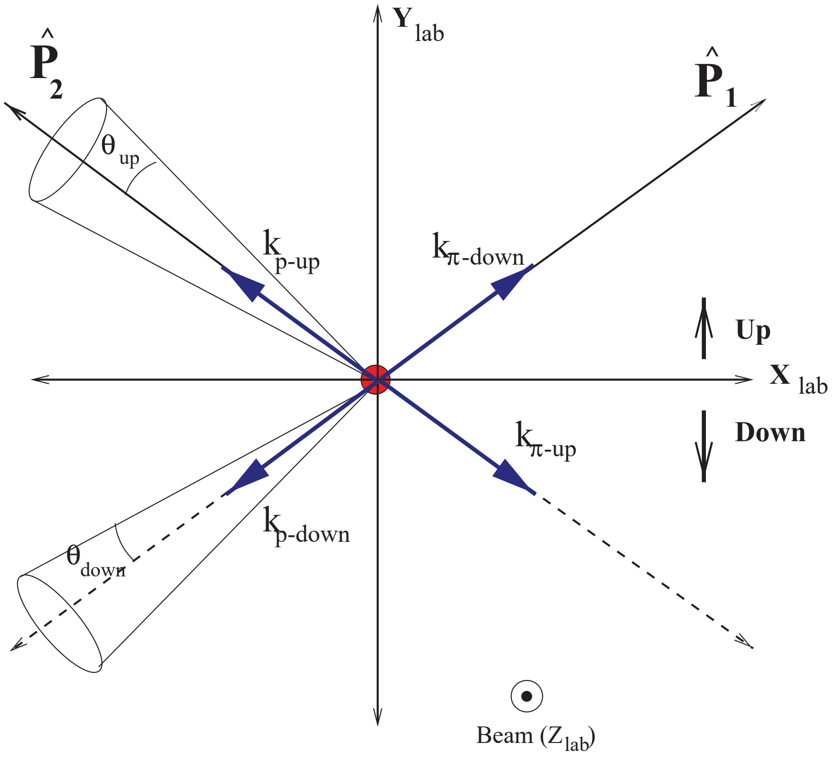

Figure 6.4: Comparison of apparatus acceptance regions

function.

The two methods used for this analysis are the Geometric Mean and the Arithmetic Mean methods. The Geometric Mean method used the following ratio:

$$\epsilon_i = \frac{\sqrt{U(z_i) \times D(-z_i)} - \sqrt{U(-z_i) \times D(z_i)}}{\sqrt{U(z_i) \times D(-z_i)} + \sqrt{U(-z_i) \times D(z_i)}} = \alpha P z_i \tag{6.3}$$

where $z_i = \cos\theta_i$ is the angle between the normal to the production plane and the proton momentum in the Λ CM frame (see Fig 6.1).

The Arithmetic Mean method used the following ratio:

$$\epsilon = \frac{U(\cos\theta) + D(-\cos\theta) - U(-\cos\theta) - D(\cos\theta)}{U(\cos\theta) + D(-\cos\theta) + U(-\cos\theta) + D(\cos\theta)} = \alpha P \cos\theta \qquad (6.4)$$

Both methods were used throughout this analysis and served as one of the cross-checks to the results. Since both methods are to a large part independent they served help validate each other. These methods were written as *.kumac* files which were used in PAW to analyze the data.

The flow of the process used to analyze the data is show in Fig. 6.5. In SELEX, the raw data gathered for the experiment is stored on $8mm$ tapes and placed into the Fermilab Mass Storage System (FMSS) for later processing. The data was then processed by the SELEX Off-line Analysis Program (SOAP). The data used for this analysis was the result of the first full pass-though of the data (PASS1). PASS2 is planned to occur in the Fall of 1999. The output of SOAP were files in the form of ftuples (file ntuples). The form of the output allowed additional processing of the data as it was converted into ntupl form, which is the main form of data used by PAW. During this conversion to ntuples is when the direction cosines of the proton in the Λ CM frame were calculated, in addition to other useful parameters for the verification of the analysis.

The various methods used to validate the algorithms is discussed below. First, is a discussion on the selection of the data, and it's characteristics.

6.2 Data Selection

The output of PASS1 contained $1,441,664$ events with candidates for Λ^0 decays. The algorithm used by RECON required the $\Lambda' s$ to decay by the first vertex SSD station. This meant the decay volume was from the first charm target to 15.6cm downstream of the last charm target. Although this is a

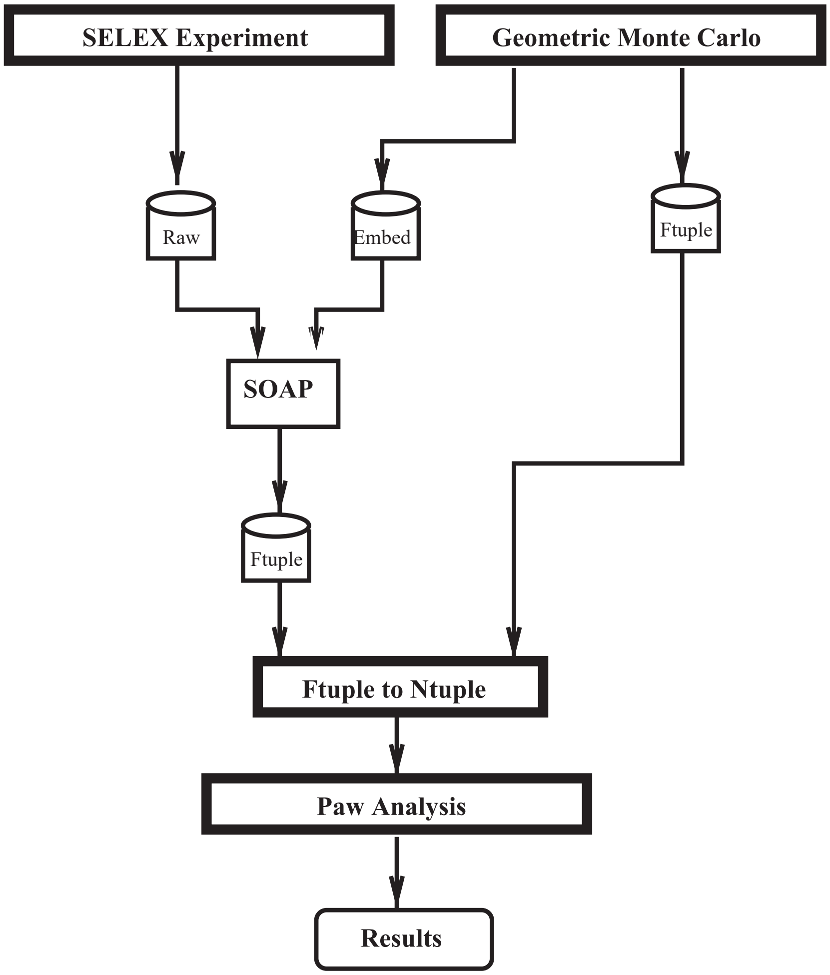

Figure 6.5: Process flow for the analysis of the data

Table 6.1: Sequential selection cuts and their effects

Cut	Events	% reduction
No cut	1,441,664	0%
abs(mass-1.116).lt.0.005	1,037,537	28.0%
btk_pid.lt.10	1,003,609	3.3%
mod(-tk2_type,1000.)>8	401,880	60.0%
tk1_pid.lt.1000	372,311	7.4%
abs(tk3_py).gt.0.025	364,859	2.0%

small volume, the large number of events captured during the run accounted for the 1.4M candidates. These candidate events were reduced considerably by the data selection cuts. Table 6.2 shows the reduction in data due to each sequential cut.

The data selection cuts were 1) mass window around the mass of the Λ^0, 2) requiring that the BTRD identify the beam particle as a Σ^-, 3) requiring that the pion be observed in the M2 spectrometer and consequently the RICH, 4) requiring that the RICH positively identify the proton, and 5) removing events were the resolution of the spectrometer makes the distinction between 'up' events and 'down' events unreliable. This is a cut on the cosine of theta.

The mass cut and the requirement that the pion be in the M2 spectrometer caused the largest reduction in the data. The final mass plot of the data used in the analysis is shown in Fig. 6.6 (Breit-Wigner fit), and the mass plot after each of the cuts is shown in Fig. 6.7.

The most interesting data selection cut is the requirement that the pion appear in M2. This requirement is an effective cut on the momentum of the

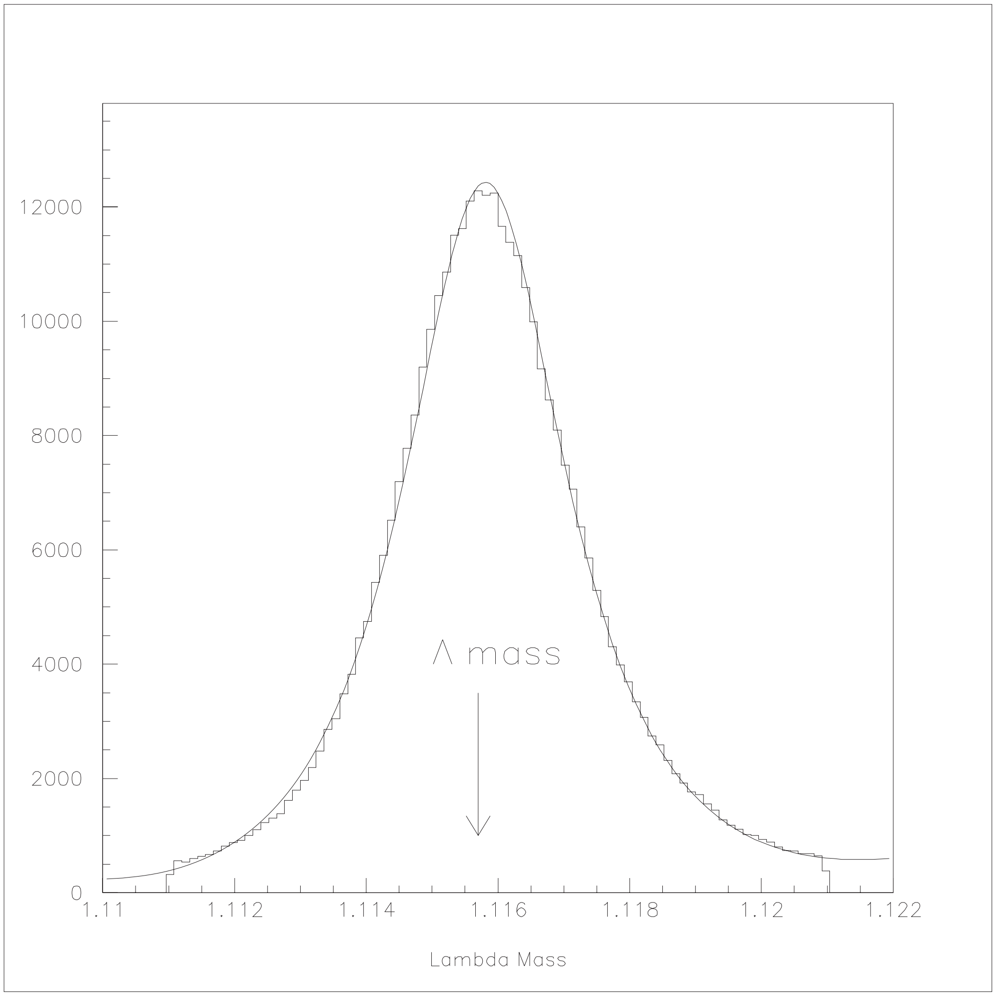

Figure 6.6: Λ^0 mass plot after all data selection cuts

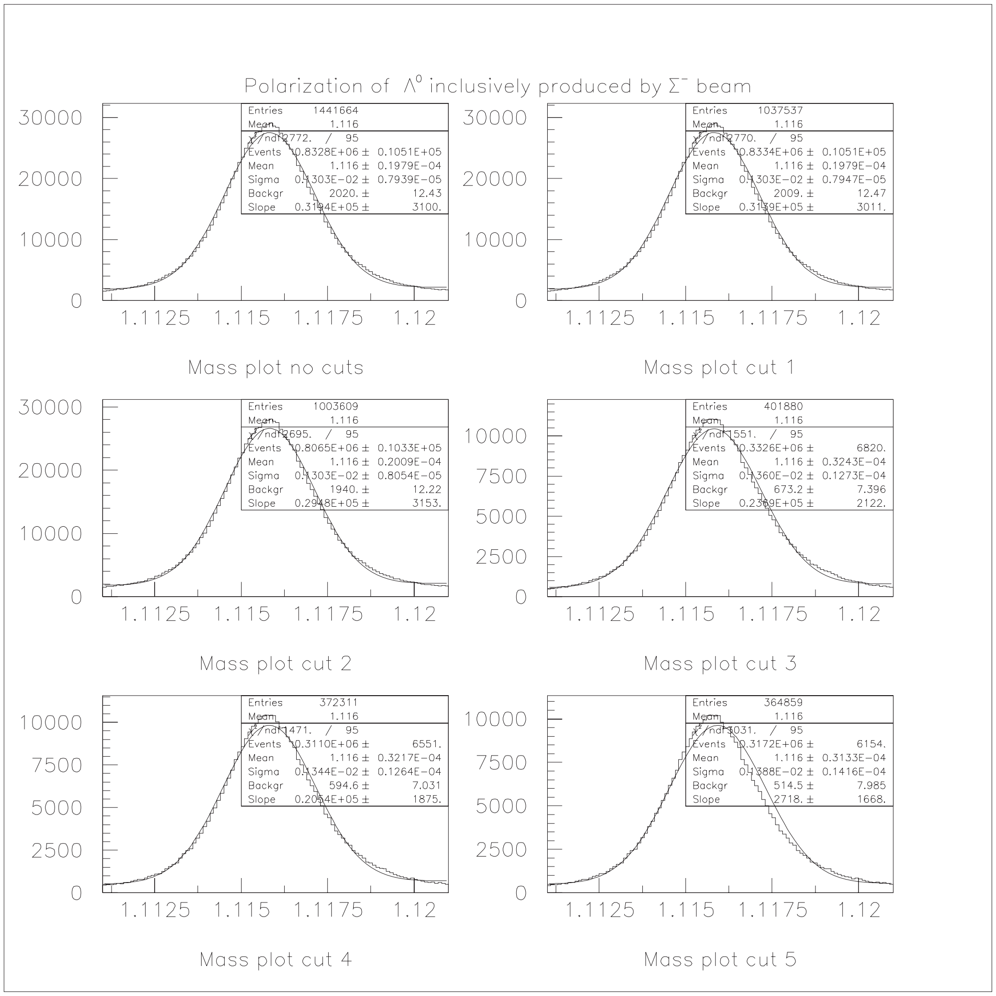

Figure 6.7: Λ^0 mass plot after each data selection cut

pion since the pion is the lowest momentum particle of the decay. The M2 spectrometer has a lower limit on momentum of 15 GeV/c due to the field strengths of the M1 and M2 magnets. Therefore, this cut effectively removes events with low x_f. Fig. 6.8 shows the x_f distribution before and after this cut. The y-axis is the log of the number of events, giving a better picture of the effect at high x_f.

Fig. 6.9 shows the efficiency of this cut for both the x_f distribution and the p_t distribution. From the x_f efficiency it can be seen that this cut is 80% efficient at $x_f = 0.3$ and rises to $\approx 95\%$ for most of the region. This set the lower limit for this analysis in x_f to be 0.3. The effect on the p_t distribution for this cut was fairly uniform. It started around 40% for the bulk of the data while slightly favoring data at the higher p_t range. For the SELEX detector, this cut put all of the analyzed data in a well understood region. The acceptance of the M2 spectrometer is well understood and selects the high x_f events which the experiment was designed for. The usefulness of this cut will be shown below, but it's use reduced the systematic errors associated with the data to be small compared to the statistical errors.

6.3 Data Profiles

The profiles for the data used in this analysis are shown in the following figures. Fig. 6.10 shows the Σ^- profile with a mean momentum of $610 GeV/c$. Fig. 6.11 shows the Λ^0 profile. Fig. 6.12 show the proton profile, and Fig. 6.13 show the pion profile.

6.4 Algorithm Validation

In this type of analysis, a lot of the usual algorithm checks are not apparent. The traditional method of measuring the acceptance of the apparatus

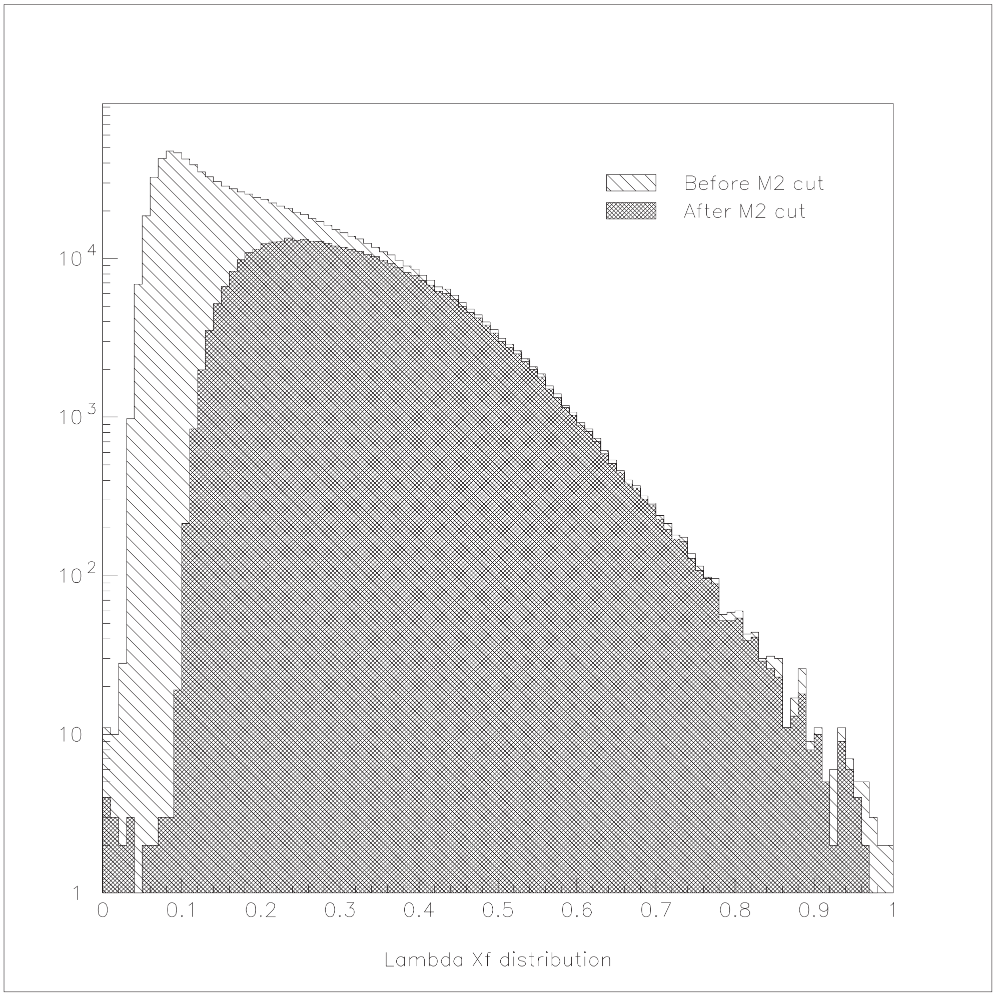

Figure 6.8: X_f distribution before and after the M2 required cut

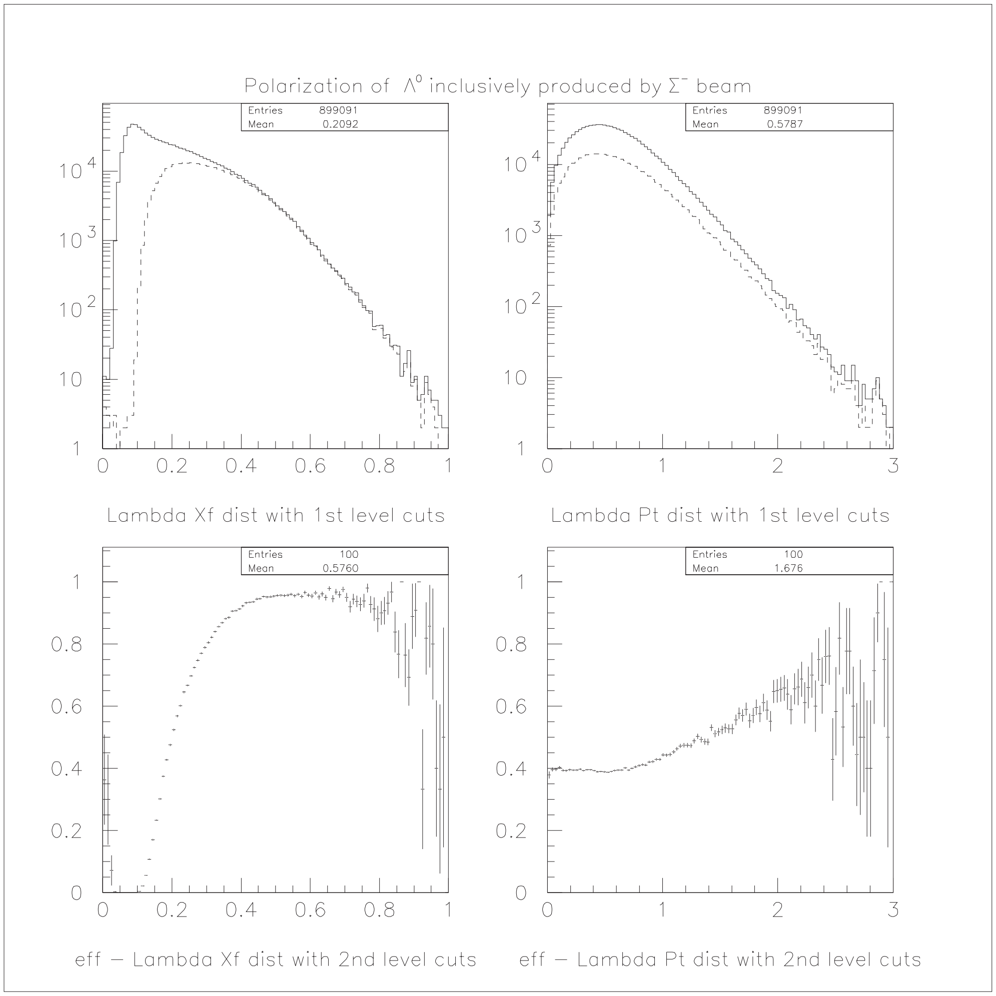

Figure 6.9: X_f and P_t after the M2 required cut showing the cut efficiencies

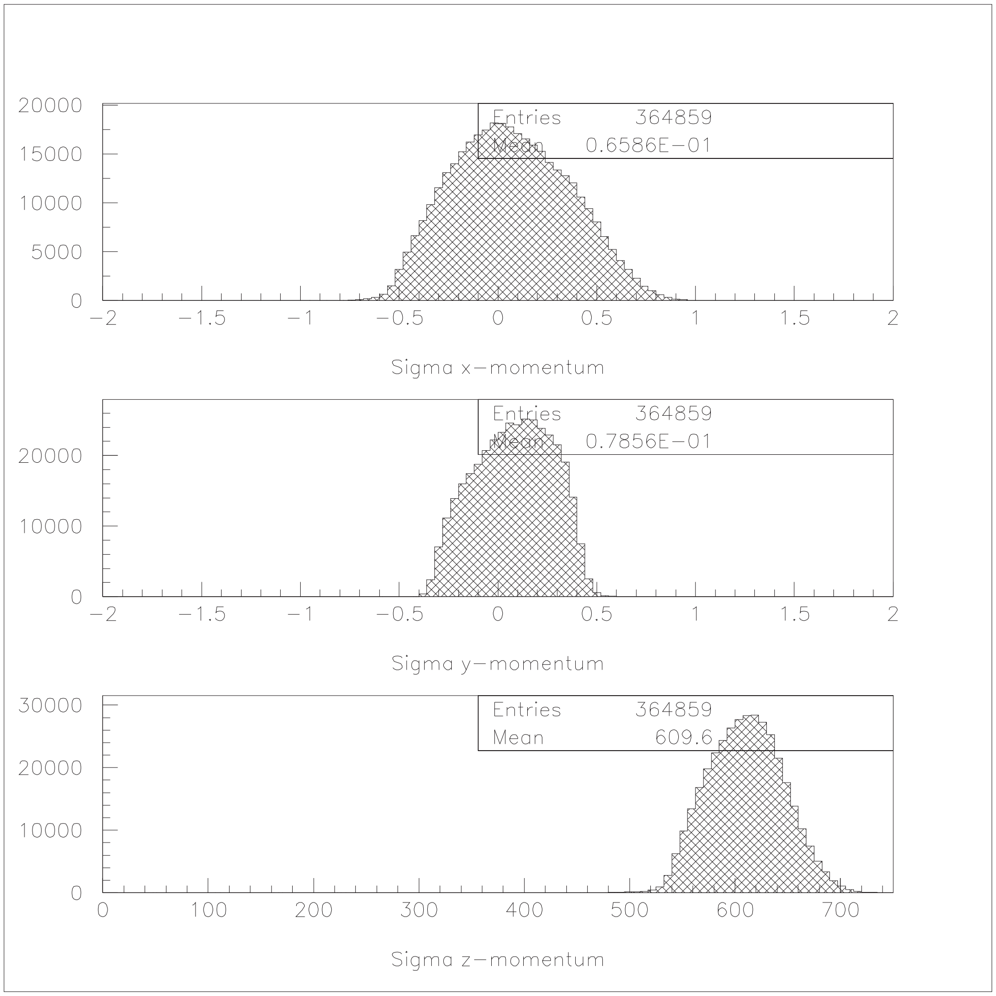

Figure 6.10: Σ^- momentum profiles after all data selection cuts

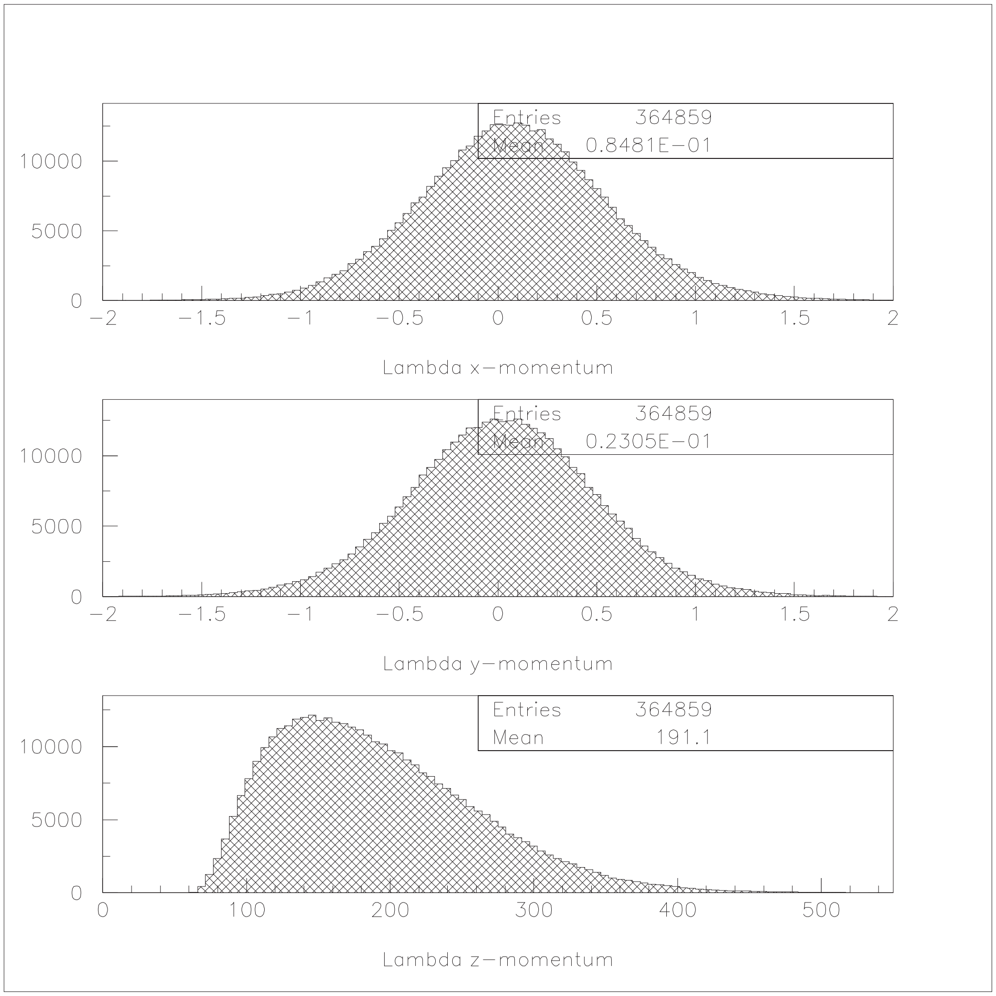

Figure 6.11: Λ^0 momentum profiles after all data selection cuts

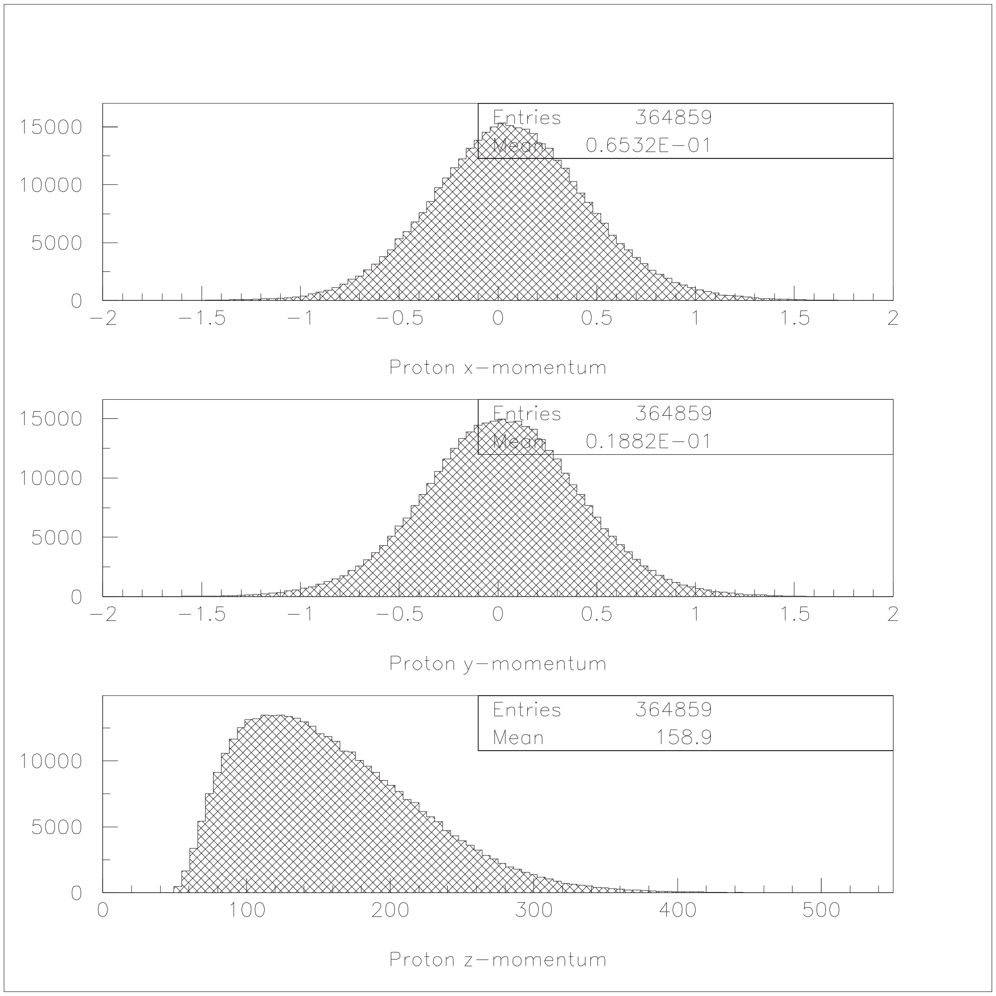

Figure 6.12: Proton momentum profiles after all data selection cuts

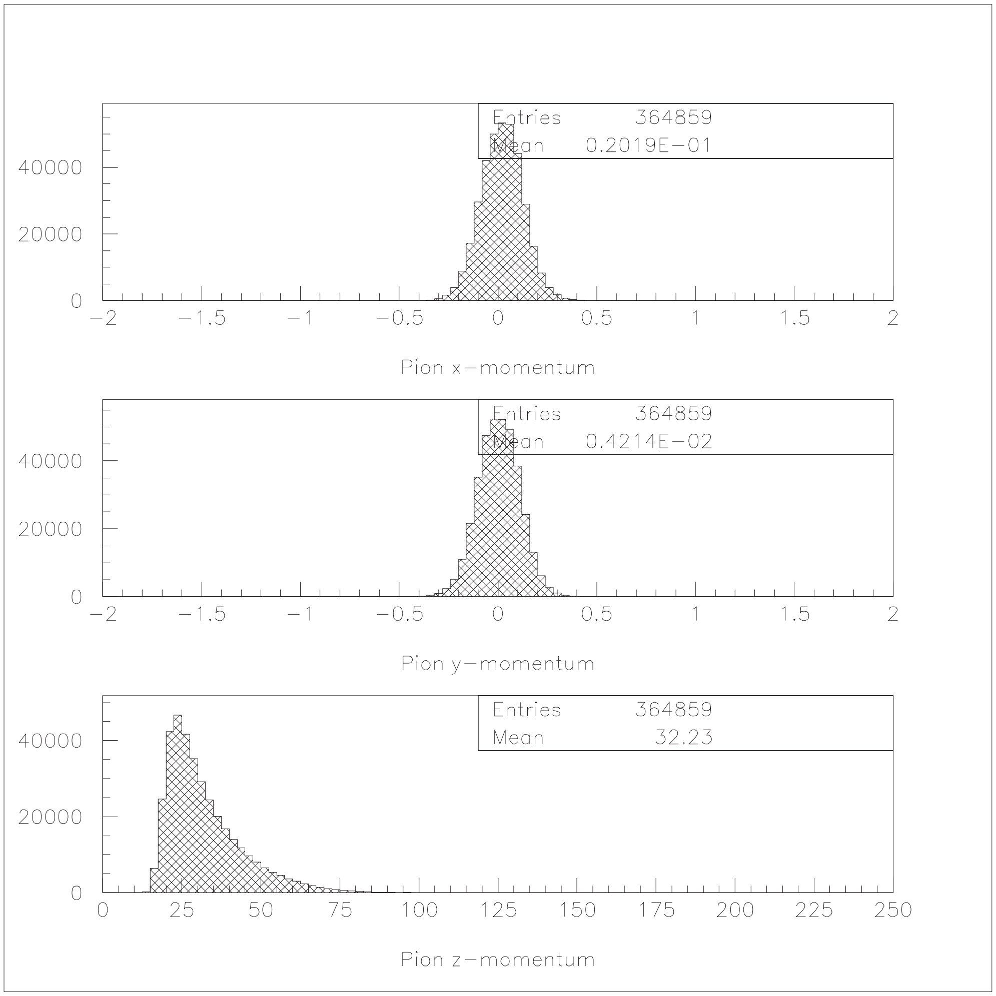

Figure 6.13: Pion momentum profiles after all data selection cuts

and the dividing the data by the acceptance allows for many visual checks which are used to validate the results. This method works well with small data sets but the need for a full monte carlo to the detector at a level of 10 - 20 times the data used in the analysis makes this difficult for large data sets. A monte carlo of this size takes months just to run after the monte carlo has been completely validated. The bias canceling methods used in this analysis do not need the enormous monte carlo run but rely on other methods to validate the results.

The acceptance of the apparatus for the direction cosines gives a feel for the functioning of the detector. Fig. 6.14 shows the direction cosine distributions. The dip in the histograms near zero is a well-known phenomena, which is due to the difficulty is resolving tracks which lie close together. The $\cos\theta_z$ distribution shows the forward-back asymmetry of the apparatus. The shape of these distributions prevents the direct measurement of the polarization. These distributions would be straight with an asymmetry equal to the slope if the apparatus had a uniform acceptance for all data.

The bias canceling algorithms require acceptance symmetry in the apparatus. In the case of SELEX, this symmetry is 'up' vs. 'down' in the lab frame. Fig. 6.15 shows the apparatus acceptance as a function of the azimuthal angle measured from the horizontal axis in the lab frame. This shows a very strong 'up'-'down' symmetry by the symmetry about the $azimuth = 0$ point.

6.4.1 K-short Analysis

The K-short is a spin 0 object and therefore can not exhibit any preference in the direction of it's decay products. For this analysis, the decay $\kappa_s \rightarrow \pi^+\pi^-$

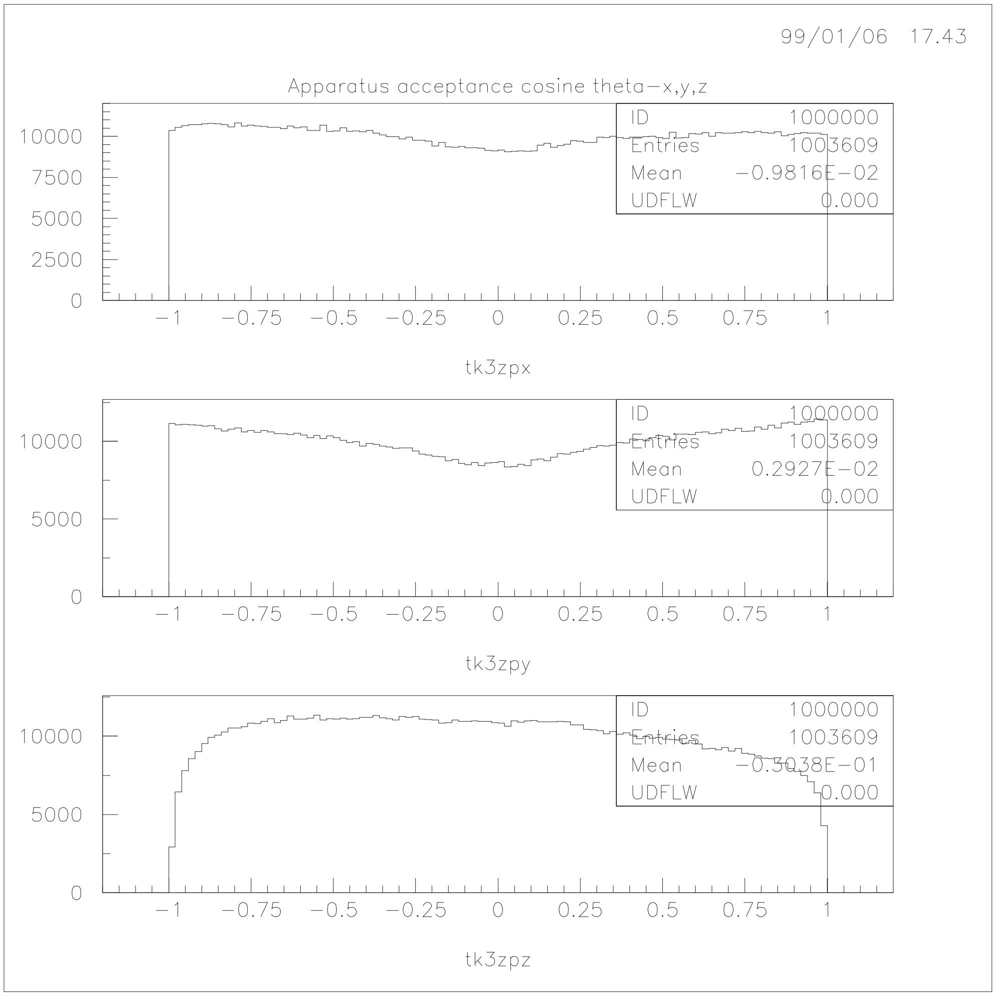

Figure 6.14: Direction cosine distributions in the λ^0 rest frame

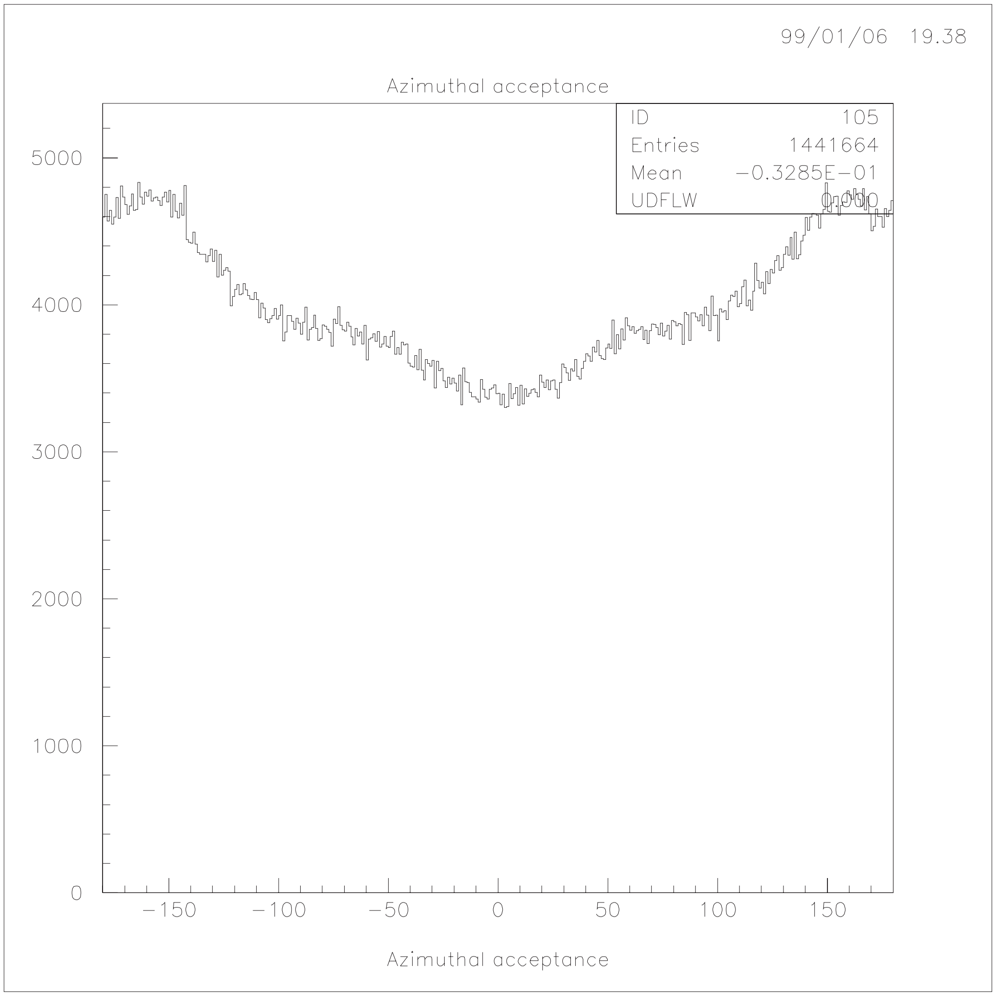

Figure 6.15: Acceptance as a function of angle to the x-axis

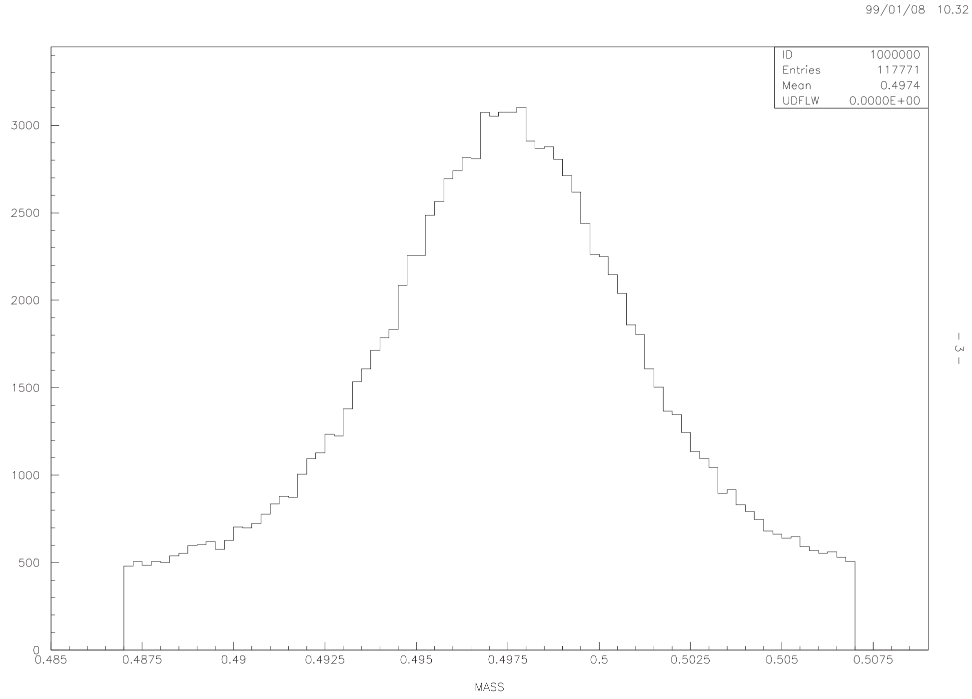

Figure 6.16: K-short mass plot for data used in the analysis

was used. This decay has a branching ratio of 68.61%. In the rest frame of the kaon, the direction of the pions is isotropic and therefore should exhibit no polarization. The mass plot of the kaon's used from PASS1 is shown in Fig. 6.16. The analysis of the kaon was identical to the lambda with the π^+ playing the part of the proton and the kaon playing the part of the lambda. Even though the phase space of the daughters is different for the two decays, it is never the less, a good check of the polarization analysis technique.

The acceptance for the direction cosines of the k-short is shown in Fig. 6.17. The one feature of note is the peak at the upstream end of the $\cos\theta_z$

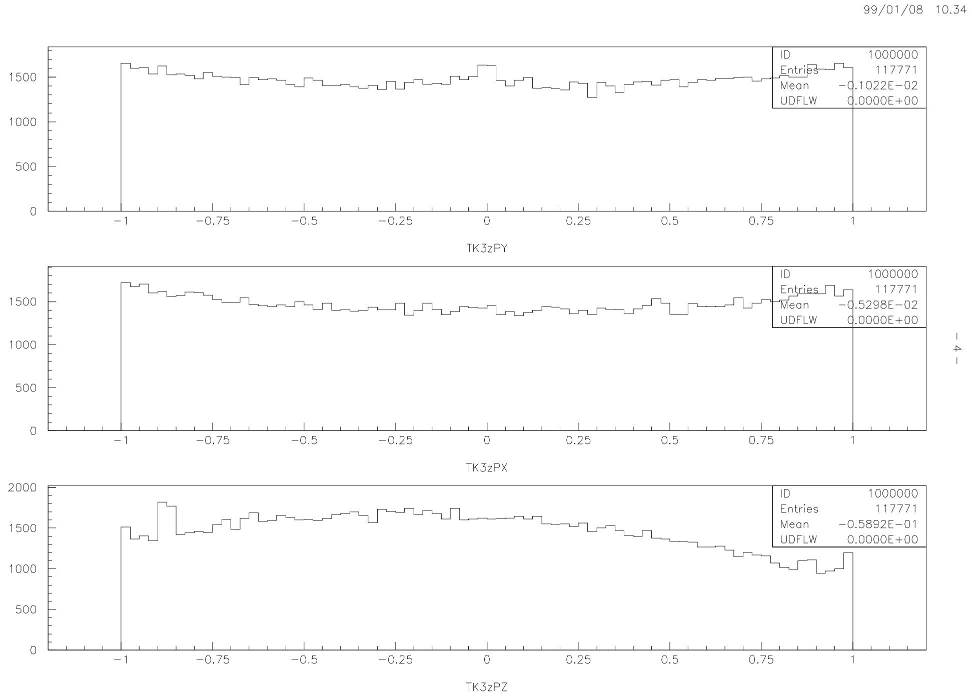

Figure 6.17: K-short direction cosine acceptance for data used in the analysis

histogram which is caused by lambda decays misidentified as k-short events. Otherwise, the distributions are very similar to those shown for the lambda.

The analysis of the k-short gave an average polarization value of $-0.003 \pm 0.007\%$ with a reduced χ^2 of 0.07, which is in very good agreement with the known value of 0.0% polarization.

Fig. 6.18 shows the measured asymmetry for the k-short using the geometric mean method and Fig. 6.19 shows the measured asymmetry for the k-short using the arithmetic mean method. Clearly, within the statistical errors shown, the net asymmetry is zero - as expected.

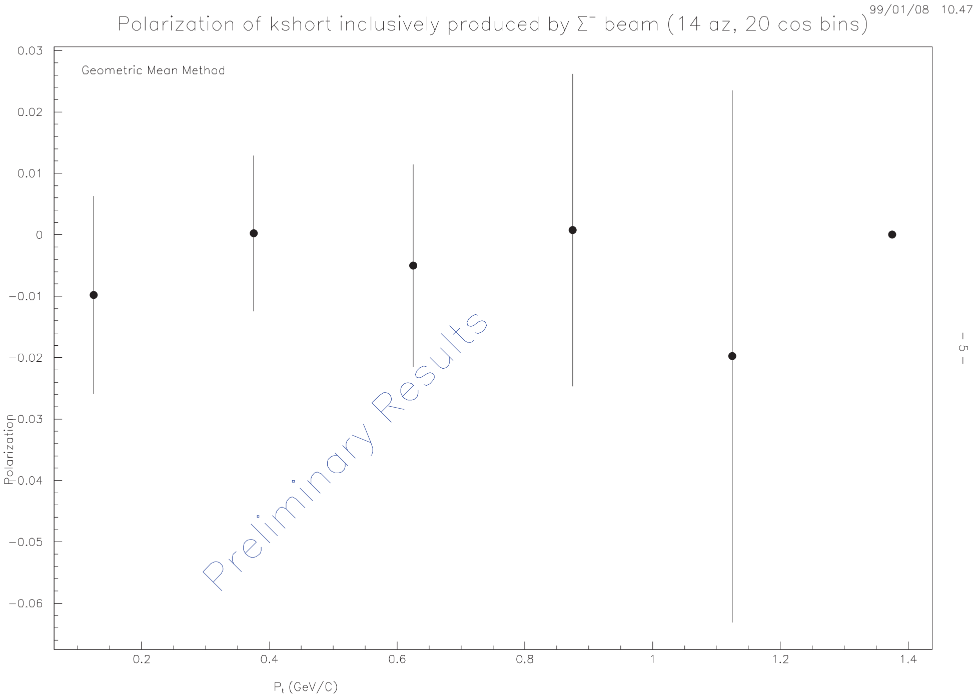

Figure 6.18: K-short polarization using the geometric mean method

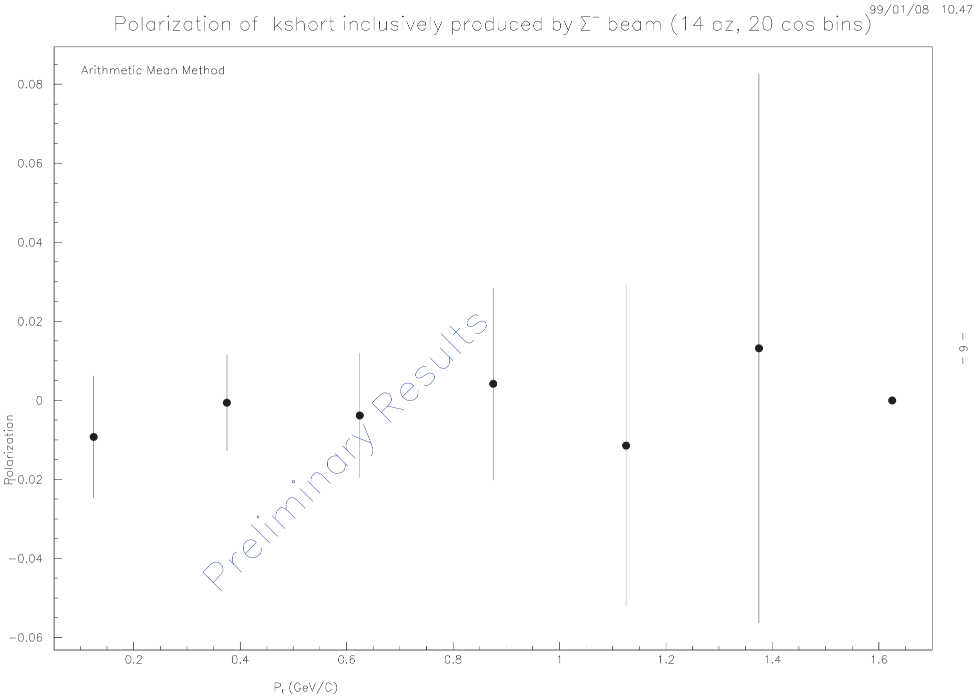

Figure 6.19: K-short polarization using the arithmetic mean method

6.4.2 Monte Carlo Simulation

A second method of algorithm validation is the use of simulated data with an input polarization. This method was used extensively during the development of the algorithms. In using a monte carlo generator it is first necessary to have the simulation reproduce the phase space and other parameters of the actual data. For this, the real data p_t distribution was fit to the function:

$$p_t = ax \exp\left(-bx^2\right) \tag{6.5}$$

as can be seen in Fig. 6.20, and the x_f distribution was fit to

$$x_f = a\sqrt{x^{-2} - 1}(1 - x)^b \tag{6.6}$$

as can be seen in Fig. 6.21. The values obtained for a and b became inputs into the monte carlo.

For the beam profile, a subset of the real data was used. This allowed for an accurate depiction of the beam which was critical for a good simulation. The beam profile used can be seen in Fig. 6.22. The resulting lambda, proton and pion profiles generated by EXP can be seen in Fig. 6.23, Fig. 6.24 and Fig. 6.25. The simulated polarization was not allowed to have any dependence in p_t or in x_f in order to give a clear picture of potential systematic errors. Early on in the analysis, potential systematic errors were observed using this method. These errors turned out to be an artifact of the random number generator being used in EXP. This generator was changed to RANLUX from the CERN library used at the highest level of luxury. Once this was installed, the observed errors disappeared.

The output of EXP was used in many ways. By removing the apparatus acceptance requirements from EXP the output polarization was measured

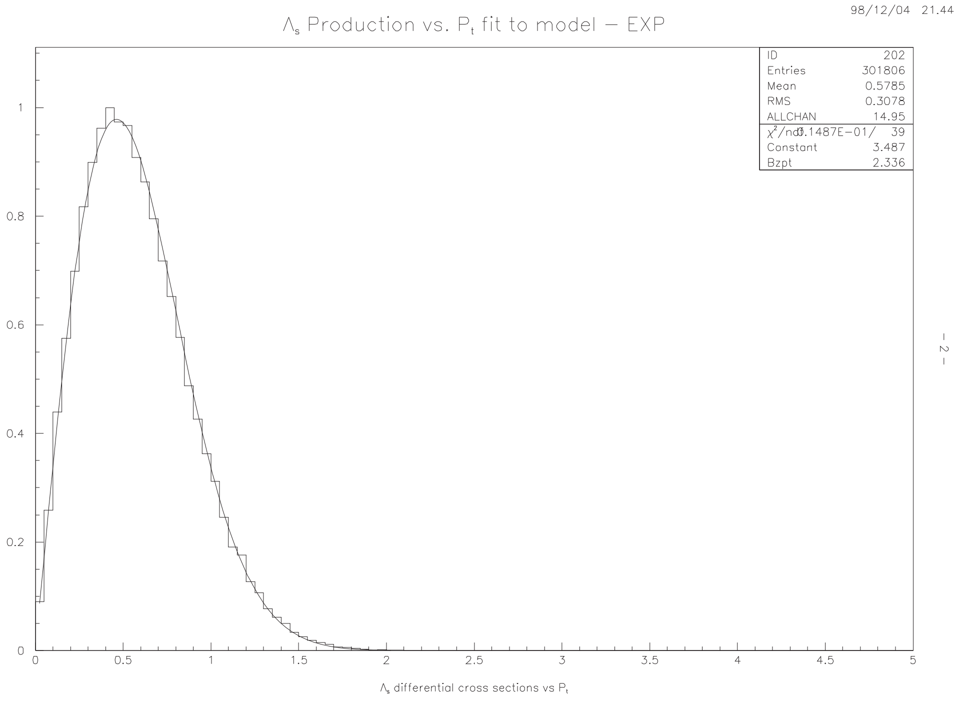

Figure 6.20: EXP production model fit to data for p_t

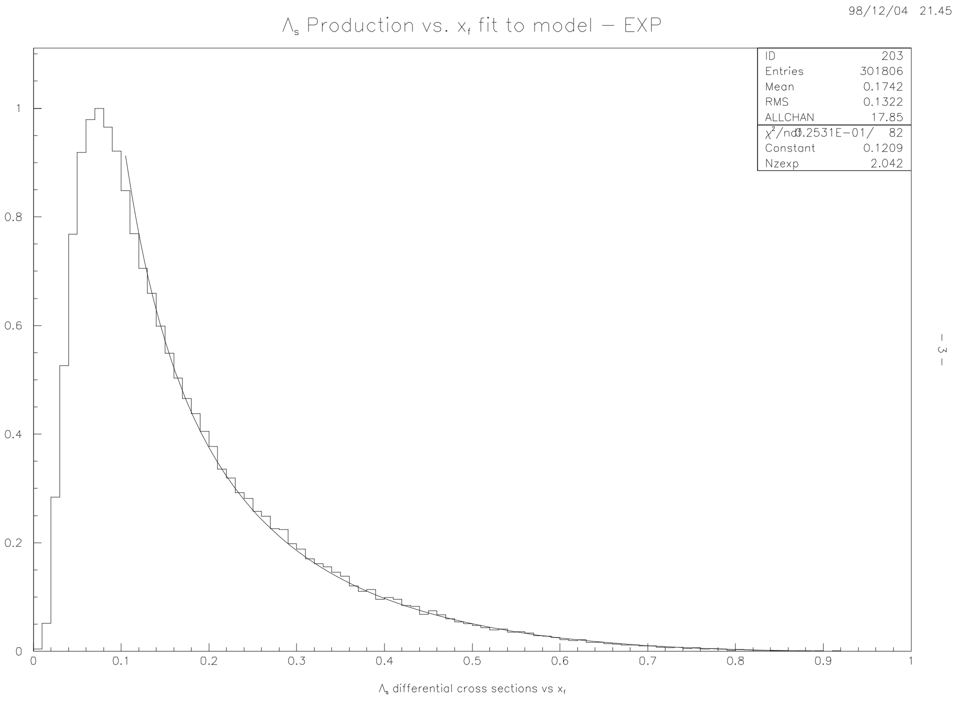

Figure 6.21: EXP production model fit to data for x_f

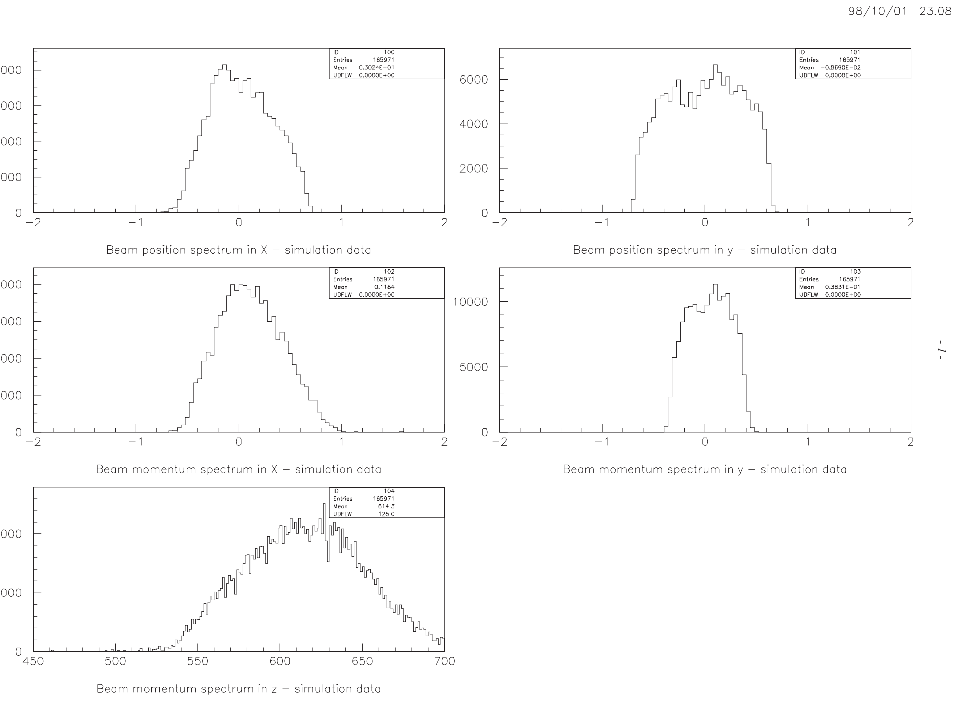

Figure 6.22: EXP input Σ^- beam profile used for event generation

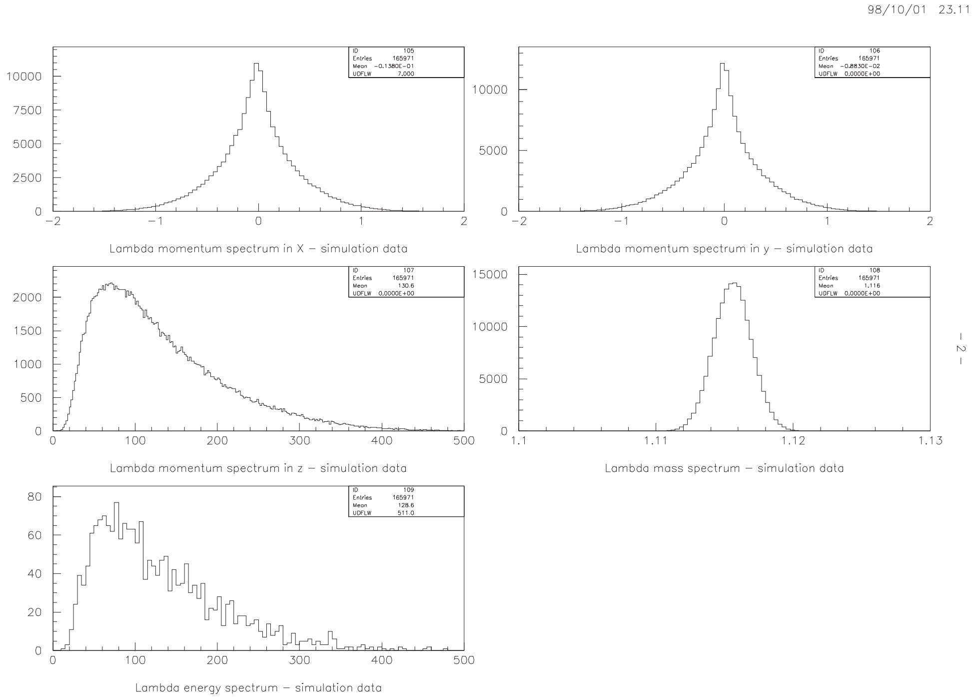

Figure 6.23: EXP output Λ^0 profile for successful events

98/10/01 23.13

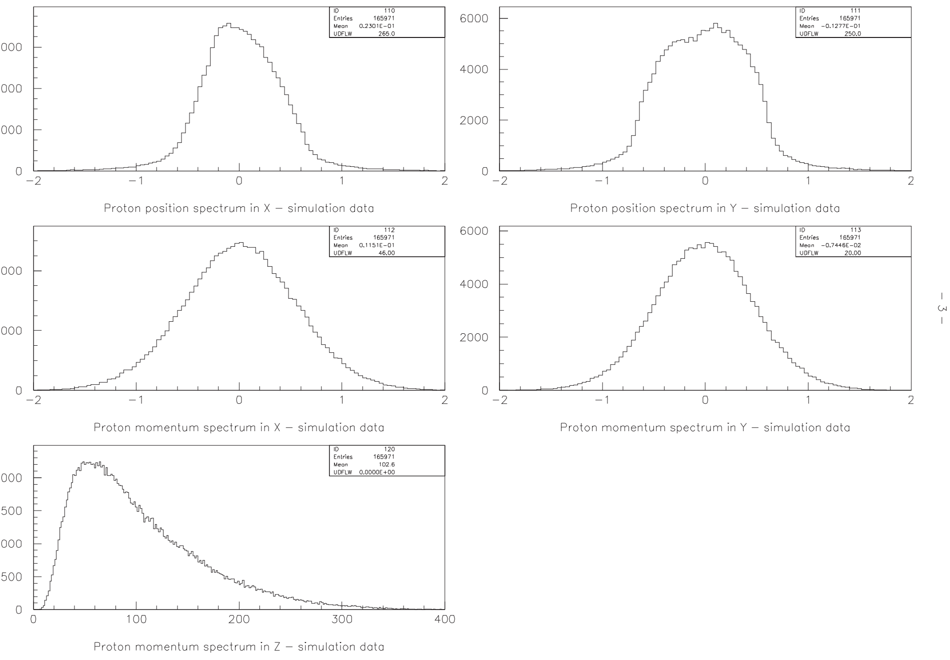

Proton position spectrum in X – simulation data

Proton position spectrum in Y – simulation data

Proton momentum spectrum in X – simulation data

Proton momentum spectrum in Y – simulation data

Proton momentum spectrum in Z – simulation data

Figure 6.24: EXP output proton profile for successful events

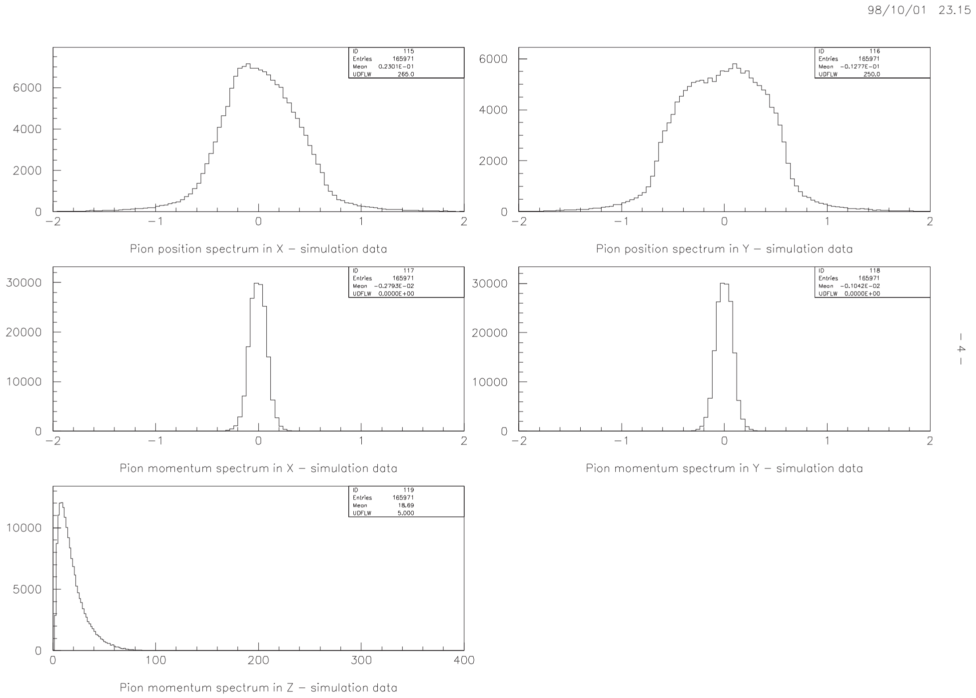

Figure 6.25: EXP output pion profile for successful events

directly from the slope of the distribution, ensuring the polarization was being simulated correctly. This also was the first level test of the algorithms. Next apparatus requirements were used in EXP and again the output was compared with the results found using the bias canceling techniques. This worked well in the initial development, but the geometric simulation was insufficient to properly test the algorithms. Hence, the EXP output of an embedding file was added so a full detector simulation could be used.

6.4.3 Embedding

The embedding feature of SOAP allowed for a full simulation of the experiment using monte carlo generated data. This method allowed data with a known polarization to be input into the software and then analyzed using the same analysis as the real data. For this, many different polarizations were used to test the full range of the data. The results for and input polarization of -10% is shown in Fig. 6.26. No dependence on the input polarization was found in the analysis. The data was checked in a range from -40% to $+40\%$ polarization.

The embedding allowed for four levels of embedding. All four levels were used in the validation of the analysis software. At the initial level, the data is embedded without smearing and without background events. This has the feature of testing the acceptance of the apparatus without the complications of multiple scattering. At the second level, the data is embedded with smearing but still without background events. The third level adds the background events without smearing of the embedded events, and the forth level adds both background events and smearing of the embedded events. Although statistical fluctuations were found within the results of each level,

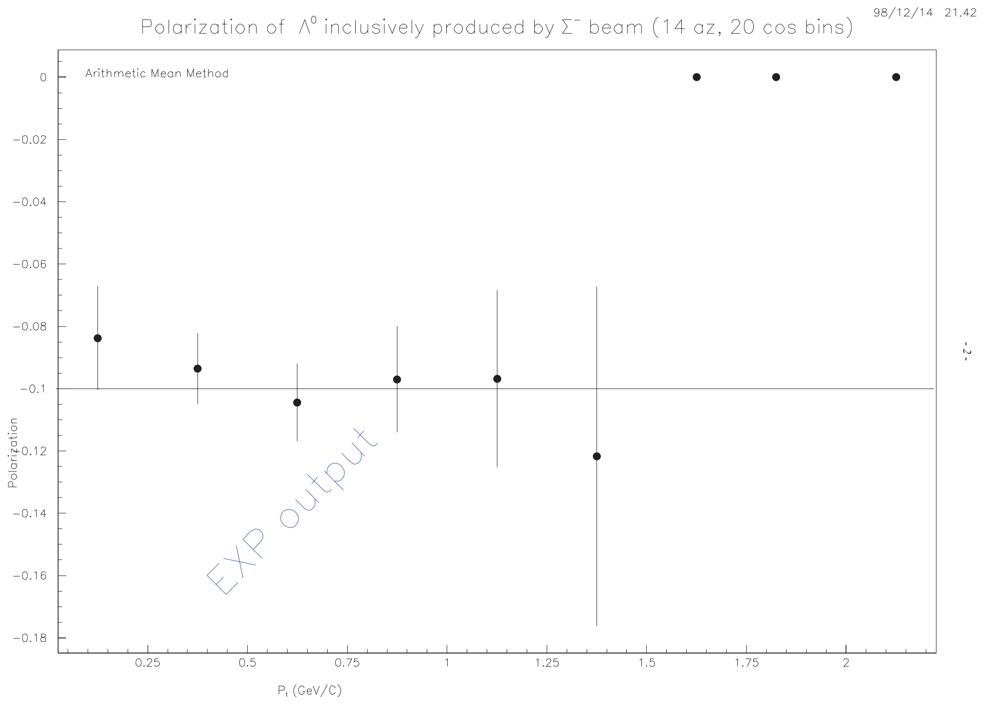

Figure 6.26: EXP monte carlo data embedded with a -10% polarization

no systematic changes were observed.

6.5 Systematic Error Analysis

Perhaps the most difficult sources of errors to observe are the systematic errors. Systematic errors are biases in the final result as a result of the way in which the data set is defined. Most of the time spent on errors analysis of these results was in looking for systematic errors. Any cut or slicing of data was a potential source and had to looked at individually. The techniques involved varied depending on the type of selection used in the analysis.

The strong left-right asymmetry inherent in the detector was a potential source of errors. Fig. 6.27 and Fig. 6.28 show the skewed distributions of the daughter particles along the x-axis (perpendicular to the polarization axis). This bias is a result of the preference of the detector to detect negative particles as a result of the spectrometer magnets. This is the bias which the bias canceling algorithms are designed to eliminate. This ability of the algorithms to remove the bias was looked at in several ways.

This bias is observed in embedded data which both helps to validate the embedding and validate the bias canceling. By showing no systematic errors in the output of embedding data where a known polarization was input, suggest the algorithms are removing the biases. Although this is a compelling result, it is insufficient to validate the algorithms.

A second method is to utilize the two perpendicular axes to the polarization axis. Since the polarization can not be along these axes, only bias (false asymmetries) due to the apparatus will be seen. It is these false asymmetries that the algorithms are designed to remove. APPENDIX A gives a more detailed explanation of the method. The polarization should be zero about these axes within statistical limits and this is what was observed, see Fig. 6.29, 6.30, 6.31, and 6.32. This method directly deals with the source of the bias and gives a strong statement about the validity of the bias canceling algorithms.

A second source of systematics errors is the binning scheme used on the data. Initially, the bin size was determined by optimizing the data size in each bin. Then, the bin sizes were separately, systematically varied and the change in the polarization was observed. For bins where no dependence of the polarization on the variable being binned was observed or expected,

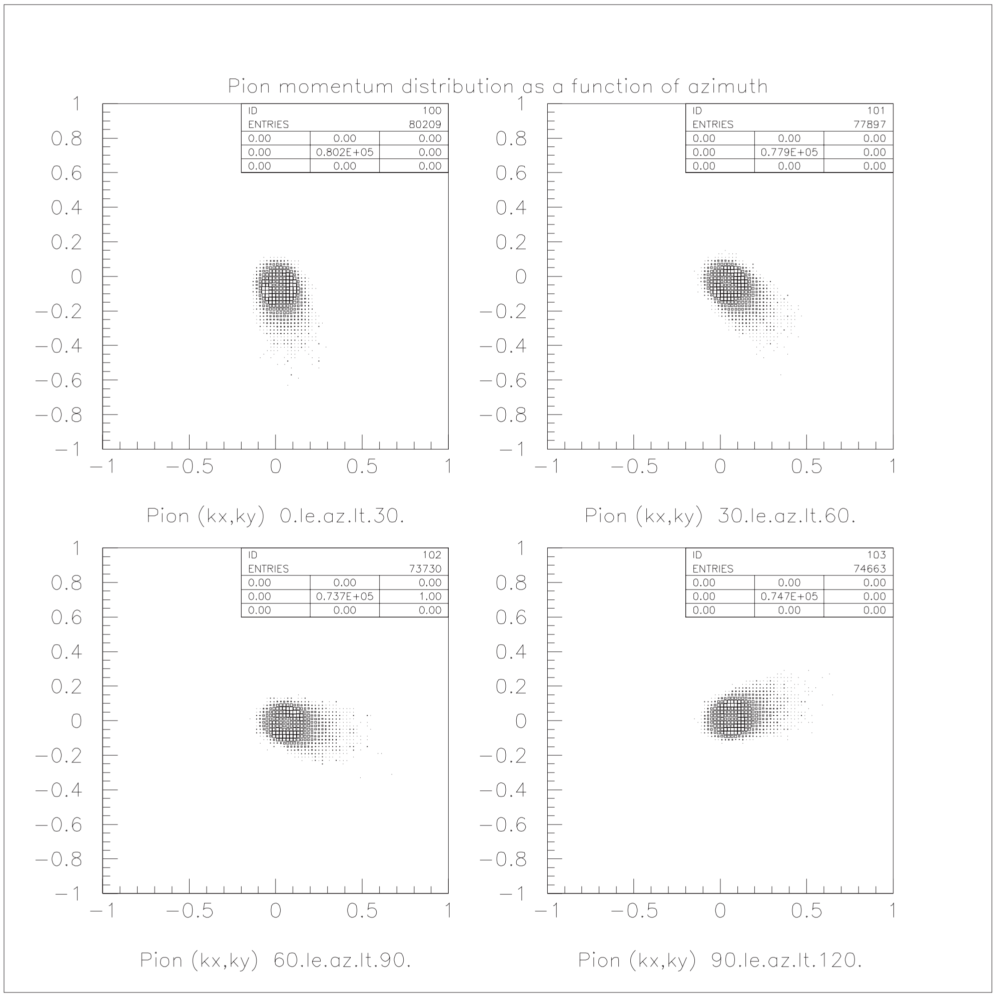

Figure 6.27: Pion momentum vs. azimuth showing the left-right asymmetries

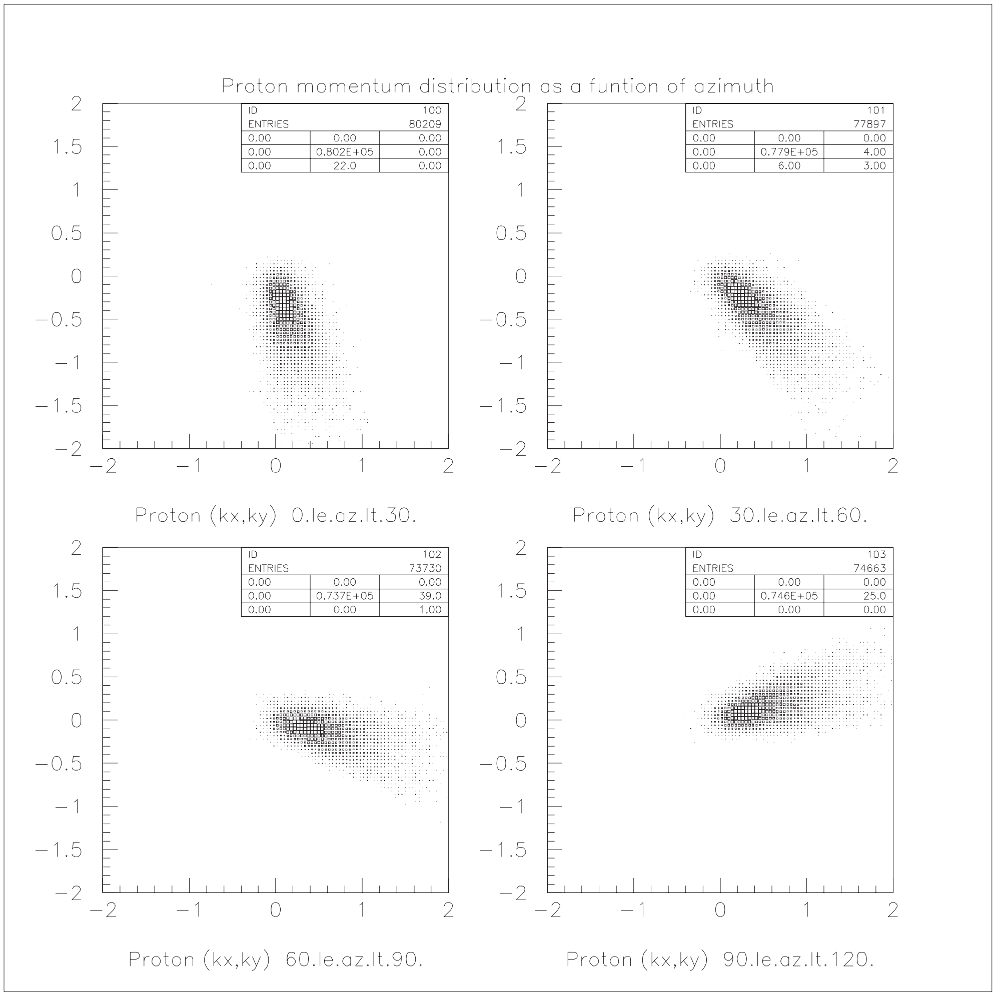

Figure 6.28: Proton momentum vs. azimuth showing left-right asymmetries

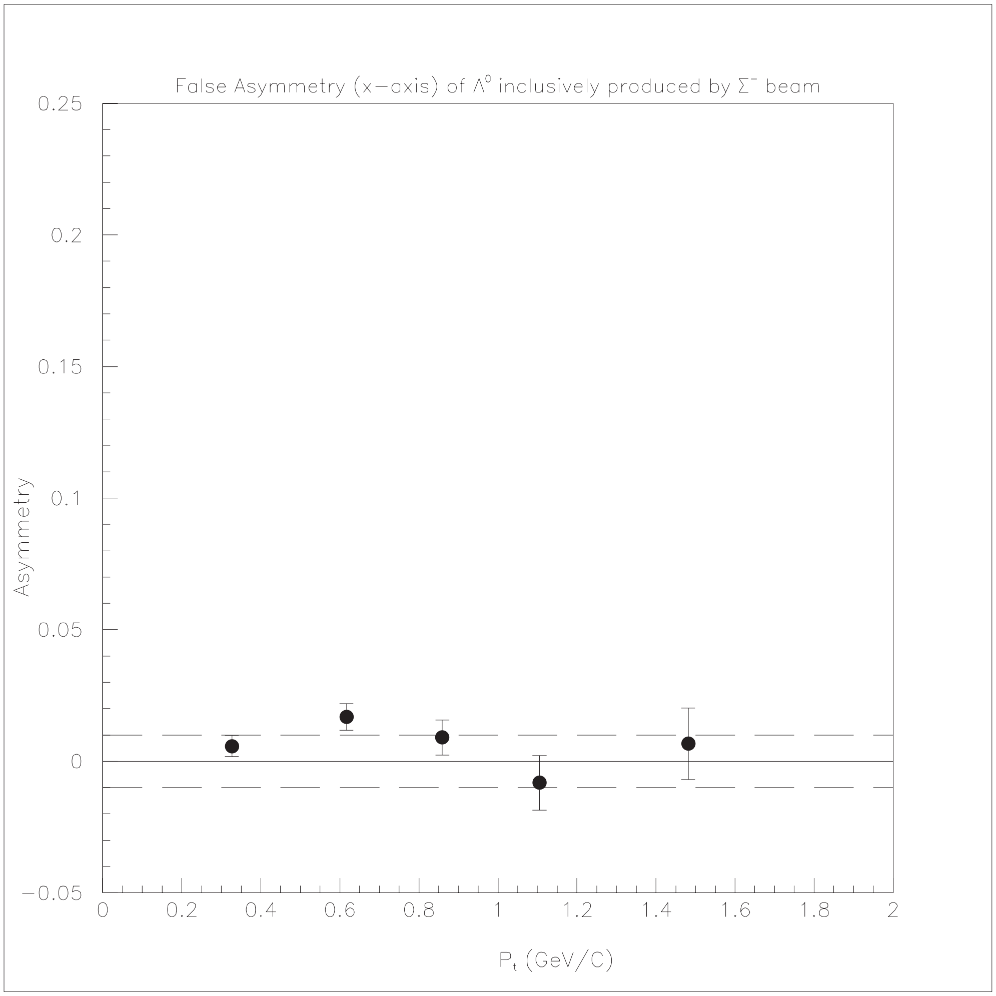

Figure 6.29: False asymmetries along the x-axes vs. p_t (dashed lines = 1%)

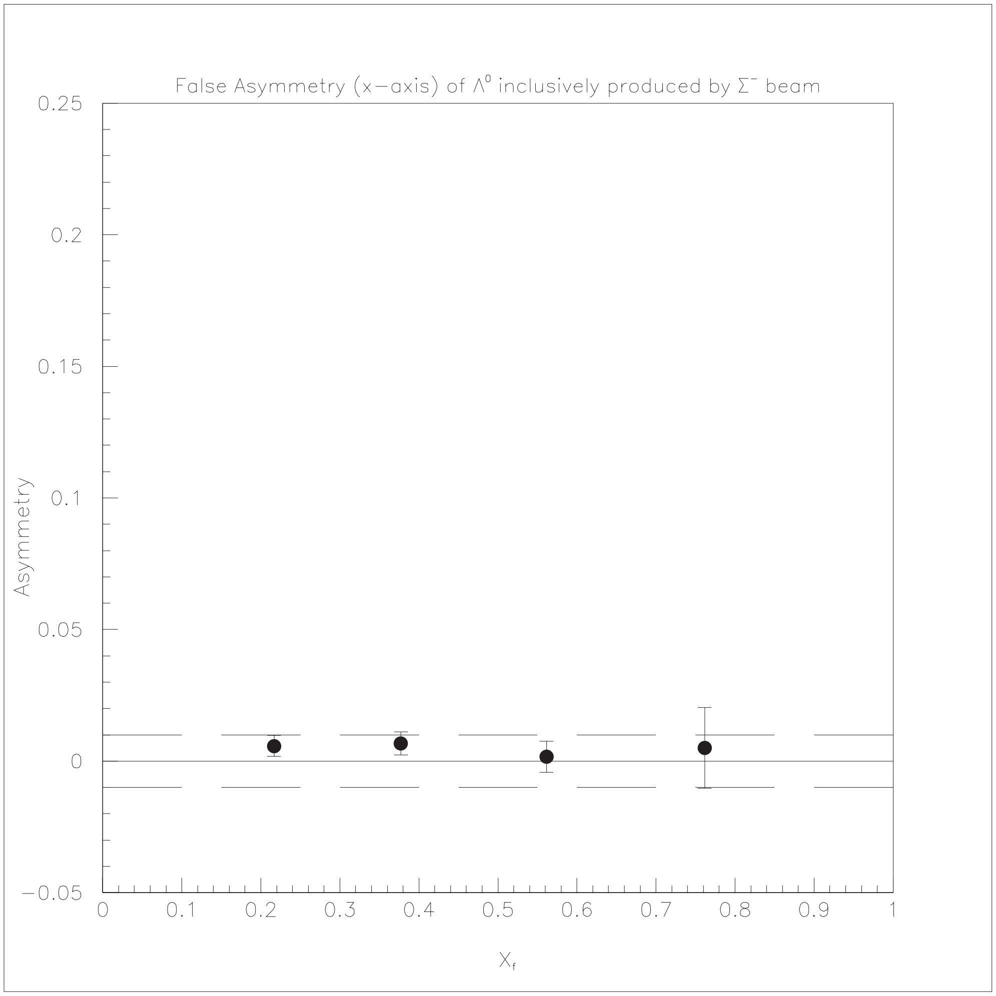

Figure 6.30: False asymmetries along the x-axes vs. x_f (dashed lines = 1%)

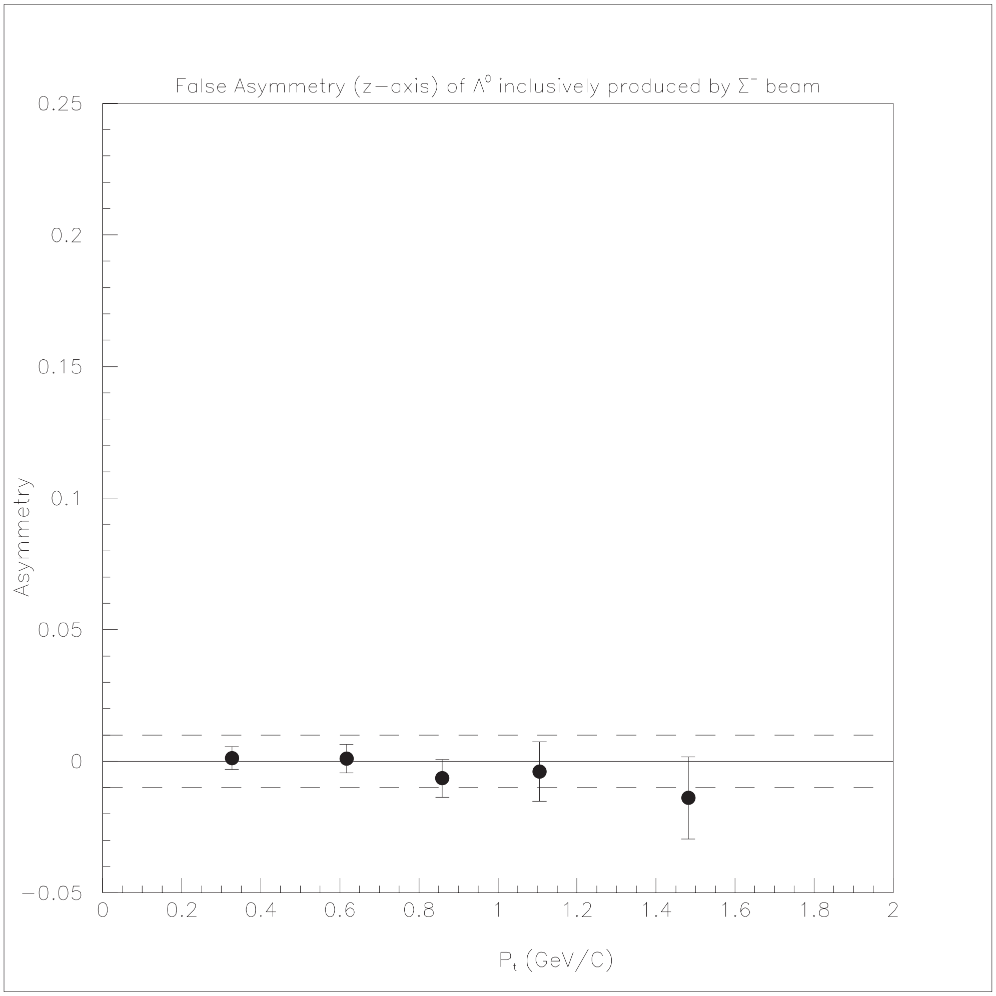

Figure 6.31: False asymmetries along the z-axes vs. p_t (dashed lines = 1%)

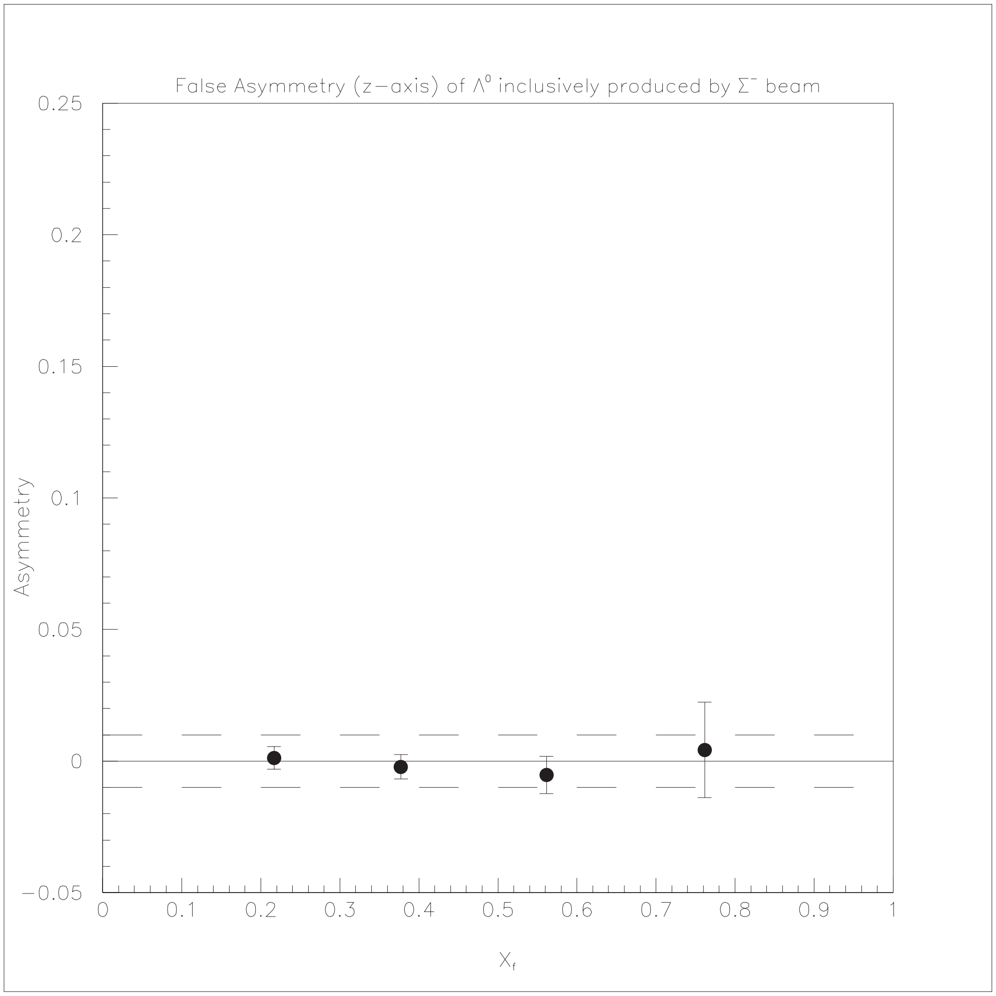

Figure 6.32: False asymmetries along the z-axes vs. x_f (dashed lines = 1%)

the bin size was varied until a region where little change in the output was observed. At this point, the results showed no dependence on the size of the bin. Typically, the lower limit on the number of bins was easy to find, as the resultant polarization tended to vary widely when the number of bins was too small. At the other end, the polarization tended to not vary until the bin size became so small that the amount of data within each bin became the source of the fluctuations. This method was used to select the bin sizes used for this analysis. Analysis of the systematic errors associated with that size then continued identically for all binned variables.

For variables for which the polarization showed a dependence (p_t and x_f), the binning scheme was determined by the desire to have the statistical errors for each bin be roughly equivalent. The systematic error analysis then continued identically of all binned variables and selection cuts.

The method used to analyze the final systematic errors for the data consisted of the following: Data which just passed the selection criteria was considered the outlying group (or test set) and the larger group of data which was clearly within the selection criteria was consider the main group. Both groups of data were analyzed and then the polarization values for a given p_t or x_f bin were compared. The data was fit to the hypothesis that the results were the same (one parameter fit) and the resulting chi-squared's of the fit were evaluated. The chi-squared distribution should have a mean value of one if the hypothesis is correct.

For the mass cut, Fig. 6.33 shows the outlying region compared to the main group, Fig. 6.34 shows the results integrated over x_f as a function of p_t, and Fig. 6.35 shows the results integrated over p_t as a function of x_f.

For the x_f binning, Fig. 6.36 shows the outlying region compared to the

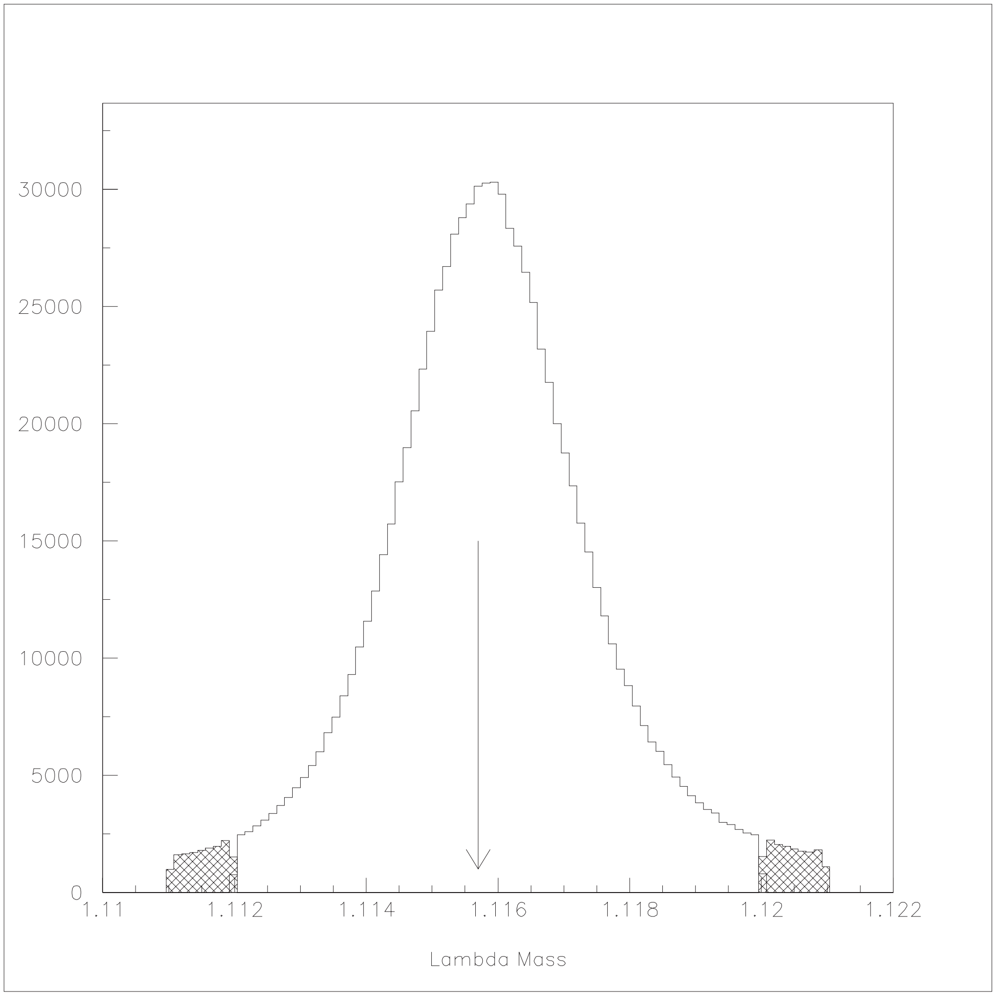

Figure 6.33: Mass cut systematic analysis (shaded=outlying)

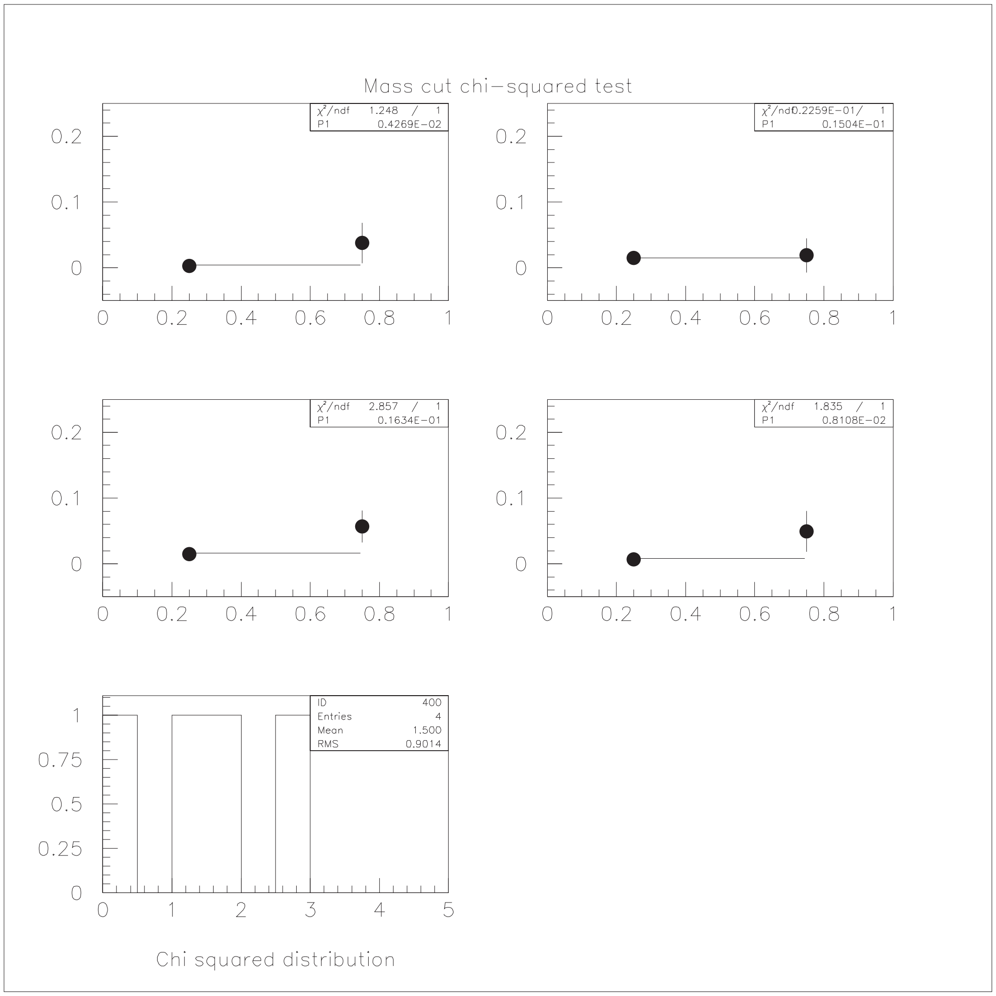

Figure 6.34: Mass cut systematic error analysis (binned in p_t)

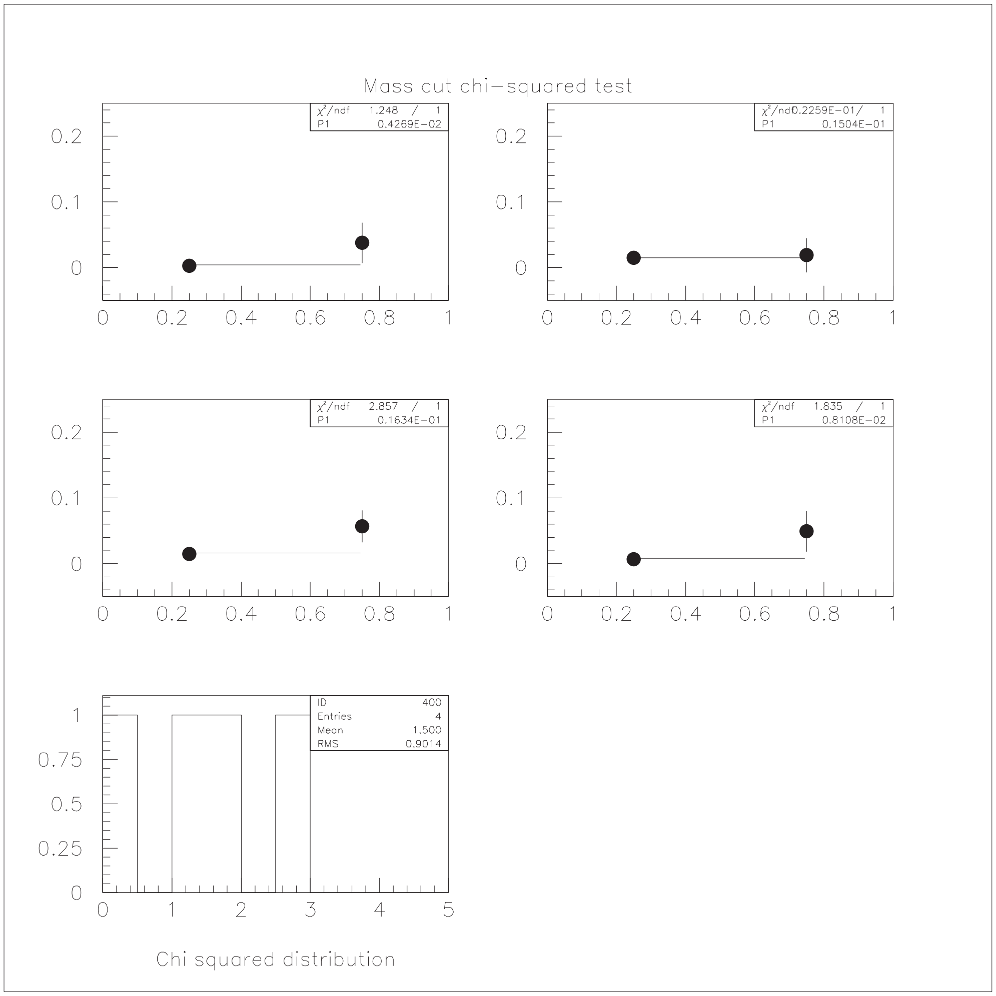

Figure 6.35: Mass cut systematic error analysis (binned in x_f)

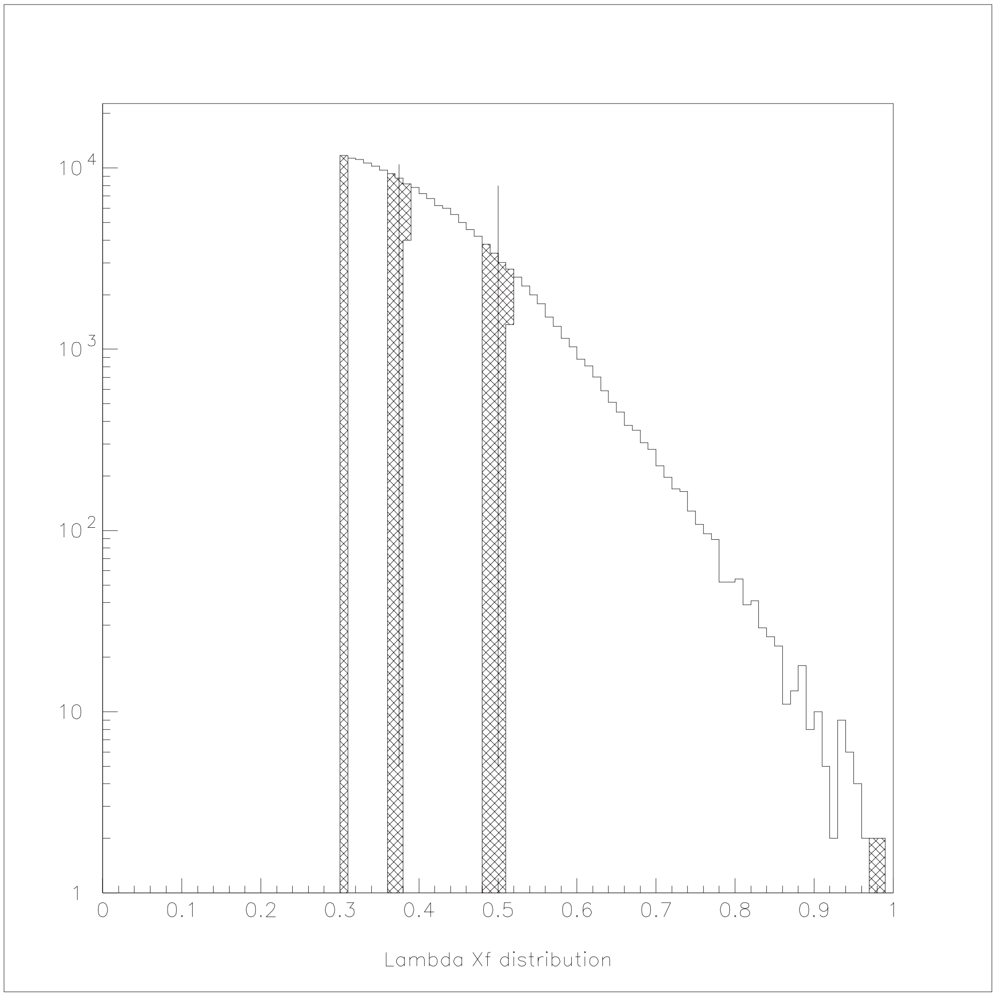

Figure 6.36: X_f cut systematic analysis (shaded=outlying)

main group for the three x_f bins, Fig. 6.37 shows the results integrated over p_t as a function of x_f.

For the p_t binning, Fig. 6.38 shows the outlying region compared to the main group for the four p_t bins, Fig. 6.37 shows the results integrated over x_f as a function of p_t.

The M2 requirement for the pion was effectively a cut on the pion momentum. The outlying group consisted of the low momentum pions which

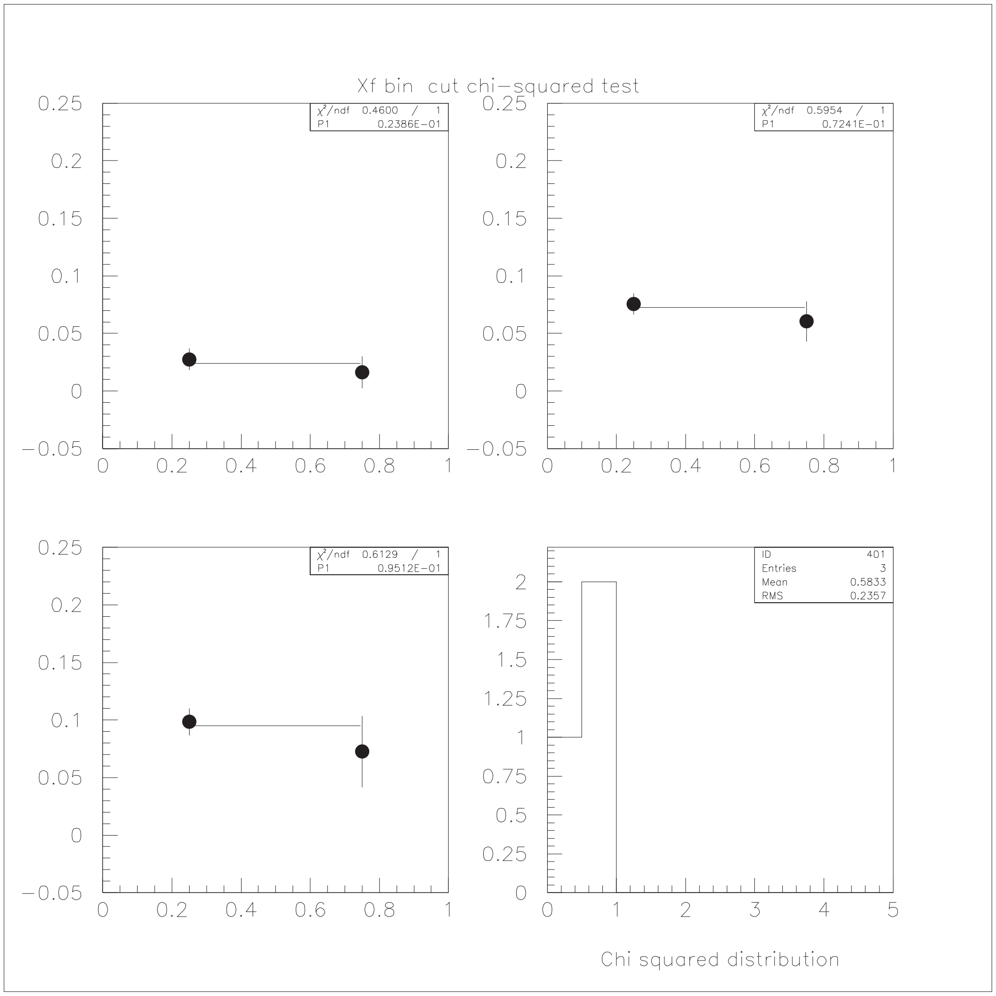

Figure 6.37: X_f binning systematic error analysis

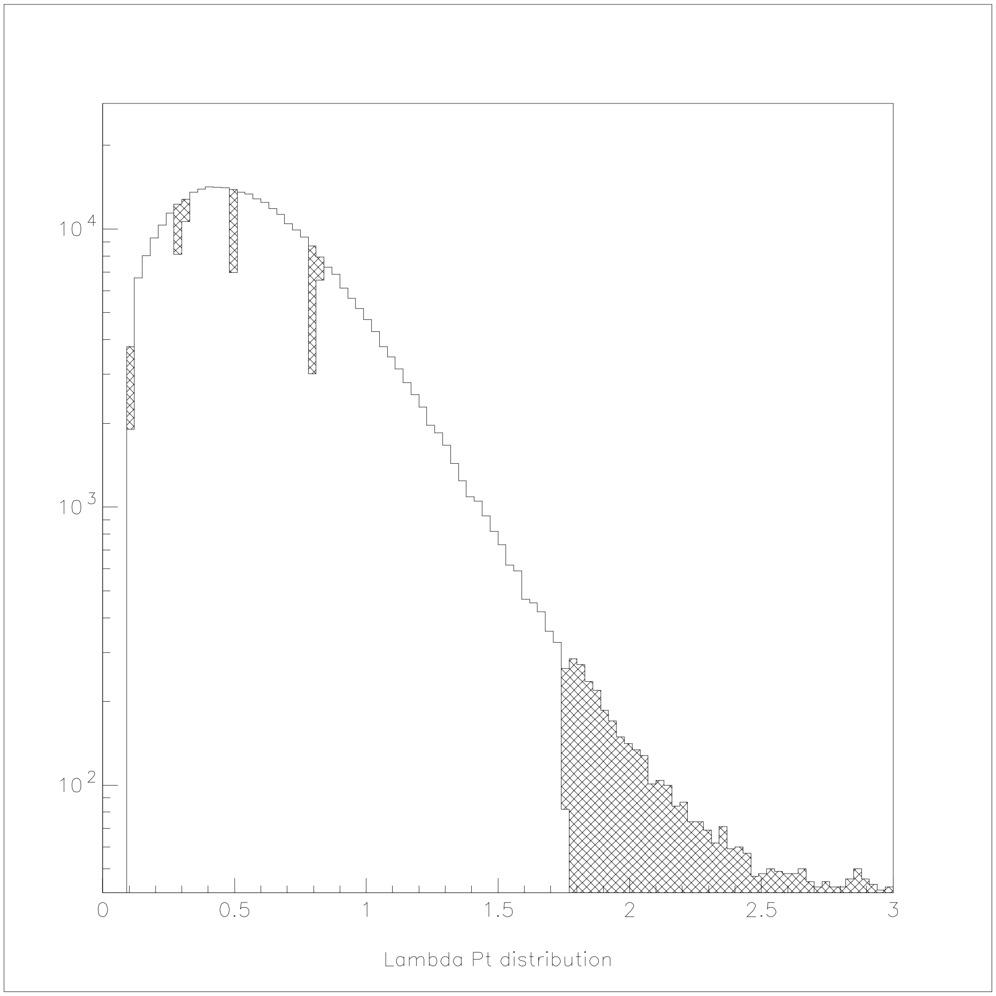

Figure 6.38: P_t cut systematic analysis (shaded=outlying)

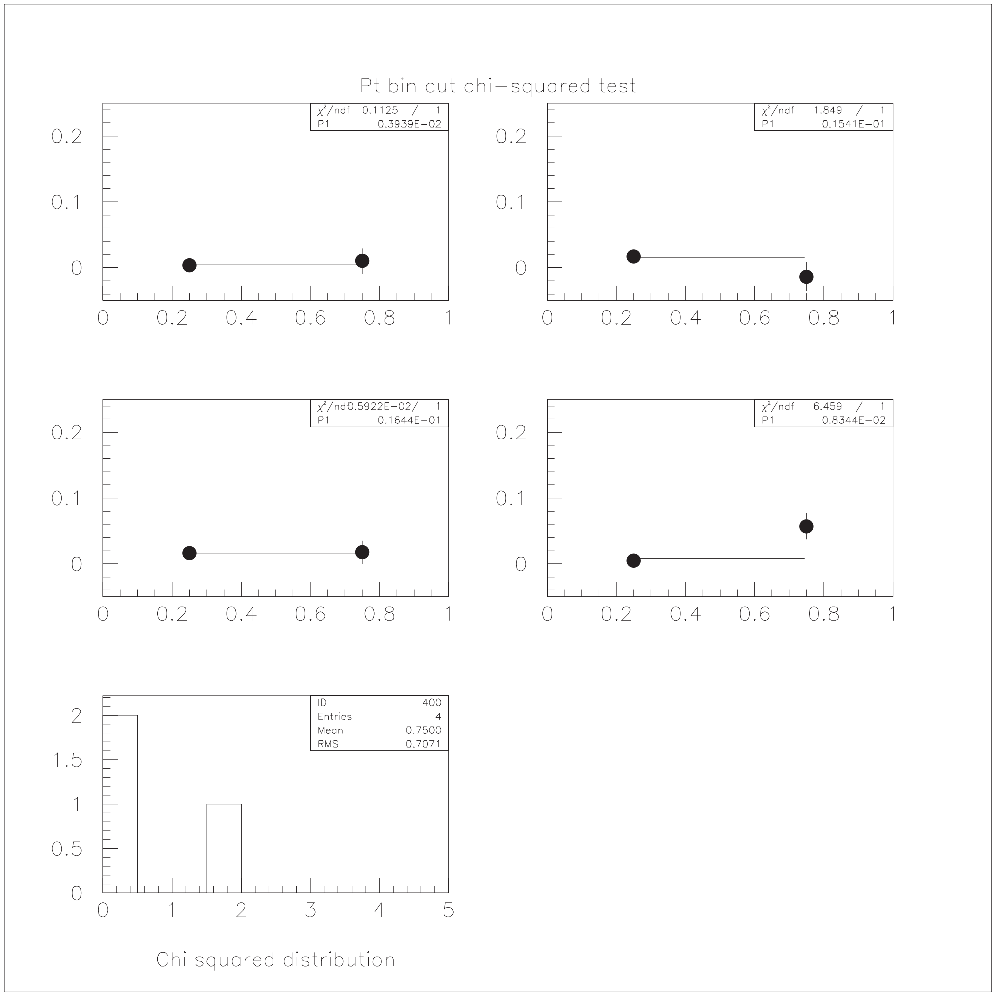

Figure 6.39: P_t binning systematic error analysis

just passed this cut and the main group consisted of the higher momentum pions. The results of this comparison as a function of p_t are shown in Fig. 6.40 and as a function of x_f in Fig. 6.41.

The selection cut removing data where the 'up', 'down' distinction was within the resolution of the software is analyzed in Fig. 6.42 as a function of p_t, and in Fig. 6.43 as a function of x_f.

The requirement of RICH identification of the proton at the exclusion of any lighter particles is analyzed in Fig. 6.44 as a function of p_t, and in Fig. 6.45 as a function of x_f.

With three of for chi-squared's in a distribution, the statistical error is large, but in looking at the distribution for all the chi-squared's the error is reduced. The data for the proton required cut is not used in this distribution, all values were < 0.5. For a one parameter fit, the chi-squared probability distribution is an exponential with a mean value of 1. Fig. 6.46 shows the distribution which has the proper form and mean value.

In reviewing the systematic error analysis, the chi-squared's show only statistical variations. This can be seen by the total distribution of chi-squared's. Therefore, The selection cuts used and binning schemes used for the data analysis show no discernible systematic errors. Hence, the only errors which are important to the final result will be the statistical errors which are a function of the size of the data set.

6.6 Polarization Results

The results of the polarization analysis is shown in Fig. 6.47, and Table 6.6. For this analysis the value $\alpha = 0.642$ was used. The data shows three main characteristics:

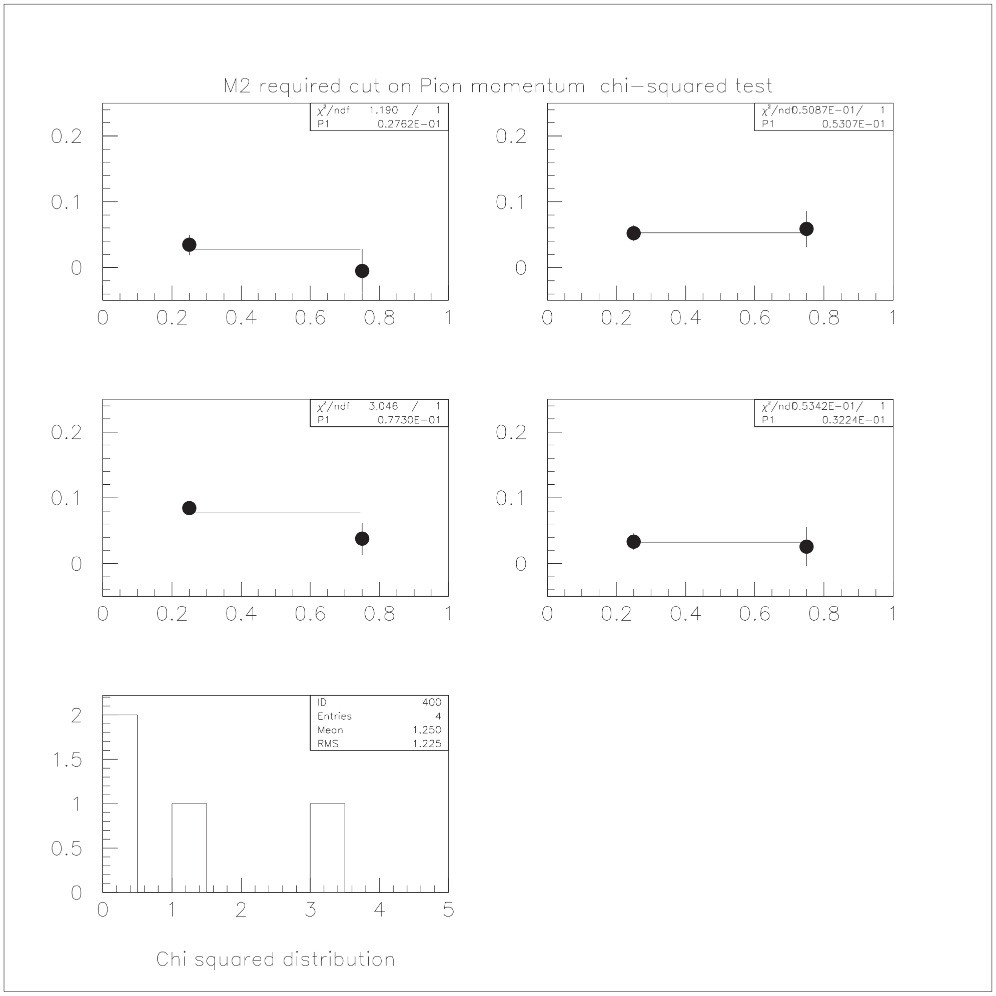

Figure 6.40: Pion M2 cut systematic error analysis (binned in p_t)

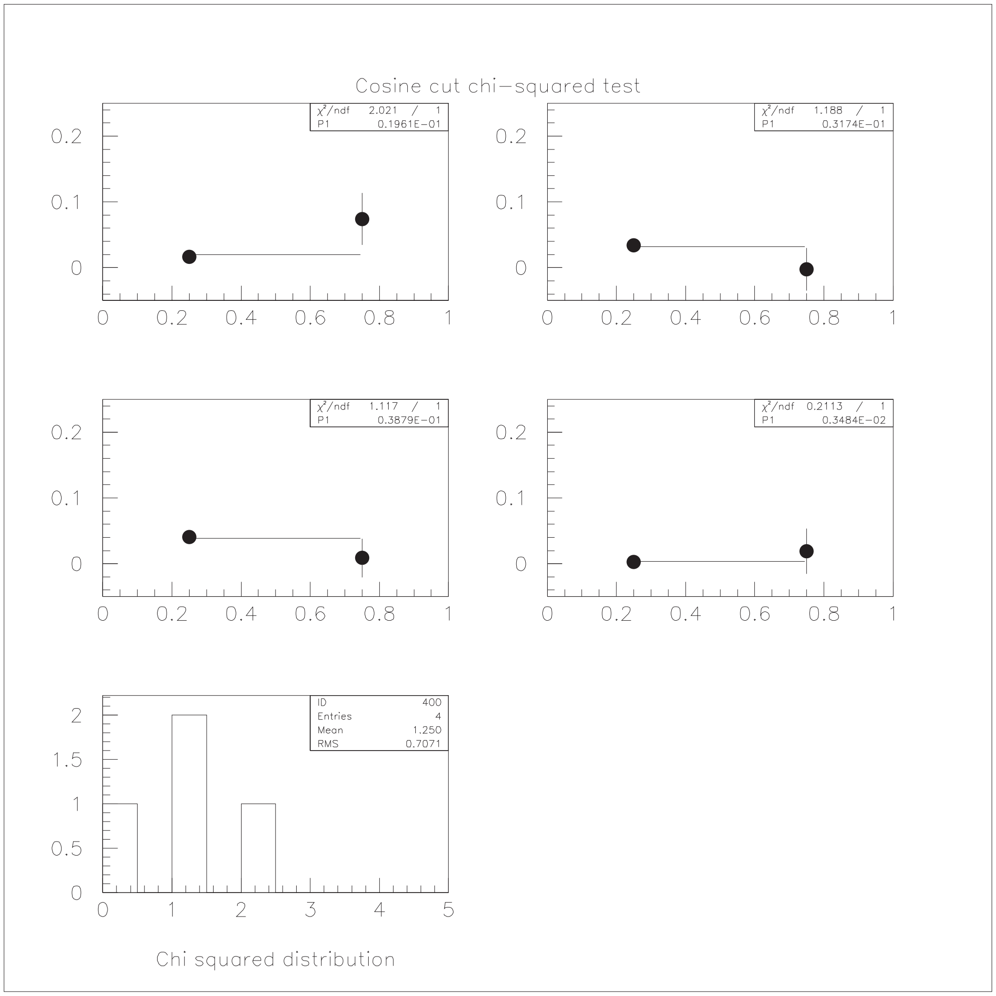

Figure 6.41: Pion M2 cut systematic error analysis (binned in x_f)

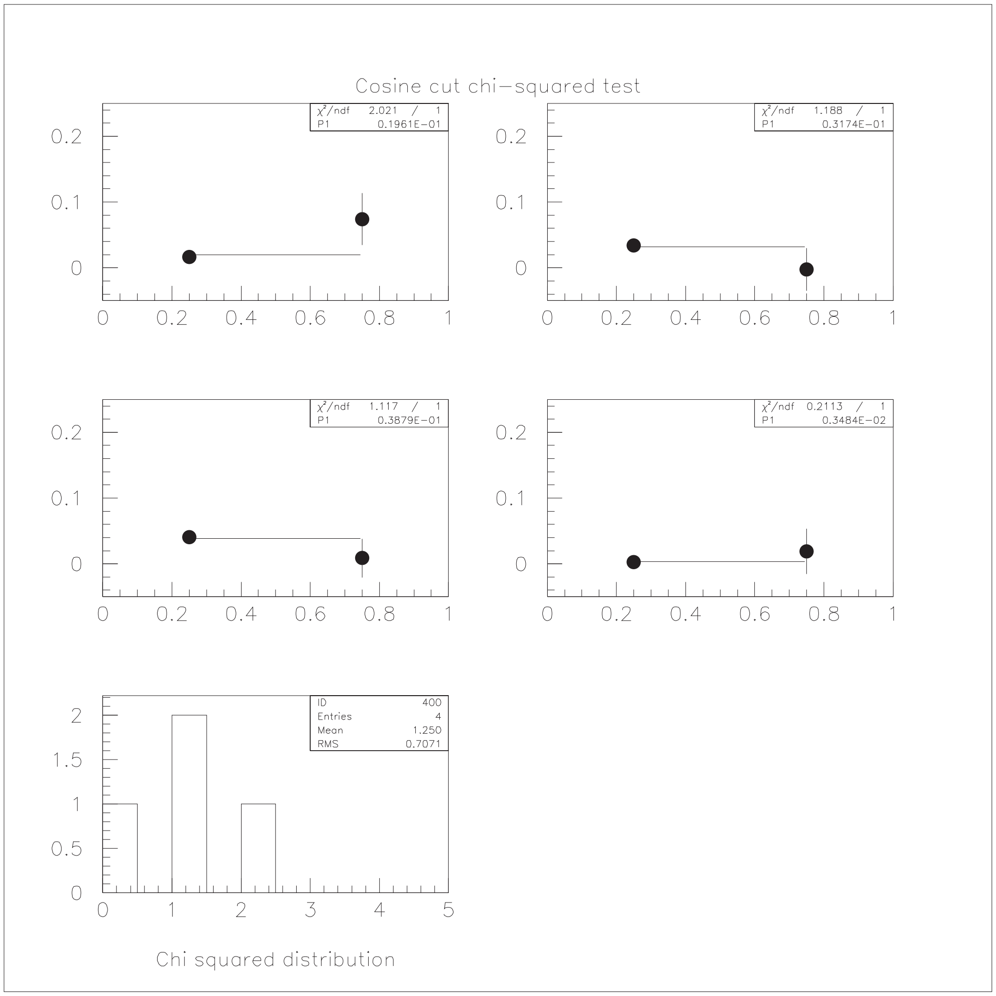

Figure 6.42: Cosine cut systematic error analysis (binned in p_t)

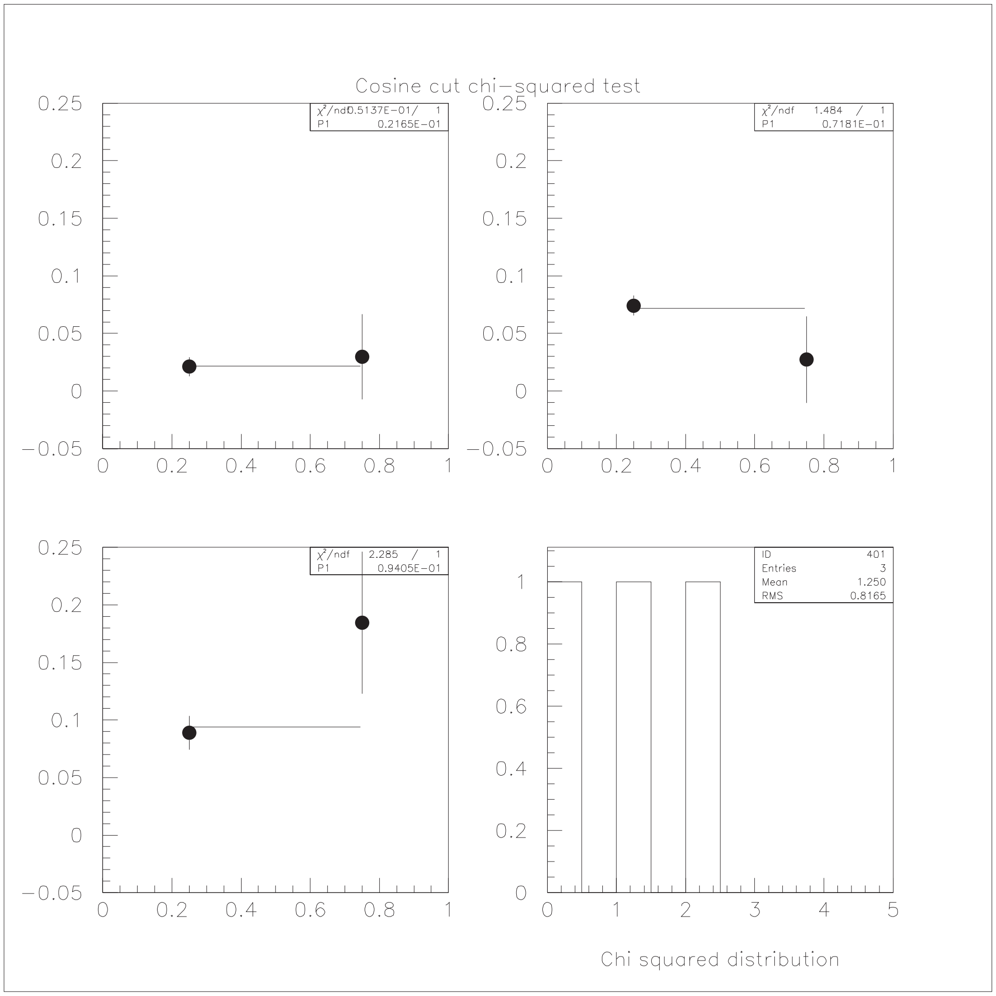

Figure 6.43: Cosine cut systematic error analysis (binned in x_f)

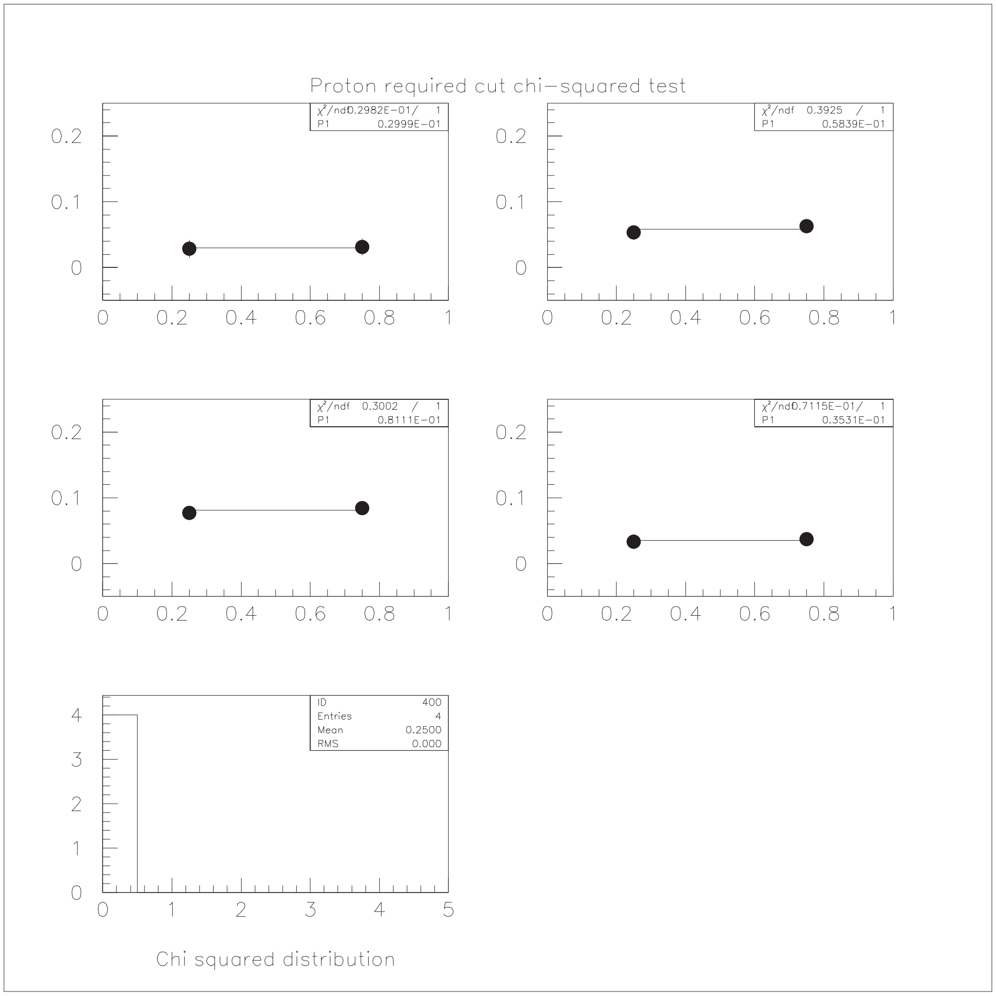

Figure 6.44: Proton required cut systematic error analysis (binned in p_t)

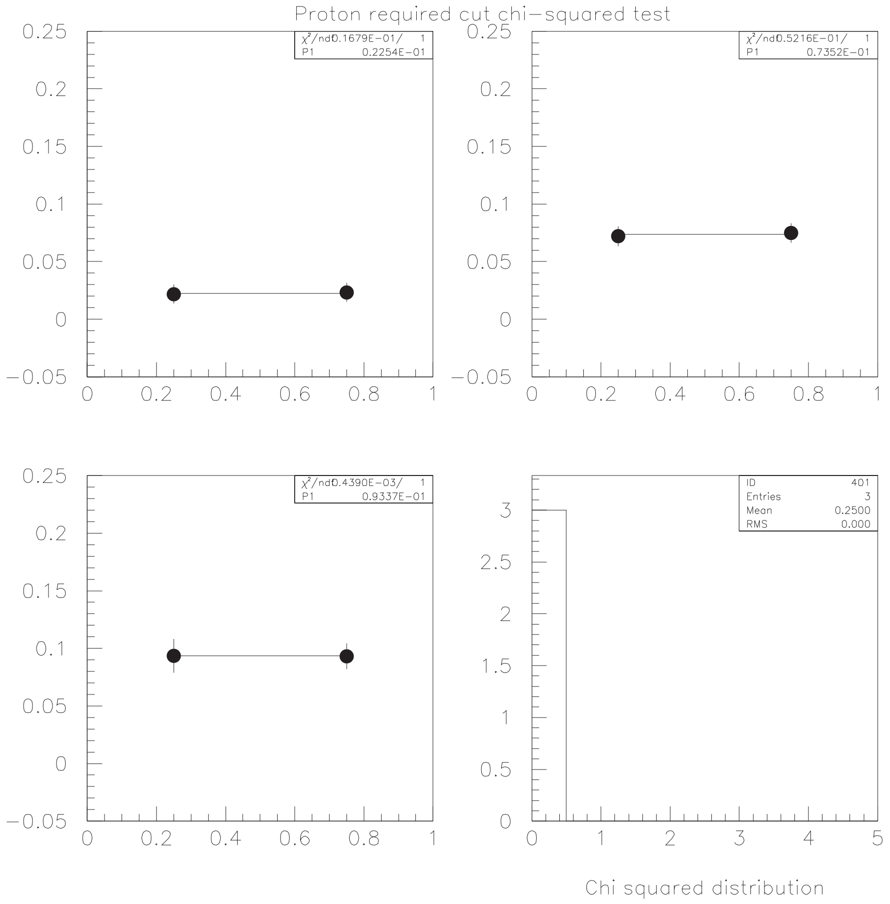

Figure 6.45: Proton required cut systematic error analysis (binned in x_f)

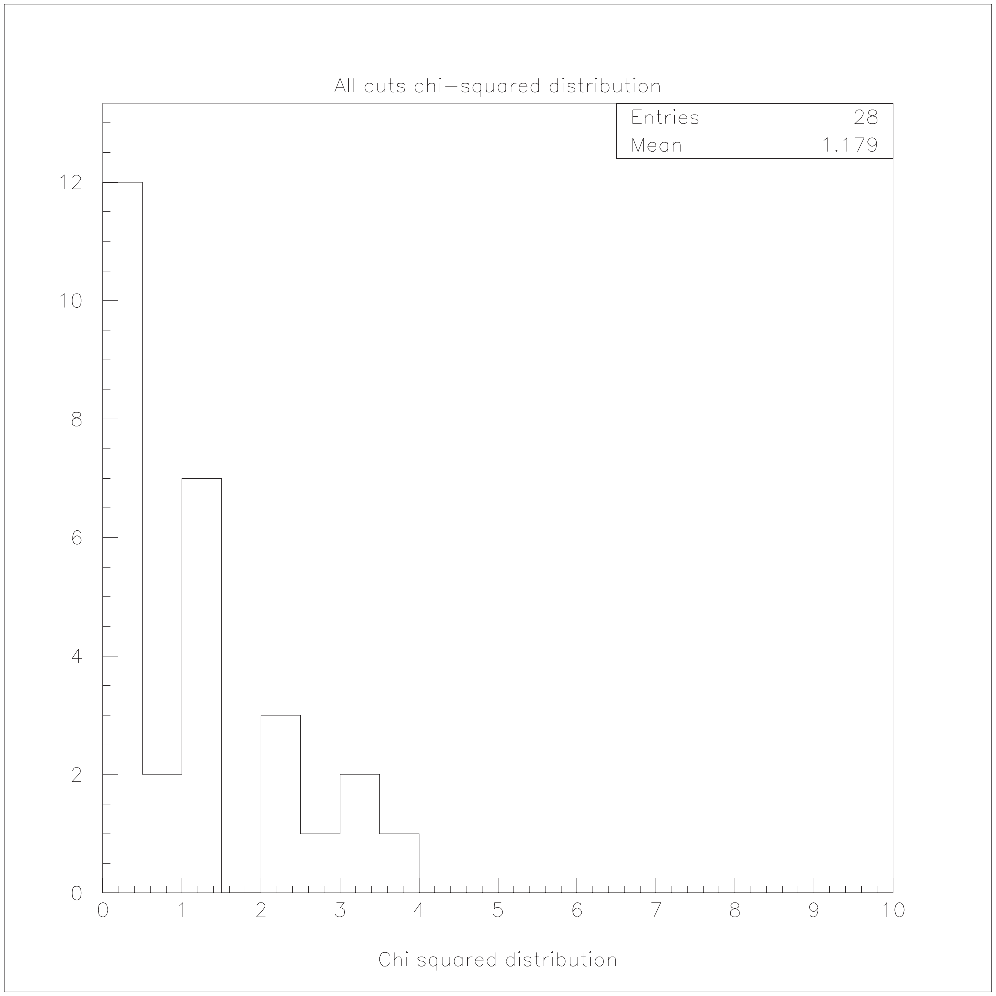

Figure 6.46: Chi squared distribution for systematic error analysis

Table 6.2: Polarization Results (statistical errors only shown)

		$X_f Bin$		
		$0.3 - 0.375$	$0.375 - 0.5$	$0.5 - 1.0$
$P_t Bin$	$< P_t >$	$< X_f >$		
(GeV/c)	(GeV/c)	0.34	0.43	0.58
$0.1 - 0.3$	0.21	0.028 ± 0.020	0.052 ± 0.022	-0.045 ± 0.037
$0.3 - 0.5$	0.40	0.021 ± 0.016	0.074 ± 0.017	0.094 ± 0.030
$0.5 - 0.8$	0.64	0.022 ± 0.015	0.107 ± 0.015	0.165 ± 0.026
> 0.8	1.07	0.008 ± 0.017	0.046 ± 0.018	0.074 ± 0.029

- Positive polarization for $\Sigma^- + A \to \Lambda^0 + X$
- A linear dependence increasing in x_f.
- A p_t dependence which 'turns over' between 0.8 and 1.0.

The largest value of polarization is 16.5% and one value for high x_f and low p_t is negative (although within statistical error of zero). The structure of the polarization as a function of x_f and p_t can be seen in Fig. 6.48 and Fig. 6.49. This structure is similar to that observed in proton and kaon beams for lambda polarization.

A comparison of the two bias canceling techniques can be seen by comparing Fig. 6.48 to Fig. 6.50 and Fig. 6.49 to Fig. 6.51.

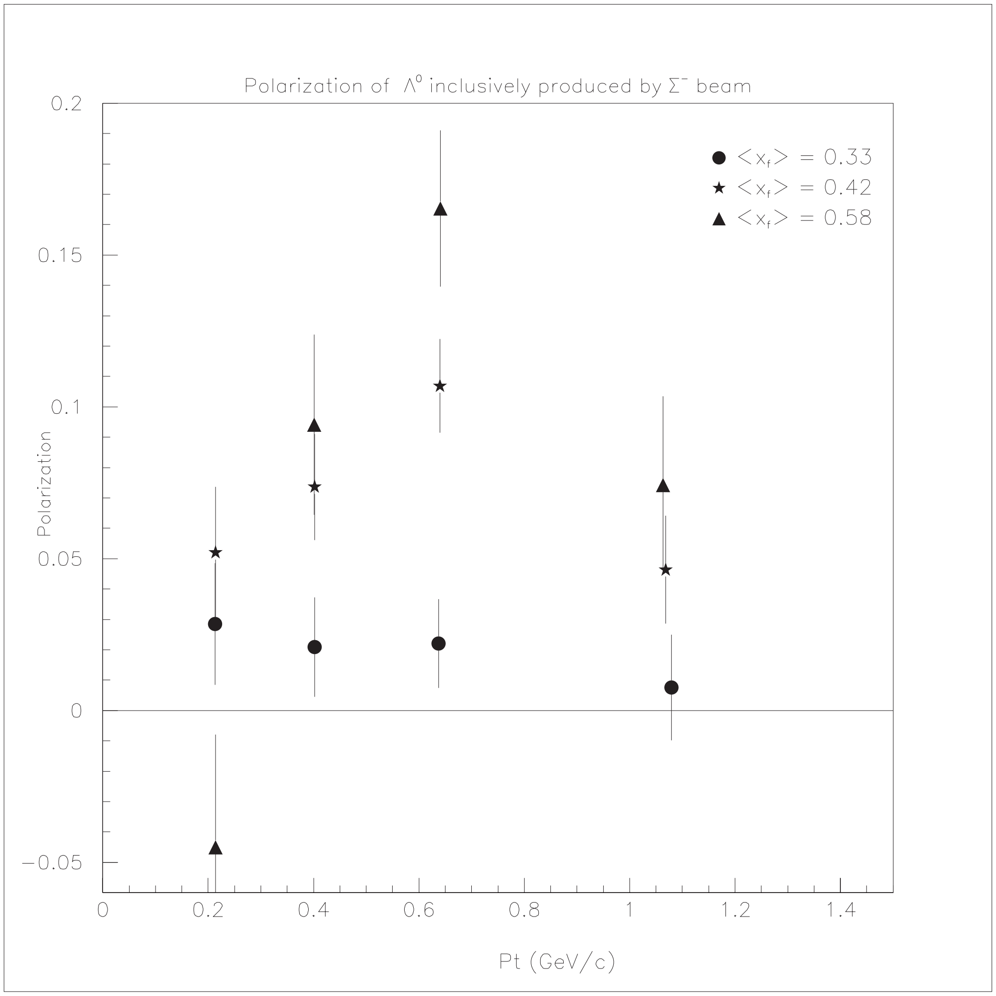

Figure 6.47: Polarization vs. p_t for all three x_f bins

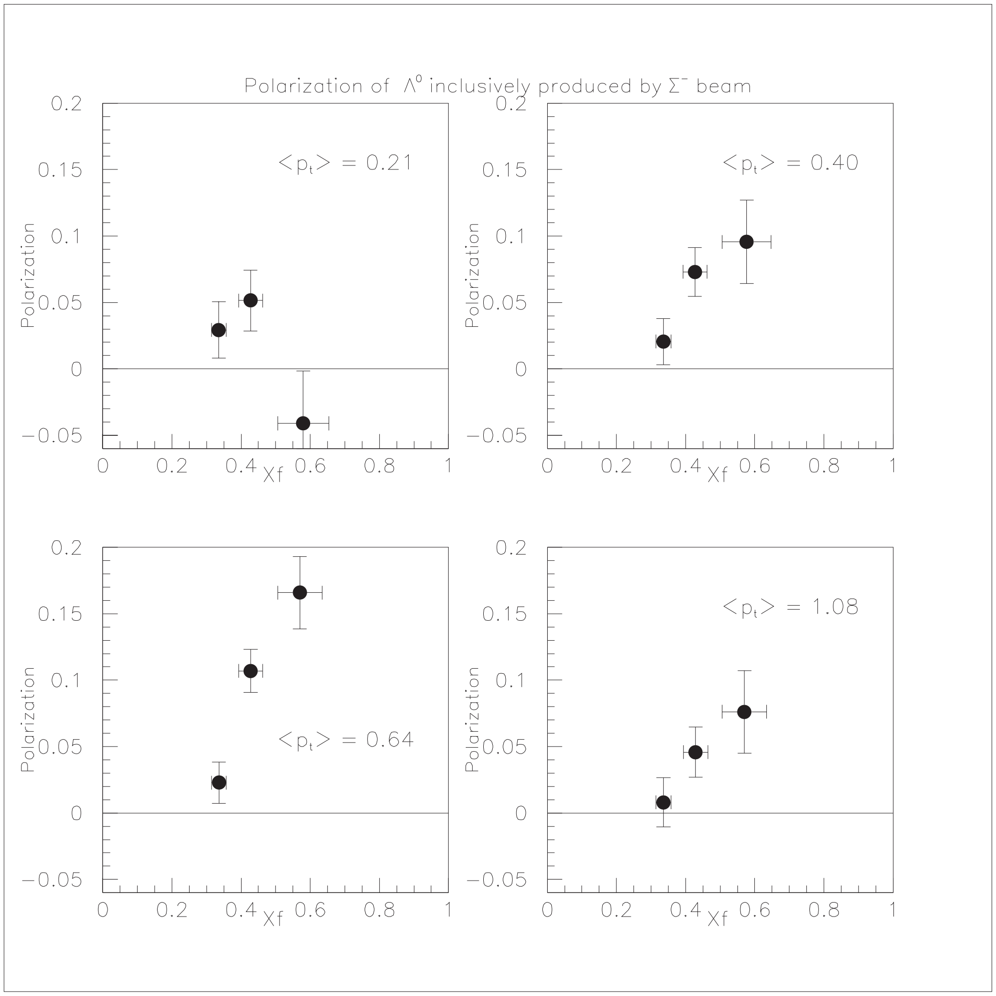

Figure 6.48: Polarization vs. x_f for all four p_t bins (geometric mean method)

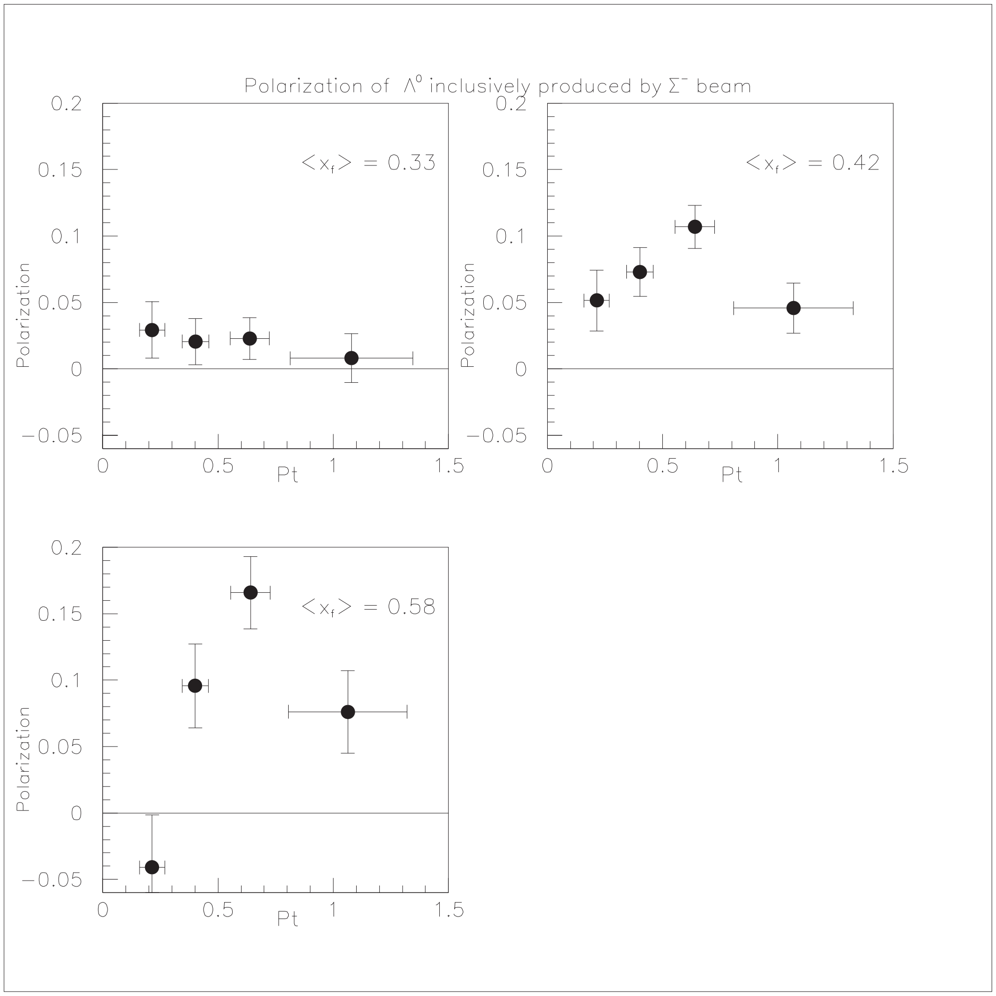

Figure 6.49: Polarization vs. p_t for all three x_f bins (geometric mean method)

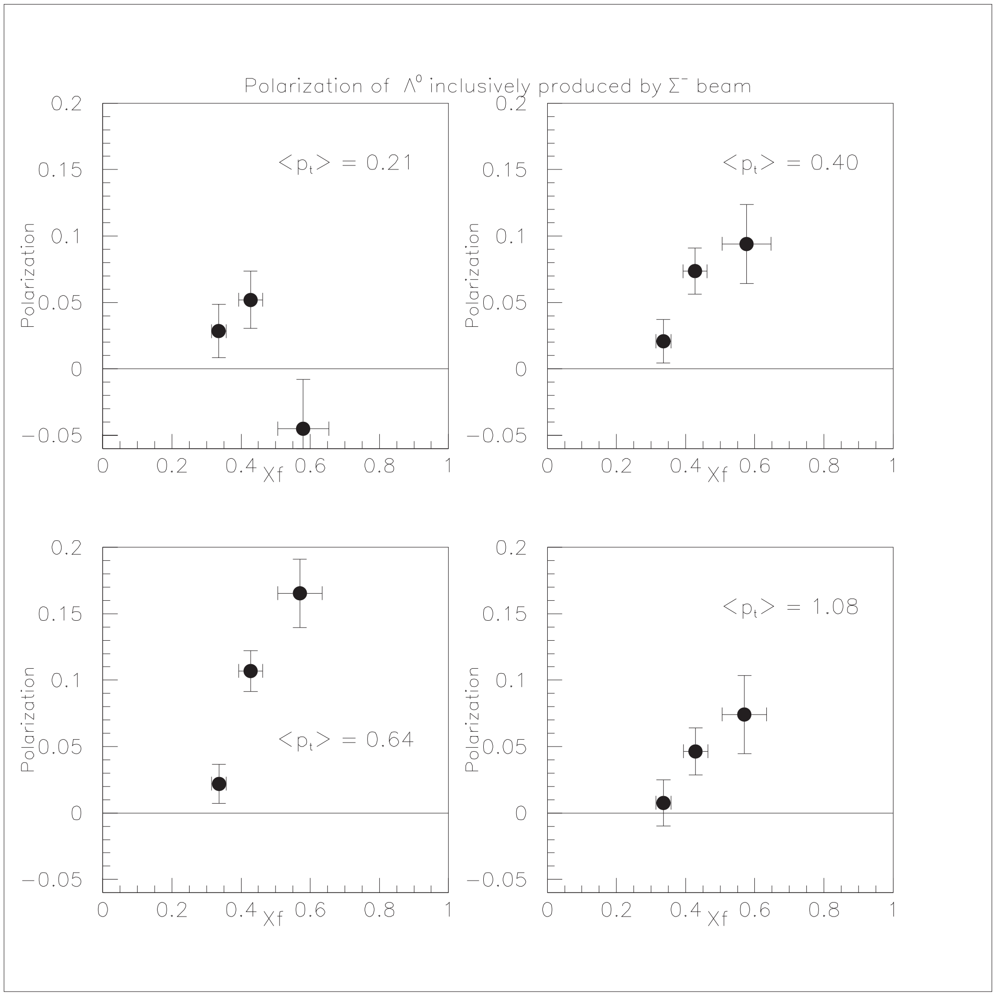

Figure 6.50: Polarization vs. x_f for all four p_t bins (arithmetic mean method)

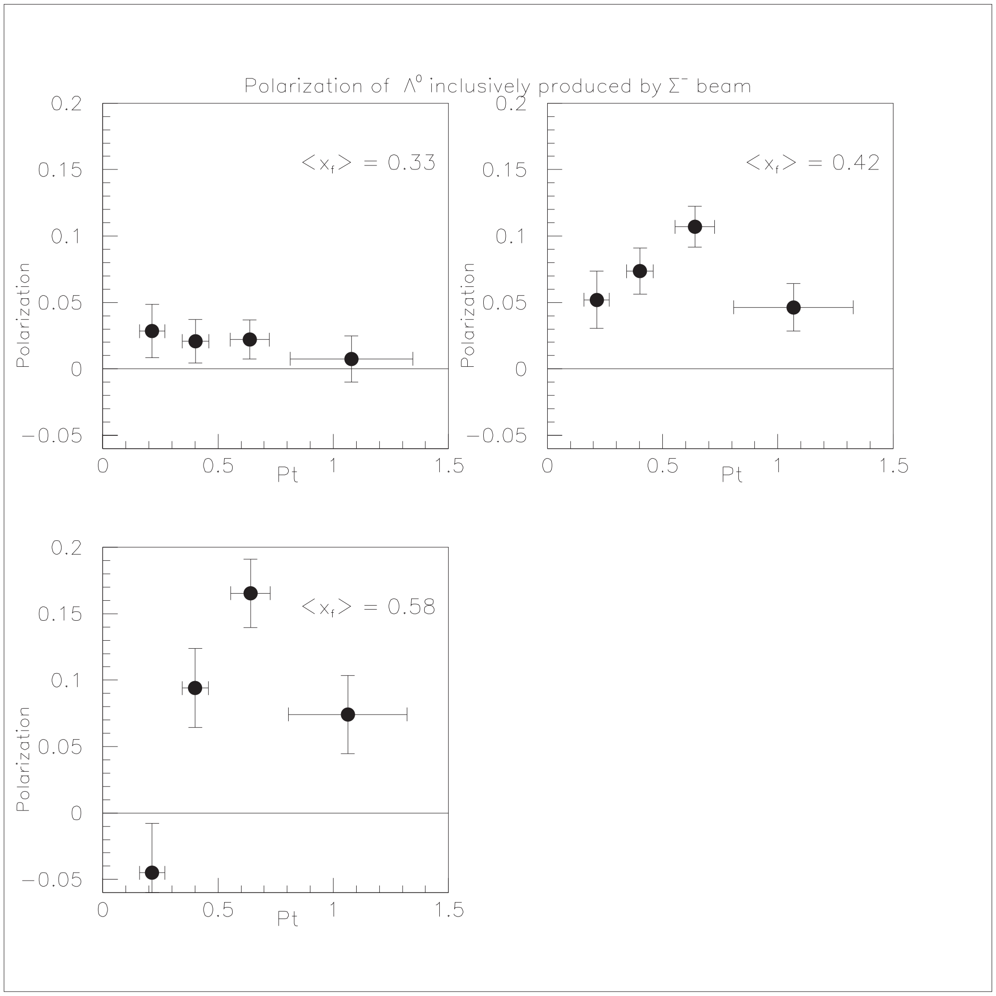

Figure 6.51: Polarization vs. p_t for each x_f bin (arithmetic mean method)

CHAPTER 7.

CONCLUSION

The results of this thesis show characteristics of the data which is common to the majority of hyperon polarization results previously published when the incident beam is a baryon. It shows:

- The polarization shows a strong linear dependence on x_f.
- The polarization shows a linear dependence on p_t up until around $p_t \geq 1.0$.
- The polarization has a maximum magnitude in the $10 - 20\%$ range.

This commonality in results is intriguing. It suggests that the mechanism for the polarizations magnitude may only depend weakly on the quark content of the incident beam. If not, the polarization produced by hyperon beams would probably be considerably different from that produced by protons. However, when comparing π^- produced $\Lambda's$ $(P \approx -5\%)$ with K^- produced $\Lambda's$ $(P \approx 40\%)$ the quark content seems very important. Maybe the effect is masked (or mitigated) by the inclusion of a third valence quark? The current models are unable account for these differences.

The DGM model assumes that the two valence quarks (sd) form a diquark before combining with the up-quark to form the Λ^0. As such, the expected polarization is mainly due to the addition of the up quark and is therefore predicted to be small and negative. If at this energy, this is not the case, and instead the s quark is the only valence quark transferred to the Λ^0, than the polarization would be expected to be similar to that induced by K^- beams. This is in fact the case, although at a lower magnitude than in the K-short case. This might also explain the difference between the results of WA89 and this analysis. The energy dependence may manifest itself in whether the s and d quarks form a diquark or if the s quark is the only valence quark in the process and both u and d quarks originate from the sea. Clearly, new models will need to be developed. The current level of experimental data should also be increased. Additional data, using hyperon beams will be a good test of these new models. The addition of other hyperon beam types could only increase the understanding of the phenomena of polarization.

APPENDIX A.

BIAS CANCELING METHODS

A.1 Overview

Bias canceling methods are used to extract the asymmetry ($\vec{A}$) and hence the polarization ($\vec{P}$) from experimental data. These methods are used to reduce biases in the result from variations in the apparatus acceptance function. In E781, these techniques were used to extract the polarization for Λ^0 from the data. This appendix describes the analysis technique used, looks at the first order variations for two ratio methods and compares these results on a subset of the data.

A.2 Preliminaries

For a two-body decay, (e.g. $\Lambda^0 \rightarrow p + \pi^-$), the angular distribution of the daughter baryon in the hyperon center of momentum (CM) frame is given by:

$$\frac{dN}{d\Omega} = a(\Omega) N_0 \frac{1}{4\pi}(1 + \vec{A} \cdot \hat{p}_b) \tag{A.1}$$

Where:

- $a(\Omega)$ is the apparatus acceptance function
- $\vec{A}$ is the asymmetry defines as $\vec{A} = \alpha\vec{P}$, where $\vec{P}$ is the hyperon polarization vector and α is the asymmetry parameter.
- $\hat{p}_b$ is the unit momentum vector of the daughter baryon in the hyperon CM frame.

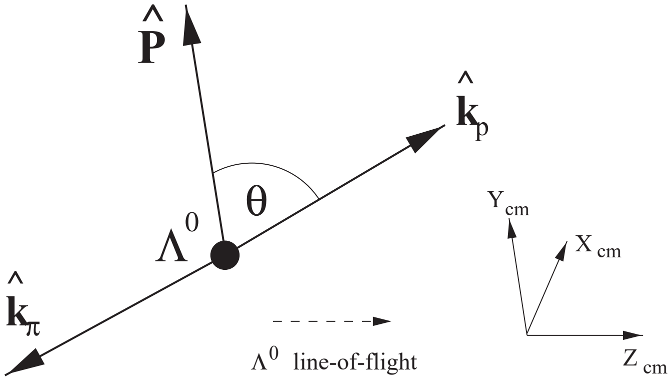

Figure A.1: Definition of θ, Center of Momentum frame

- N_0 is the total number of events in the sample.

This equation can be simplified by defining θ as the polar angle as measured from the asymmetry $\vec{A}$ in the CM frame (Fig A.1). Upon integration over the azimuthal angle, this distribution becomes:

$$\frac{dN}{d\cos\theta} = a(\cos\theta) N_0 \frac{1}{2}(1 + \alpha P \cos\theta) \tag{A.2}$$

The distribution of events is now dependent only on the angle between the spin vector of the parent hyperon ($\vec{S}$) and the momentum vector of the daughter baryon $\vec{k}_p$.

The asymmetry vector $\vec{A}$ lies in the direction of the spin axis $\vec{S}$ of the parent hyperon. For hyperons produced via a strong interaction, this direction must be perpendicular to the production plane due to parity conservation. In many experiments, this direction is determined by the experimental setup which predetermines the general direction of the spin vector. In other experiments, the hyperon beam is not incident on the production target at a fixed angle and hence the production plane may have any orientation in the CM frame. The direction of the spin vector is determined by the cross product of the hyperon momentum with the daughter baryon momentum (Fig. A.2).

In order for these bias canceling methods to be effective, it is necessary that the apparatus acceptance function for measurements with the spin vector up must be related to the apparatus acceptance function for measurements with the spin vector down. The relation between the two must be:

$$a_{down}(-\cos\theta) = a_{up}(\cos\theta) \tag{A.3}$$

That is, in terms of angles:

$$a_{down}(\theta_{down}) = a_{up}(\theta_{up}) \tag{A.4}$$

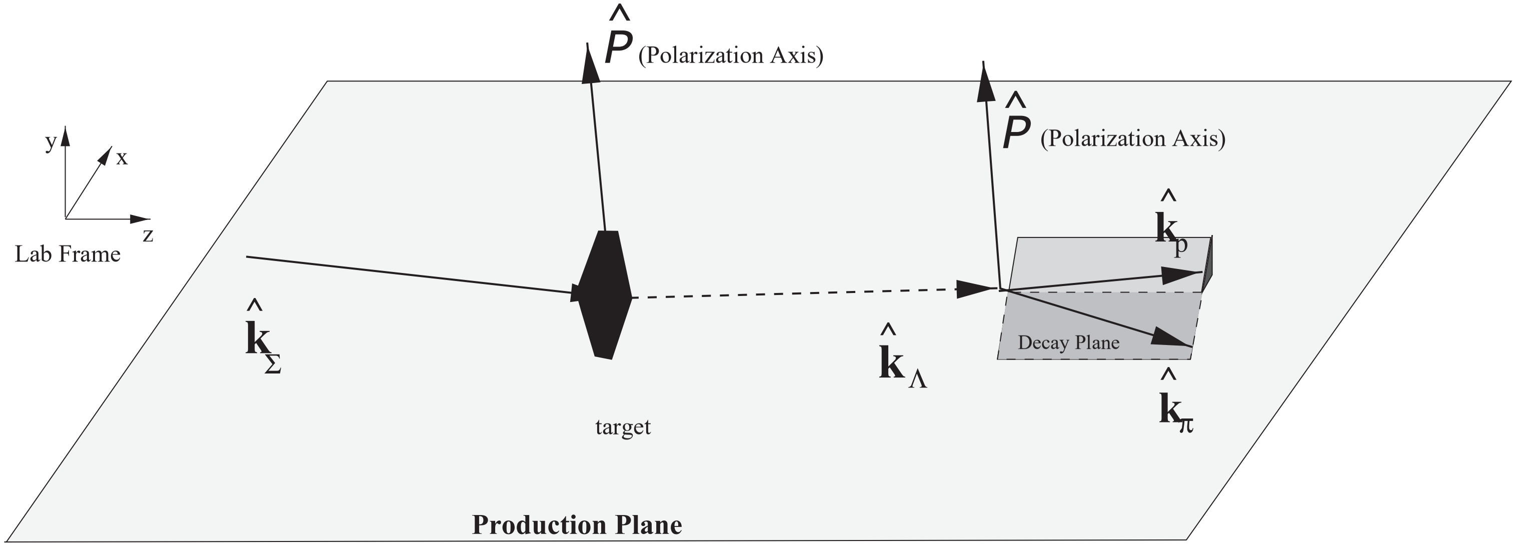

Figure A.2: Polarization vector definition: $\vec{S} = \vec{P}_{\Sigma^-} \times \vec{P}_{\Lambda^0}$

When

$$\theta_{down} = 180^0 - \theta_{up} \tag{A.5}$$

For experimental apparatus which exhibit a left-right or up-down symmetry, this can be accomplished by dividing space into azimuthal sectors such that each sector has a corresponding sector of similarly acceptance reflected through the plane of symmetry Fig. A.3.

A.3 Removing Experimental Biases

Given that the apparatus exhibits some type of up-down symmetry, it becomes possible to eliminate biases (false asymmetries) induced by acceptance differences in the measurement of polarization using two techniques; The arithmetic mean and the geometric mean bias canceling techniques. Both techniques will be analyzed for their abilities to remove first order variations in both the acceptance function and the polarization.

First, it is necessary to define four functions to simplify the analysis

$$U(\cos\theta_{up}) = \frac{N_0}{2} A_{up}(\cos\theta_{up})(1 + \alpha P_{up}\cos\theta_{up}) \tag{A.6}$$

$$U(-\cos\theta_{up}) = \frac{N_0}{2} A_{up}(\cos -\theta_{up})(1 - \alpha P_{up}\cos\theta_{up}) \tag{A.7}$$

$$D(\cos\theta_{down}) = \frac{N_0}{2} A_{down}(\cos\theta_{down})(1 + \alpha P_{down}\cos\theta_{down}) \tag{A.8}$$

$$D(-\cos\theta_{down}) = \frac{N_0}{2} A_{down}(\cos -\theta_{down})(1 - \alpha P_{down}\cos\theta_{down}) \tag{A.9}$$

with

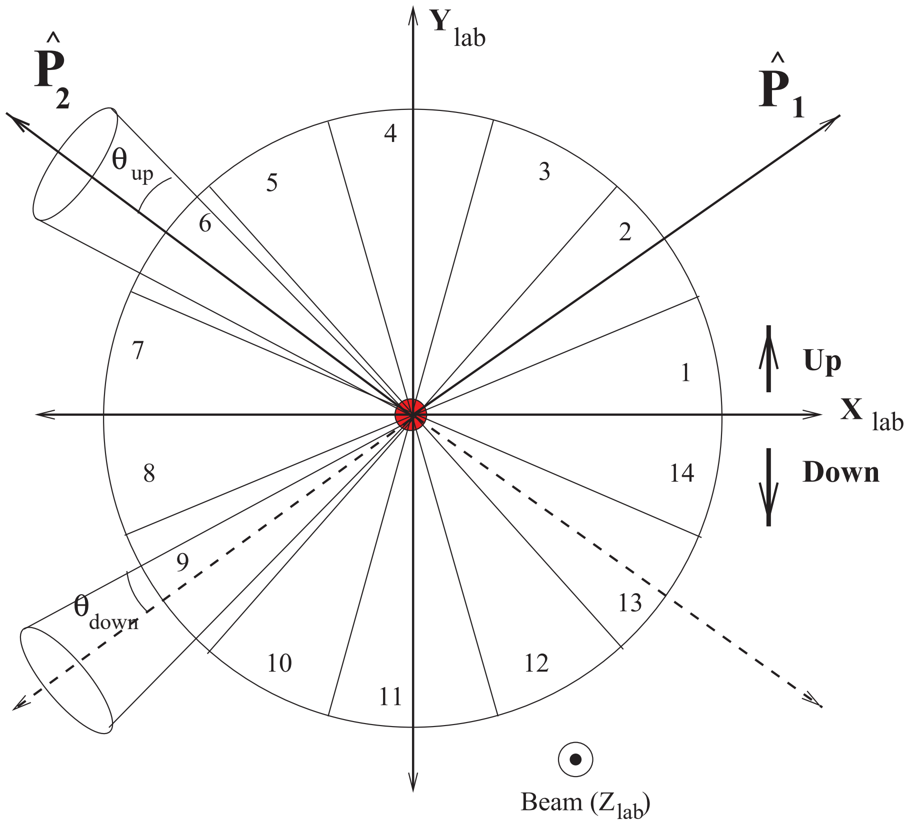

Figure A.3: Division of the decay space into azimuthal sectors

$$0 \leq \cos(\theta_{up}) \leq 1 \tag{A.10}$$

$$0 \leq \cos(\theta_{down}) \leq 1 \tag{A.11}$$

From Fig. A.3, it is clear that

$$A_{up}(\cos\theta_{up}) = A_{down}(\cos\theta_{down}) \tag{A.12}$$

When

$$\theta_{down} = 180^0 - \theta_{up} = \theta \tag{A.13}$$

Putting everything in terms of $\cos\theta$ yields:

$$A_{up}(\cos\theta) = A_{down}(-\cos\theta) \tag{A.14}$$

$$A_{up}(-\cos\theta) = A_{down}(\cos\theta) \tag{A.15}$$

Now look at first order variations in these functions. Careful attention must be payed to the sign of the variations since all equations are now in terms of θ.

$$A_{up}(\cos\theta) = A \Rightarrow A + \Delta A \tag{A.16}$$

$$A_{down}(-\cos\theta) = A \Rightarrow A - \Delta A \tag{A.17}$$

$$A_{up}(-\cos\theta) = B \Rightarrow B - \Delta B \tag{A.18}$$

$$A_{down}(\cos\theta) = B \Rightarrow B + \Delta B \tag{A.19}$$

Putting these back into the equations yields

$$U(\cos\theta) = \frac{N_0}{2}(A+\Delta A)(1+\alpha P_{up}\cos\theta) \tag{A.20}$$

$$U(-\cos\theta) = \frac{N_0}{2}(B-\Delta B)(1-\alpha P_{up}\cos\theta) \tag{A.21}$$

$$D(\cos\theta) = \frac{N_0}{2}(A-\Delta A)(1+\alpha P_{down}\cos\theta) \tag{A.22}$$

$$D(-\cos\theta) = \frac{N_0}{2}(B+\Delta B)(1-\alpha P_{down}\cos\theta) \tag{A.23}$$

Similarly, the polarization can be given a first order variation. This would correspond to measured polarization varying as a function of the direction of the spin vector $\vec{S}$. The polarization, as measured using the common angle θ, will be opposite in sign for a downward pointing spin vector $\vec{S}_{down}$, as opposed to $\vec{S}_{up}$. Similarly, the variation in the polarization will carry an opposite sign. That is

$$P_{up} = P \Rightarrow P + \Delta P \tag{A.24}$$

$$P_{down} = -P \Rightarrow -P - \Delta P \tag{A.25}$$

Which when put back into the equations yields:

$$U(\cos\theta) = \frac{N_0}{2}(A+\Delta A)(1+\alpha(P+\Delta P)\cos\theta) \tag{A.26}$$

$$U(-\cos\theta) = \frac{N_0}{2}(B-\Delta B)(1-\alpha(P+\Delta P)\cos\theta) \tag{A.27}$$

$$D(\cos\theta) = \frac{N_0}{2}(A-\Delta A)(1-\alpha(P-\Delta P)\cos\theta) \tag{A.28}$$

$$D(-\cos\theta) = \frac{N_0}{2}(B+\Delta B)(1+\alpha(P-\Delta P)\cos\theta) \tag{A.29}$$

Now the two techniques can be analyzed.

A.3.1 Arithmetic Mean

The arithmetic mean method is based on the following ratio:

$$\epsilon = \frac{U(\cos\theta) + D(-\cos\theta) - U(-\cos\theta) - D(\cos\theta)}{U(\cos\theta) + D(-\cos\theta) + U(-\cos\theta) + D(\cos\theta)} = \alpha P \cos\theta \qquad \text{(A.30)}$$

For experimental data, the functions $U(\cos\theta)$ and $D(\cos\theta)$ are numerical (i.e. histograms of the distribution $\frac{dN}{d\cos\theta}$). Hence, $\cos\theta$ is a discrete variable which can be written $z_i = \cos\theta_i$, and the ratio becomes:

$$\epsilon_i = \frac{U(z_i) + D(-z_i) - U(-z_i) - D(z_i)}{U(z_i) + D(-z_i) + U(-z_i) + D(z_i)} = \alpha P z_i \qquad \text{(A.31)}$$

Substituting in the expressions for the variations gives

$$\Big[\frac{N_0}{2}(A+\Delta A)(1+\alpha(P+\Delta P)z_i) + \frac{N_0}{2}(B+\Delta B)(1+\alpha(P-\Delta P)z_i) - \frac{N_0}{2}(B-\Delta B)(1-\alpha(P+\Delta P)z_i) - \frac{N_0}{2}(A-\Delta A)(1-\alpha(P-\Delta P)z_i)\Big] / \Big[\frac{N_0}{2}(A+\Delta A)(1+\alpha(P+\Delta P)z_i) + \frac{N_0}{2}(B+\Delta B)(1+\alpha(P-\Delta P)z_i) + \frac{N_0}{2}(B-\Delta B)(1-\alpha(P+\Delta P)z_i) + \frac{N_0}{2}(A-\Delta A)(1-\alpha(P-\Delta P)z_i)\Big] \qquad \text{(A.32)}$$

Expanding the terms, and some algebra gives:

$$= \frac{(\alpha P z_i) + \frac{\Delta A + \Delta B}{A+B}(1 + \alpha\Delta P z_i)}{1 + \alpha\Delta P z_i + \frac{\Delta A + \Delta B}{A+B}(\alpha P z_i)} \qquad \text{(A.33)}$$

Removing the second order terms in ΔA and ΔP gives:

$$= \frac{(\alpha P z_i) + \frac{\Delta A + \Delta B}{A+B}}{1 + \alpha z_i(\Delta P + \frac{\Delta A + \Delta B}{A+B} P)} \tag{A.34}$$

$$= \alpha P z_i + \frac{\Delta A + \Delta B}{A+B} - \alpha^2 z_i^2 (\Delta P P - P^2 \frac{\Delta A + \Delta B}{A+B}) + H.O.T. \tag{A.35}$$

the higher order terms are again dropped. Now look at the quadratic term. Since $\alpha = 0.642$, $P \approx 0.05$, $\frac{\Delta P}{P} \approx 0.1$, and $z_i \leq 1.0$ then

$$\alpha^2 z_i^2 (\Delta P P - P^2 \frac{\Delta A + \Delta B}{A+B}) < 2 \times 10^{-4} \tag{A.36}$$

and the ratio of the quadratic term to the linear term is ≈ 0.006, so it can be dropped. That gives, to first order,

$$\boxed{\epsilon_i \doteq \alpha P z_i + \frac{\Delta A + \Delta B}{A+B}} \tag{A.37}$$

If the acceptance is a slowly varying function, then its' affect on the measurement will be minimal. Note that all first order variations in the polarization have canceled out with this method.

A.3.2 Error Propagation

The problem of finding the asymmetry and hence, the polarization can now be done using the arithmetic ratio. But, this ratio is taken on a sector in azimuth space and a range in $\cos\theta$ space. Both of these increment sizes are selectable and care must be taken to ensure systematic errors in bin sizing are properly accounted for. However, once a bin size has been chosen it is still necessary to propagate the counting error from the N's into the error in

ϵ. First the fit is done over the $\cos\theta$ bins and then over the azimuth bins. The fit is made through χ^2 minimization. For the fit over the $\cos\theta$ bins, χ^2 is defined as:

$$\chi^2 = \sum_{ij}(Az_i - \epsilon_i)W_{ij}(Az_j - \epsilon_j) \tag{A.38}$$

where W is the inverse of the covariance matrix: $W_{ij} = [\sigma^2_{ij}]^{-1}$.

The covariance matrix is:

$$\sigma^2_{ij} =< \Delta\epsilon_i \Delta\epsilon_j > \tag{A.39}$$

where $\Delta\epsilon_i$ can be written as:

$$\Delta\epsilon_i = \sum_j \frac{\partial\epsilon_i}{\partial N_j}\Delta N_j \tag{A.40}$$

Solving for σ^2_{ij} in terms of the measured parameters gives:

$$\sigma^2_{ij} = \frac{(1-\epsilon_i^2)(1-\epsilon_j^2)}{4}\left[\delta_{ij}\left(\frac{1}{N_i^{up}} + \frac{1}{N_i^{down}}\right) - \left(\frac{1}{N_0^{up}} + \frac{1}{N_0^{down}}\right)\right] \tag{A.41}$$

Since the covariance matrix is symmetric, its inverse is also. Minimizing the χ^2 for the asymmetry parameter A gives:

$$A = \frac{\sum_{ij} z_i W_{ij} \epsilon_j}{\sum_{ij} z_i W_{ij} z_j} \tag{A.42}$$

and the error in the asymmetry is:

$$\sigma_A = \sqrt{\frac{1}{\sum_{ij} z_i W_{ij} z_j}} \tag{A.43}$$

This gives the asymmetry measurement for a given azimuthal sector. Each sector's measurement needs to be combined to yield a final result. This is again done through χ^2 minimization with the result being a weighted sum:

$$A = \frac{\sum_{ij} A_i W_{ij}}{\sum_{ij} W_{ij}} \tag{A.44}$$

with error:

$$\sigma_A = \sqrt{\frac{1}{\sum_{ij} W_{ij}}} \tag{A.45}$$

The other technique used to cancel biases is the geometric mean method.

A.3.3 Geometric Mean

The geometric mean is based on the following ratio:

$$\epsilon_i = \frac{\sqrt{U(z_i) \times D(-z_i)} - \sqrt{U(-z_i) \times D(z_i)}}{\sqrt{U(z_i) \times D(-z_i)} + \sqrt{U(-z_i) \times D(z_i)}} = \alpha P z_i \tag{A.46}$$

Substituting in the expressions for the variations gives

$$\begin{aligned}
&\Bigg[\sqrt{\frac{N_0}{2}(A+\Delta A)(1+\alpha(P+\Delta P)z_i) \times \frac{N_0}{2}(B+\Delta B)(1+\alpha(P-\Delta P)z_i)} - \\
&\sqrt{\frac{N_0}{2}(B-\Delta B)(1-\alpha(P+\Delta P)z_i) \times \frac{N_0}{2}(A-\Delta A)(1-\alpha(P-\Delta P)z_i)}\Bigg] / \\
&\Bigg[\sqrt{\frac{N_0}{2}(A+\Delta A)(1+\alpha(P+\Delta P)z_i) \times \frac{N_0}{2}(B+\Delta B)(1+\alpha(P-\Delta P)z_i)} + \\
&\sqrt{\frac{N_0}{2}(B-\Delta B)(1-\alpha(P+\Delta P)z_i) \times \frac{N_0}{2}(A-\Delta A)(1-\alpha(P-\Delta P)z_i)}\Bigg]
\end{aligned} \tag{A.47}$$

Expanding the terms, and some algebra gives:

$$\begin{aligned}&\Bigg[(1+\alpha P)\sqrt{1+\frac{\Delta B}{B}+\frac{\Delta A}{A}+\frac{\Delta B\Delta A}{AB}}-\\&\qquad(1-\alpha P)\sqrt{1-\frac{\Delta B}{B}-\frac{\Delta A}{A}+\frac{\Delta B\Delta A}{AB}}\Bigg]/\\&\qquad\Bigg[(1+\alpha P)\sqrt{1+\frac{\Delta B}{B}+\frac{\Delta A}{A}+\frac{\Delta B\Delta A}{AB}}+\\&\qquad\qquad(1-\alpha P)\sqrt{1-\frac{\Delta B}{B}-\frac{\Delta A}{A}+\frac{\Delta B\Delta A}{AB}}\Bigg]\end{aligned}\tag{A.48}$$

Which becomes

$$\begin{aligned}&\Bigg[(1+\alpha P)1+\frac{1}{2}(\frac{\Delta B}{B}+\frac{\Delta A}{A})+\frac{1}{2}(\frac{\Delta B\Delta A}{AB})-\\&\qquad(1-\alpha P)1-\frac{1}{2}(\frac{\Delta B}{B}+\frac{\Delta A}{A})+\frac{1}{2}(\frac{\Delta B\Delta A}{AB})\Bigg]/\\&\qquad\Bigg[(1+\alpha P)1+\frac{1}{2}(\frac{\Delta B}{B}+\frac{\Delta A}{A})+\frac{1}{2}(\frac{\Delta B\Delta A}{AB})+\\&\qquad\qquad(1-\alpha P)1-\frac{1}{2}(\frac{\Delta B}{B}+\frac{\Delta A}{A})+\frac{1}{2}(\frac{\Delta B\Delta A}{AB})\Bigg]\end{aligned}\tag{A.49}$$

Removing the second order terms in ΔA and ΔP gives:

$$\epsilon_i=\frac{\alpha Pz_i+\frac{1}{2}(\frac{\Delta A}{A}+\frac{\Delta B}{B})}{1+\frac{1}{2}\alpha Pz_i(\frac{\Delta A}{A}+\frac{\Delta B}{B})}\tag{A.50}$$

Which can be expanded to:

$$\epsilon_i=\alpha Pz_i+\frac{1}{2}(\frac{\Delta A}{A}+\frac{\Delta B}{B})-\frac{1}{2}\alpha^2P^2z_i^2(\frac{\Delta A}{A}+\frac{\Delta B}{B})+H.O.T\tag{A.51}$$

As before, the quadratic term is small and can be dropped along with the higher order terms, giving to first order:

$$\boxed{\epsilon_i \doteq \alpha P z_i + \frac{1}{2}\left(\frac{\Delta A + \Delta B}{A+B}\right)} \tag{A.52}$$

A.3.4 Error Propagation

As with the arithmetic ratio the data must be fit over the $\cos\theta$ bins and then over the azimuth bins. The fit is made through χ^2 minimization. For the fit over the $\cos\theta$ bins, χ^2 is again defined as:

$$\chi^2 = \sum_{ij}(Az_i - \epsilon_i)W_{ij}(Az_j - \epsilon_j) \tag{A.53}$$

In this case, the covariance matrix has the form:

$$\sigma_{ij}^2 = \frac{\left(1-\epsilon_i^2\right)^2}{4}\,\delta_{ij}\left(\frac{1}{N_i^{up+}} + \frac{1}{N_i^{down-}} + \frac{1}{N_i^{up-}} + \frac{1}{N_i^{down+}}\right) \tag{A.54}$$

Since the covariance matrix is symmetric, its inverse is also. Minimizing the χ^2 for the asymmetry parameter A gives:

$$A = \frac{\sum_{ij} z_i W_{ij} \epsilon_j}{\sum_{ij} z_i W_{ij} z_j} \tag{A.55}$$

and the error in the asymmetry is:

$$\sigma_A = \sqrt{\frac{1}{\sum_{ij} z_i W_{ij} z_j}} \tag{A.56}$$

This gives the asymmetry measurement for a given azimuthal sector. Each sector's measurement needs to be combined to yield a final result. This is again done through χ^2 minimization with the result being a weighted sum:

$$A = \frac{\sum_{ij} A_i W_{ij}}{\sum_{ij} W_{ij}} \tag{A.57}$$

with error:

$$\sigma_A = \sqrt{\frac{1}{\sum_{ij} W_{ij}}} \tag{A.58}$$

A.4 Comparison of the Two Ratio Methods

Both methods show similar first order variations, with the Geometric Mean variations $\frac{1}{2}$ of the Arithmetic Mean. However, the Geometric Method requires slightly larger data sets to achieve the same error found in the Arithmetic method. Is there a difference?

In Table A.1 and Table A.2, the results from the two methods, shows that the two methods agree with each other closely. The Arithmetic Mean method gives slightly smaller errors in the final values. Both methods were used on the same ntuple of data consisting of over $350,000$ events. The two methods agree very closely with each other for measurements using a large number of events. When the events become very sparse, however, they become unstable and the geometric mean method is unable to converge on a value.

Table A.1: Polarization Results (Arithmetic Mean method)

		$X_f Bin$		
		$0.3 - 0.375$	$0.375 - 0.5$	$0.5 - 1.0$
$P_t Bin$	$< P_t >$	$< X_f >$		
(GeV/c)	(GeV/c)	0.34	0.43	0.58
$0.1 - 0.3$	0.21	0.028 ± 0.020	0.052 ± 0.022	-0.045 ± 0.037
$0.3 - 0.5$	0.40	0.021 ± 0.016	0.074 ± 0.017	0.094 ± 0.030
$0.5 - 0.8$	0.64	0.022 ± 0.015	0.107 ± 0.015	0.165 ± 0.026
> 0.8	1.07	0.008 ± 0.017	0.046 ± 0.018	0.074 ± 0.029

Table A.2: Polarization Results (Geometric Mean method)

		$X_f Bin$		
		$0.3 - 0.375$	$0.375 - 0.5$	$0.5 - 1.0$
$P_t Bin$	$< P_t >$	$< X_f >$		
(GeV/c)	(GeV/c)	0.34	0.43	0.58
$0.1 - 0.3$	0.21	0.029 ± 0.021	0.052 ± 0.023	-0.041 ± 0.040
$0.3 - 0.5$	0.40	0.021 ± 0.017	0.073 ± 0.018	0.096 ± 0.031
$0.5 - 0.8$	0.64	0.023 ± 0.016	0.107 ± 0.016	0.165 ± 0.027
> 0.8	1.07	0.008 ± 0.018	0.046 ± 0.019	0.076 ± 0.031

APPENDIX B.

BSSD ALIGNMENT

B.1 System Description

The E781 Beam Silicon Detector system consists of 8 detector planes, organized into 3 groups of which two groups consist of 3 planes and one group consists of 2 planes. Each group of planes is mounted onto a machined Al alignment plate, called a "monument block". This alignment plate orients each detector precisely with respect to its neighbors and transfers that alignment to the E781 laboratory system via the polished granite support block. The overall layout of the beam silicon system is shown in Figure B.1 and the detail of one monument block is shown in Figure B.2.

B.2 Procedure

The alignment procedure was carried out on a CORDAX Coordinate Measuring Machine (CMM) at Lab D, with the operational assistance of Mike Roman. The measurement precision on the machine was about 1μ in each of the three orthogonal directions.

Each monument block has a set of carbide "buttons". The two buttons on the bottom rest on the surface of the granite table and the third one butts against a steel brace perpendicular to the granite surface. The origin is defined as the intersection of the granite blocks. All positions of detector strips are given with respect to this origin.

To align the detectors, a precise(to within 200μrad) right angle was set up using granite blocks clamped to the CMM table. The granite blocks were at worst, shifted 60μ in 30cm, i.e. a 0.2mrad offset from 90 ^{o} . In 2 cm, this results in an offset error of 4μ in the position of the origin. The CMM recorded the orientations of the “X” and “Y” lines and formed the origin. As this was done in software, it was possible to rotate the axes about the origin, necessary in order to align the “U” detectors. The monument block was slid and pushed into place with the first detector mounted on the top face of the block. In the case of the 3-plane blocks, the first detector is a “U” plane. For this, the axes are rotated in software 45 ^{o} . before aligning the detector. In the case of the 2-plane block, no rotation is required. The alignment of a detector strip parallel to an axis of the detector, was checked. This consisted of observing an edge strip of the detector and adjusting the detector orientation(by loosening one end support at at time)so that the run-out along its length was $<2\mu$. After this was completed, the four corners on the active area of the detector were measured and recorded. Once a detector was aligned and fixed in place, a second detector was mounted and the alignment procedure repeated. In the case of the 3-plane detectors, the axes were rotated back 45^o before continuing. Once the second detector was aligned the third detector was mounted and the procedure repeated. This completed the alignment of one monument block. The angular precision of each detector is +-1 μrad.

B.3 Hardware Alignment Data

Every silicon panel in the beam detector has been surveyed at all four corners of the active detector area. Figure B.3 shows the locations which were surveyed and measured, and figure B.4 shows the reference axes for the

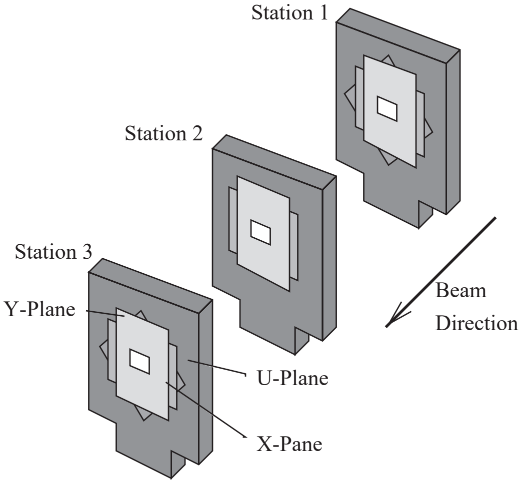

Figure B.1: BSSD layout

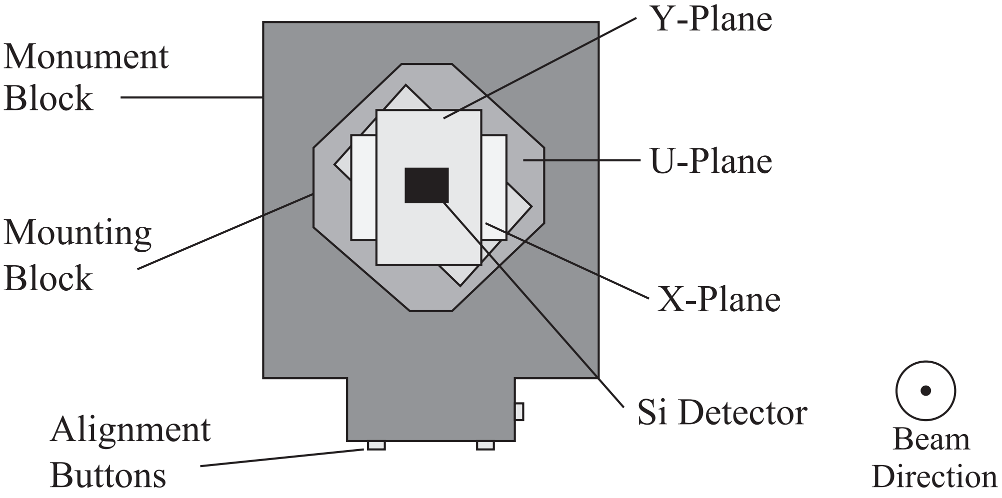

Figure B.2: Monument Block

measurement. The position of each measurment is the end of the outside strips, at the center of the strip. The “Z” position measures the variation of the mounted detector from the reference “X”-”Y” plane defined by the monument block. The “X” and “Y” positions are useful in calculating the tilt of the detector strips from the reference “X” or ”Y” axis. Table B.1 describes the x, y and z positions of each of the four corners for each detector. Note that the origin used for these measurements is different for station 3 (see item below).

All detectors are mounted on the downstream face of the monument blocks. The U plane is farthest upstream followed by the Y and X planes

Table B.2 describes the z positions for the first reference point of the beam detector planes. The z origin for this table is the downstream face of station 1.

B.4 Important Points

- All measurements have been made with respect to **one fixed point** on the monument block (The intersection of lines formed by the fixed buttons), which is also the origin.
- The z position of each detector is very accurately known in relation to the monument block, and less accurately in realation to the experiment origin.
- The upstream outside face of the RF cage is **-57 mm** from the origin used for Table B.2. Also, the BSSD origin is **146.5 cm** upstream of the upstream face of the first VSSD monument block.
- BSSD Station 3 has the alignment button on the opposite side of the monument block compared to the other monument blocks. This was

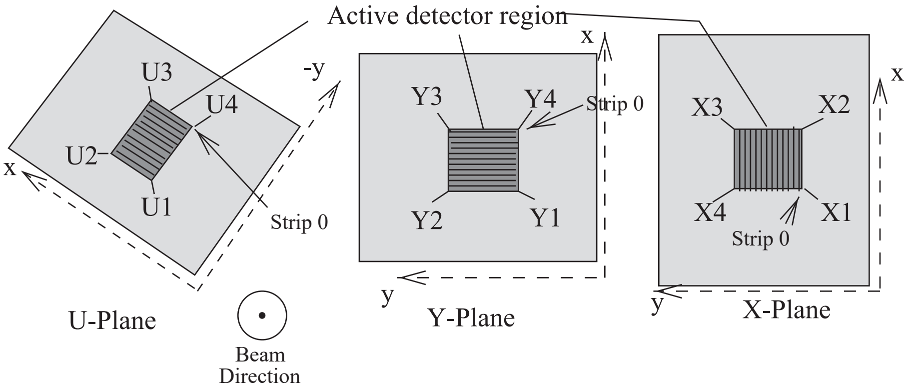

Figure B.3: Points surveyed on the detectors

necessary since the mounting holes for the detector were unusable on the nominal side of the mounting block.

- A reference point opposite of the origin on the monument block was measured and checked every time a detector was aligned. This was used to ensure the mounment block did not move during the alignment process.

Table B.1: Alignment reference points (in mm) on the Beam detectors

Detector	**Position**	**X**	**Y**	**Z**
BSSD_ST1_U	U1	291.295	-111.280	4.200
	U2	311.271	-111.281	4.255
	U3	311.277	-131.742	4.188
	U4	291.303	-131.740	4.178
BSSD_ST1_Y	Y1	288.237	117.322	26.262
	Y2	288.236	137.315	26.128
	Y3	308.691	137.320	26.252
	Y4	308.696	117.320	26.328
BSSD_ST1_X	X1	288.377	116.708	48.118
	X2	308.374	116.711	48.118
	X3	308.370	137.167	48.189
	X4	288.373	137.166	48.189
BSSD_ST2_Y	Y1	287.673	116.770	26.316
	Y2	287.672	136.777	26.374
	Y3	308.128	136.776	26.316
	Y4	308.131	116.771	26.316
BSSD_ST2_X	X1	288.234	117.522	48.112
	X2	308.234	117.523	48.128
	X3	308.223	137.982	48.112
	X4	288.233	137.982	48.095
BSSD_ST3_U	U1	111.773	-290.199	4.188
	U2	131.702	-290.202	4.124
	U3	131.725	-310.676	4.144
	U4	111.775	-310.673	4.199
BSSD_ST3_Y	Y1	288.469	-136 722	26.070
	Y2	288.471	-116.675	26.070
	Y3	308.962	-116.677	26.122
	Y4	308.964	-136.720	26.125
BSSD_ST3_X	X1	288.955	-137.149	48.025
	X2	308.994	-137.150	47.962
	X3	309.003	-116.667	47.961
	X4	288.942	-116 666	48.025

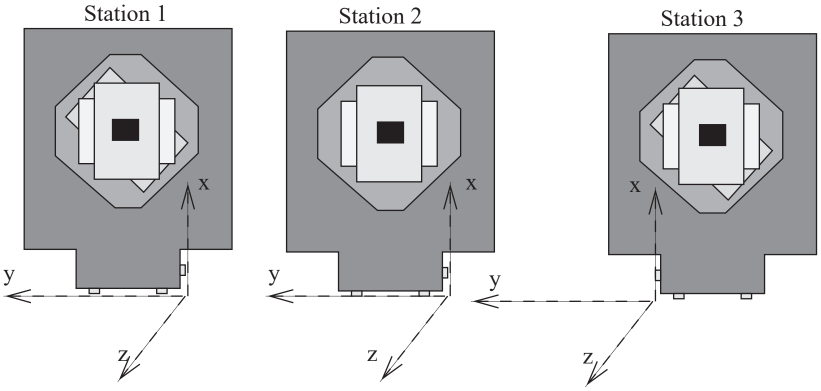

Figure B.4: Measurement axes of the detectors

Table B.2: Z position (in mm) of Beam Detector Planes

Detector	**z position**
BSSD_ST1_U	20.8
BSSD_ST1_Y	42.9
BSSD_ST1_X	64.7
BSSD_ST2_Y	644.8
BSSD_ST2_X	666.6
BSSD_ST3_U	1220.8
BSSD_ST3_Y	1242.7
BSSD_ST3_X	1264.4

APPENDIX C.
SELEX COLLABORATION LIST

The SELEX Collaboration

G.P. Thomas
Ball State University, Muncie, IN 47306, U.S.A.

E. Gülmez
Bogazici University, Bebek 80815 Istanbul, Turkey

R. Edelstein, E. Gottschalk[1], S.Y. Jun, A. Kushnirenko, D. Mao[2],
P. Mathew[3], M. Mattson, M. Procario, J. Russ, J. You
Carnegie-Mellon University, Pittsburgh, PA 15213, U.S.A.

A.M.F. Endler
Centro Brasiliero de Pesquisas Físicas, Rio de Janeiro, Brazil

P.S. Cooper, J. Engelfried[4], J. Kilmer, S. Kwan, J. Lach, G. Oleynik[2],
E. Ramberg, D. Skow, L. Stutte
Fermilab, Batavia, IL 60510, U.S.A.

Y.M. Goncharenko, O.A. Grachov[5], V.P. Kubarovsky, A.I. Kulyavtsev[6],
V.F. Kurshetsov, A.P. Kozhevnikov, L.G. Landsberg, V.V. Molchanov,

V.A. Mukhin, S.B. Nurushev, A.N. Vasiliev, D.V. Vavilov, V.A. Victorov
Institute for High Energy Physics, Protvino, Russia

Li Yunshan, Li Zhigang, Mao Chensheng, Zhao Wenheng, He Kangling,
Zheng Shuchen, Mao Zhenlin
Institute of High Energy Physics, Beijing, P.R. China

M.Y. Balatz, G.V. Davidenko, A.G. Dolgolenko, G.B. Dzyubenko,
A.V. Evdokimov, A.D. Kamenskii, M.A. Kubantsev, I. Larin, V. Matveev,
A.P. Nilov, V.A. Prutskoi, V.K. Semyatchkin, A.I. Sitnikov,
V.S. Verebryusov, V.E. Vishnyakov
Institute of Theoretical and Experimental Physics, Moscow, Russia

U. Dersch, I. Eschrich[7], K. Königsmann[8], I. Konorov[9], H. Krüger,
S. Masciocchi[10], B. Povh, J. Simon, K. Vorwalter[11]
Max-Planck-Institut für Kernphysik, 69117 Heidelberg, Germany

I.S. Filimonov[12], E.M. Leikin, A.V. Nemitkin, V.I. Rud
Moscow State University, Moscow, Russia

V.A. Andreev, A.G. Atamantchouk, N.F. Bondar, V.L. Golovtsov,
V.T. Kim, L.M. Kochenda, A.G. Krivshich, N.P. Kuropatkin, V.P. Maleev,
P.V. Neoustroev, S. Patrichev, B.V. Razmyslovich, V. Stepanov,
M. Svoiski, N.K. Terentyev[6], L.N. Uvarov, A.A. Vorobyov
Petersburg Nuclear Physics Institute, St. Petersburg, Russia

S. Gerzon, I. Giller, M.A. Moinester, A. Ocherashvili, V. Steiner
Tel Aviv University, 69978 Ramat Aviv, Israel

A. Morelos
Universidad Autónoma de San Luis Potosí, San Luis Potosí, Mexico

M. Luksys
Universidade Federal da Paraíba, Paraíba, Brazil

S.L. McKenna, V.J. Smith
University of Bristol, Bristol BS8 1TL, United Kingdom

N. Akchurin, M. Aykac, M. Kaya, D. Magarrel, E. McCliment,
K.D. Nelson, C. Newsom, Y. Onel, E. Ozel, S. Ozkorucuklu, P. Pogodin
University of Iowa, Iowa City, IA 52242, U.S.A.

L.J. Dauwe
University of Michigan-Flint, Flint, MI 48502, U.S.A.

M. Gaspero, M. Iori
University of Rome "La Sapienza" and INFN, Rome, Italy

L. Emediato, C. Escobar[13], F.G. Garcia, P. Gouffon, T. Lungov[14],
M. Srivastava, R. Zukanovich-Funchal
University of São Paulo, São Paulo, Brazil

A. Bravar, D. Dreossi, A. Lamberto, A. Penzo, G.F. Rapazzo, P. Schiavon
University of Trieste and INFN, Trieste, Italy

---

[1] Now at Fermilab, Batavia, IL 60510, U.S.A.

[2] Present address: Lucent Technologies, Naperville, IL

[3] Present address: Motorola Inc., Schaumburg, IL

[4] Now at Universidad Autónoma de San Luis Potosí, San Luis Potosí, Mexico

[5] Present address: Dept. of Physics, Wayne State University, Detroit, MI 48201

[6] Now at Carnegie-Mellon University, Pittsburgh, PA 15213, U.S.A.

[7] Now at Imperial College, London SW7 2BZ, U.K.

[8] Now at Universität Freiburg, 79104 Freiburg, Germany

[9] Now at Physik-Department, Technische Universität München, 85748 Garching, Germany

[10] Now at Max-Planck-Institut für Physik, München, Germany

[11] Present address: Deutsche Bank AG, 65760 Eschborn, Germany

[12] deceased

[13] Current Address: Instituto de Fisica da Universidade Estadual de Campinas, UNICAMP, SP, Brazil

[14] Current Address: Instituto de Fisica Teorica da Universidade Estadual Paulista, São Paulo, Brazil

REFERENCES

[1] G. Bunce, *et al.*, Phys. Rev. Lett. **36**, 1113, (1976)

[2] K. Heller, *et al.*, Phys. Lett. **68B**, 480, (1977)

[3] K. Heller, *et al.*, Phys. Rev. Lett. **41**, 607, (1978)

[4] S. Erhan, *et al.*, Phys. Lett. **82B**, 301, (1979)

[5] F. Lomanno, *et al.*, Phys. Rev. Lett. **43**, 1905, (1979)

[6] J. Bensinger, *et al.*, Phys. Rev. Lett. **50**, 313, (1983)

[7] B. Adeva, *et al.*, Z. Phys. **C26**, 359, (1984)

[8] N. N. Biswas, *et al.*, Nucl. Phys. **B167**, 41, (1980)

[9] F. Abe, *et al.*, Phys. Rev. Lett. **50**, 1102, (1983)

[10] S. A. Gourlay, *et al.*, Phys. Rev. Lett. **56**, 2244, (1986)

[11] T. A. Armstrong, *et al.*, Nucl. Phys. **B262**, 356, (1985)

[12] A. Borg, *et al.* Nouvo Cimento **22A**, 559, (1974)

[13] F. Abe, *et al.*, Phys. Rev. D **34**, 1950, (1986)

[14] A. M. Smith, *et al.*, Phys. Lett. B **185**, 209, (1987)

[15] B. Lundberg, *et al.*, Phys. Rev. D **40**, 3557, (1989)

[16] E. J. Ramberg, *et al.*, Phys. Lett. B **338**, 403 (1994).

[17] J. Felix, *et al.*, Phys. Rev. Lett. **76**, 22, (1996)

[18] V. Fanti, *et al.*, Eur. Phys. J. C **6**, 265, (1999)

[19] M. I. Adamovich, *et al.*, Z Phys. A **350**, 379, (1995)

[20] M. W. McNaughton, *et al.*, Phys. Rev. C **23**, 1128, (1981)

[21] P. T. Cox, *et al.*, Phys. Rev. Lett. **46**, 877, (1981)

[22] L. Deck, *et al.*, Phys. Rev. D **28**, 1, (1983)

[23] Y. W. Wah, *et al.*, Phys. Rev. Lett. **55**, 2551, (1985)

[24] R. Rameika, *et al.*, Phys. Rev. D **33**, 3172, (1986)

[25] C. Wilkinson, *et al.*, Phys. Rev. Lett. **58**, 855, (1987)

[26] E. C. Dukes, *et al.*, Phys. Lett. B **193**, 135, (1987)

[27] L. H. Trost, *et al.*, Phys. Rev. D **40**, 1703, (1989)

[28] B. E. Bonner, *et al.*, Phys. Rev. Lett. **62**, 1591, (1989)

[29] J. Duryea, *et al.*, Phys. Rev. Lett. **67**, 1193, (1991)

[30] A. Morelos, *et al.*, Phys. Rev. Lett. **71**, 2172, (1993)

[31] J. Lach, Conference Proceedings, "Flavour and Spin in hadronic and Elecctromagnetic Interactions", Balogna, (1993)

[32] L. Pondrom, Phys. Rep. **122**, 58, (1985)

[33] P. M. Ho, *et al.*, Phys. Rev. Lett. **65**, 1713, (1990)

[34] T. A. DeGrand, H. I. Miettinen, Phys. Rev. D **24**, 2419, (1981)

[35] T. A. DeGrand, J. Markkanen, H. I. Miettinen, Phys. Rev. D **32**, 2445, (1985)

[36] Particle Data Group, Phys. Rev. D. **54**, (1996)

[37] W. G. D. Dharmaratna and G. R. Goldstein, Phys, Rev. D, **41**, 1731, (1990)

[38] W. G. D. Dharmaratna and G. R. Goldstein, Phys, Rev. D, **53**, 1073, (1996)

[39] B. Andersson, *et al.*, Phys. Lett. **85B**, 417, (1979)

[40] B. Andersson, *et al.*, Phys. Rep. **97**, 33, (1983)

[41] A. Bravar, PhD Thesis, Univ of Iowa, 1994

[42] J. Engelfried, *et al.*, preprint hep-ex/9811001

[43] Private communication with Scott McKenna and various internal SELEX documents (H-notes)